8-2020

Theoretical and Experimental Investigation of the Impact of Lubricant Oil Additives on the Performance of PD-Based Three-Way Catalysts (TWCs)

Daekun Kim
University of Tennessee, kkun@vols.utk.edu

To the Graduate Council:

I am submitting herewith a dissertation written by Daekun Kim entitled "Theoretical and Experimental Investigation of the Impact of Lubricant Oil Additives on the Performance of PD-Based Three-Way Catalysts (TWCs)." I have examined the final electronic copy of this dissertation for form and content and recommend that it be accepted in partial fulfillment of the requirements for the degree of Doctor of Philosophy, with a major in Mechanical Engineering.

Nguyen Ke, Major Professor

We have read this dissertation and recommend its acceptance:

Seungha Shin, Jay Frankel, Joshua Fu, Todd Toops

Accepted for the Council:

Dixie L. Thompson

Vice Provost and Dean of the Graduate School

(Original signatures are on file with official student records.)

Theoretical and Experimental Investigation of the Impact of Lubricant Oil Additives on the Performance of Pd-Based Three-Way Catalysts (TWCs)

A Dissertation Presented for the

Doctor of Philosophy

Degree

The University of Tennessee, Knoxville

Daekun Kim

August 2020

DEDICATION

I would like to dedicate this work to my family, especially my wife and my parents, and friends who have supported me in achieving my academic goals.

ACKNOWLEDGEMENTS

I would like to thank my advisor, Dr. Ke Nguyen, for providing insight into the research and guidance on this project throughout the duration of this project, without which this project would not have been possible I would also like to express my gratitude to my co-advisor, Dr. Todd J. Toops of the Oak Ridge National Laboratory (ORNL), for sharing his invaluable knowledge in the area of catalysis, and for ensuring that I had access to the facilities for this project at the National Transportation Research Center (NTRC). I would like to thank Dr. Vitaly Prikhodko and the late Dr. C. Stewart Daw of ORNL for providing their MATLAB code for the mathematical modeling of the TWCs. I would like to recognize the invaluable assistance of Dr. D. William Brookshear, not just at the beginning but throughout the duration of the project. I also would like to thank Dr. Jay Frankel, Dr. Seungha Shin, and Dr. Joshua S. Fu for serving on my thesis committee members. In addition, I want to express my appreciation to Dr. Michael J Lance for helping in surface characterization studies and to Dr. Jun Qu for providing background information on ZDDP1, ZDDP2, and IL additives. Lastly, I want to express my appreciation to the United States Department of Energy (DOE) for the financial support of this project.

ABSTRACT

Anti-wear (AW) additives in lubricating oil are being used in engines to improve fuel efficiency and durability. Currently, one of most commonly used anti-wear (AW) additives is zinc dialkyldithiophosphate (ZDDP) due to its high effectiveness in reducing friction in engines. However, the main components of ZDDP, such as zinc, phosphorus, and sulfur, have been shown to form ash during the engine combustion, causing significant deactivation of emissions control catalysts. Consequently, it is imperative to develop new AW additives which are not just more effective in reducing friction than ZDDP, but also ashless, and thus have less impact on emissions control catalysts. Recently, a new-generation of AW additives, the oil-miscible ionic liquids (IL), has been developed. This new phosphorus only-containing AW additive mixed with ZDDP demonstrate less-friction and thus greater fuel economy than ZDDP. However, there is a lack of studies to investigate its impact on emissions control catalysts. Therefore, the present research is aimed at evaluating the poisoning of Pd-based three-way catalysts (TWCs) by ZDDP and IL. A Westerbeke SBCG gasoline generator or Genset is used to perform accelerated poisoning of the TWCs in six different scenarios: neat gasoline (no additives), IL, ZDDP1, ZDDP2, IL+ZDDP1, and IL+ZDDP2. After aging, the performance of all accelerated lubricant additive-aged TWC samples is evaluated and compared to that of NA sample in a bench-flow reactor. The impact of AW additives ZDDP and IL on the performance of the TWCs is investigated by comparing the temperature of 50% conversion (T_{50}) and 90% conversion (T_{90}) for NO, CO, C_3H_6, and C_3H_8, water-gas shift (WGS) reaction, and oxygen storage capacity (OSC)..

The deactivation mechanisms of poisoned TWCs are identified using surface characterization techniques such as Brunauer-Emmett-Teller (BET),

electron probe microanalysis (EPMA), X-ray diffraction (XRD), and inductively coupled plasma (ICP) analysis. In addition, a steady state, one-dimensional continuous-stirred tank reactors (CSTRs) mathematical model of a TWC is being developed, and it considers 14 different global reactions. It is anticipated that the results from the model can be used to identify the most dominant deactivation mechanisms.

TABLE OF CONTENTS

LIST OF TABLES

LIST OF FIGURES

CHAPTER 1
INTRODUCTION AND BACKGROUND

This chapter presents background information on three-way catalysts (TWC) research such as emission regulations, TWCs, and engine lubricant additives. An overview of typical gasoline engines and description of hazardous gas emissions from gasoline engines are given in Section 1.1. Current and future trends in US emission regulations and increasingly stringent requirements are described in Section 1.2. A description of the structure, composition, and performance of a TWC is given in Section 1.3. Finally, a description of the molecular structure, components, and properties of commercially-used engine lubricant additive ZDDP and next-generation engine lubricant additive IL are provided in Sections 1.4.1 and 1.4.2, respectively.

1.1 Gasoline Engines

In the United States, gasoline vehicles that dominate the light-duty vehicle fleet (cars and light trucks) are the largest oil consumption sector. According to the reports published by the U.S. Environmental Protection Agency (EPA) in 2009, passenger cars consume about 40% of US oil consumption and contribute 20% of all U.S. CO_2 emissions from oil consumption [1]. Thus, by implementing fuel-efficient technologies for spark ignition (SI) gasoline vehicles, much effort is underway to reduce US oil consumption, which can significantly reduce greenhouse gas emissions (CO_2). The overwhelming majority of automobiles are powered by port fuel injection (PFI) gasoline engines. In PFI engines, the fuel is sprayed into the intake port of each cylinder and mixes with the incoming air

outside the combustion chamber. The injected liquid fuel is vaporized by absorbing thermal energy from the surface of the intake valve and intake port before it enters the cylinder chamber. The composition of exhaust gases from gasoline engines typically consists of carbon monoxide (CO), nitrogen oxides (NO_x), unburned hydrocarbons (UHC), hydrogen (H_2), water (H_2O), carbon dioxide (CO_2), oxygen (O_2), and nitrogen (N_2). The main regulated pollutants among these species are CO, NO_x, and UHC because of harmful health effects, and specifically NO_x, a major contributor to acid rain.

Hydrocarbon (HC) and carbon monoxide (CO) emissions are products of incomplete combustion. HCs react with nitrogen oxides to form ground-level ozone (O_3), the main component of smog. O_3 irritates eyes, causes shortness of breath, wheezing, fatigue, headaches, and nausea, and aggravated respiratory problems [2]. In addition, some of the hydrocarbons are also toxic. CO is a colorless, odorless, and poisonous gas. High levels of CO can be fatal because it restricts the flow of oxygen to the body's organ [3]. Nitrogen oxides (NO and NO_2 or collectively NO_x) are formed through oxidation of N_2 under high pressure and temperature conditions of combustion inside the engine cylinder. NO_x emissions not only contribute to the formation of ground-level ozone and acid rain, but also cause various health problems [4].

1.2 Emission Regulations

The use of automobiles has been widespread and increased rapidly in recent decades and with it its adverse impact on the environment. Since various environmental pollutants such as NO_x, CO, HCs, and particulate matter (PM) emitted from automobiles also have harmful effects on human's health, the

international community stipulates and continuously implements automobile emissions regulations to protect citizens and improve the environment. In the USA, the Clean Air Act (CAA) was amended in 1970 to regulate concentration levels of HC, CO, and NO_x from vehicle exhausts. Light-duty vehicles (LDV) emissions standards are divided into Tier1, Tier2, and Tier3. The Tier1 emission standards were finalized on June 5, 1991, and phased-in between 1994 and 1997 for all light-duty vehicles (LDVs) such as passenger cars, light-duty trucks, sport utility vehicles (SUVs), minivans, and pick-up trucks [5]. Regulations with Tier2 emission standards were phased-in between 2004 and 2009, and they were more stringent for large vehicles such as medium-duty passenger vehicles (MDPV) [6]. The Tier2 regulations also defined the limits on the amount of sulfur permitted in gasoline and diesel fuels, since sulfur could adversely affect the exhaust treatment systems and consequently interfere with their operation. The recently implemented regulations, Tier3 proposed in March 2013, are more stringent than Tier2 in setting new vehicle emissions standards and the lower amount of sulfur content of gasoline in 2017. The important changes in Tier3 regulations are: 1) NMOG (non-methane organic gases) and NO_x emissions are combined under Tier3 regulation, whereas Tier2 regulated individually. The fleet average NMOG+NO_x limit has been in effect starting from 2017, and this fleet average emission must meet 30 mg/mi by 2025, 2) the durability of after-treatment devices has been increased from 120,000 miles to 150,000 miles, and, finally 3) E10 gasoline, which is contained 10% ethanol, is employed for gasoline vehicle's exhaust and evaporative emissions tests [7]. The certification bin standards of Tier3 is shown in Table 1.1. It is separated into seven different bins and must reach bin 30 by 2025.

Table 1.1 Tier 3 certification emissions standards for light-duty vehicles [7].

Bin	NMOG+NO_X mg/mi	CO g/mi	PM mg/mi	HCHO mg/mi
Bin 160	160	4.2	3	4
Bin 125	125	2.1	3	4
Bin 70	70	1.7	3	4
Bin 50	50	1.7	3	4
Bin 30	30	1.0	3	4
Bin 20	20	1.0	3	4
Bin 0	0	0	0	0

In addition, the national program by the Environmental Protection Agency (EPA) and National Highway Traffic Safety Administration (NHTSA) is developed to reduce greenhouse gas (GHG) emissions and improve the fuel economy of light-duty vehicles. As shown in Figure 1.1, GHG emissions from transportation in 2017 accounted for 29% of total GHG emissions in the United States, and efforts and regulations to reduce the amount of GHGs, particularly CO_2 emitted from transportation. The overall vehicle CO_2 emission targets from 2016 to 2025 are shown in Table 1.2 [8]. As given in Table 1.2, from 2017 to 2021, the annual CO_2 emission reduction target is 3.5% annually for model year (MY) 2017 to 2021 and

5% from 2022 to 2025. On average, as a result, the required CO_2 emissions with the new EPA regulation is 163 g/mile in MY 2025. In addition, the fuel economy required for the corporate average fuel economy (CAFE) standards would be between 48.7 and 49.7 mpg in MY 2025.

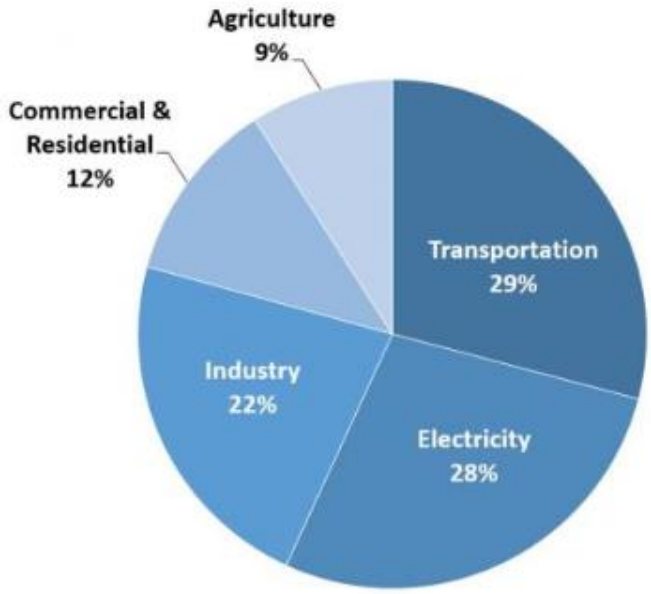

Figure 1.1 Total U.S. greenhouse gas (GHG) emissions by economic sector in 2017 [9].

Table 1.2 Emission compliance footprint-based CO_2 standards (g/mi) and corresponding fuel economy (mpg) and future targets [8].

	2016	2017	2018	2019	2020	2021	2022	2023	2024	2025
Passenger Cars (g/mi)	225	212	202	191	182	172	164	257	150	143
Light Trucks (g/mi)	298	295	285	277	269	249	237	225	214	203
Combined Cars & Trucks (g/mi)	250	243	232	222	213	199	190	180	171	163
Combined Cars & Trucks (mpg)	35.5	36.6	38.3	40.0	41.7	44.7	46.8	49.4	52.0	54.5

1.3 Automotive Catalysts for Gasoline Engines (TWC)

To reduce emissions from the gasoline engines, three-way catalysts (TWCs) have been employed since the 1980's [10]. A TWC is commonly used in engines operating with a stoichiometric air-to-fuel ratio (AFR) of about 14.7:1. The TWC aims to effectively control the emissions of NO_x, CO, and HCs, which are harmful substances contained in the exhaust gases of the gasoline engines, to be released into N_2, CO_2, and H_2O. The three main reactions of TWC (oxidation reactions, NO reductions, and H_2 generation reactions) can be expressed as follows:

1. Oxidation reactions:

1) $C_mH_n + O_2 \rightarrow CO_2\ (CO) + H_2O$

2) $CO + O_2 \rightarrow CO_2$

3) $H_2 + O_2 \rightarrow H_2O$

2. NO Reduction reactions:

1) $C_mH_n + NO \rightarrow N_2 (N_2O, NH_3) + H_2O + CO_2$

2) $CO + NO \rightarrow CO_2 + N_2 (N_2O)$

3) $H_2 + NO \rightarrow N_2 (N_2O, NH_3) + H_2O$

3. Hydrogen production reactions:

1) $CO + H_2O \rightarrow CO_2 + H_2$

2) $C_mH_n + H_2O \rightarrow CO_2 + H_2$

As shown in Figure 1.2, the three-way catalytic conversion efficiencies of NO, CO, and UHCs show the highest performance at air-fuel ratios close to the stoichiometry point (14.7: 1). However, under excessive air supply conditions (fuel-lean condition above A/F is 14.7 or λ is 1), the reaction of the NO reductants with excessive air causes a shortage of the NO reducing agent, which significantly reduces the NO conversion. Therefore, it must work in narrow bands or windows close to the stoichiometric ratio, and an oxygen sensor (or lambda sensor) is installed downstream of the catalytic converter to determine the optimal AFR for the conversion of harmful gases.

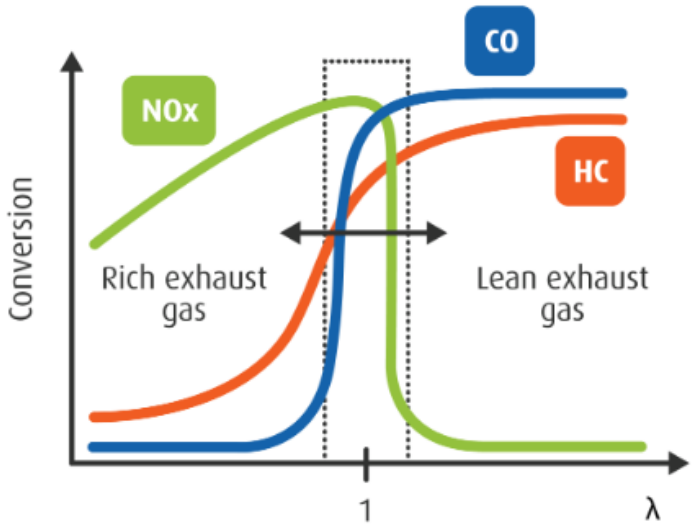

Figure 1.2 Typical performance of three-way catalyst (Pd/Rh) as a function of the lambda [11].

The widely used configuration of the TWC is a monolith or honeycomb structure with a cordierite substrate ($2MgO{\cdot}2Al_2O_3{\cdot}5SiO_2$). The advantages of this type of configuration are high surface-to-volume ratio with low-pressure drop as well as high heat and mass transfer rates. However, because of the low surface area of honeycomb monolith, γ-Al_2O_3 is employed as the support on the monolithic cordierite since it has a high surface area (100-200m^2/g) and good thermal stability at high temperatures [12]. However, at temperatures exceed 1000°C, γ-Al_2O_3 undergoes a phase change to α-Al_2O_3 with a much smaller surface area. Moreover, γ-Al_2O_3 does not have the capacity of storing and releasing oxygen [13]. For that reason, cerium oxide (CeO_2), a well-known

oxygen storage material, is added to the washcoat in order to improve the conversion of CO, HC, and NO_x by storing and releasing oxygen according to Ce^{4+}/Ce^{3+} redox reactions [14]. However, pure CeO_2 generally has poor thermal stability and weak metal-CeO_2 interaction [12,13,15]. Consequently, in order to enhance the thermal stability of $Pd/CeO_2/Al_2O_3$, other oxides such as ZrO_2, SiO_2, BaO, and La_2O_3 have been added to the catalyst in appropriate amounts [16-27]. For example, zirconium oxide (ZrO_2) is mixed with CeO_2 to form $Zr_xCe_{1-x}O_2$ (x = 0.25), and the mixed oxide (Zr-Ce) is used as an oxygen storage compound [28]. In addition, the mixed oxides ($Ce_xZr_{1-x}O_2$) can help to improve noble metal (NM) dispersion as well as to reduce particulate matter (PM) [29]. The noble metals such as platinum (Pt), Palladium (Pd), and Rhodium (Rh) are generally utilized as the active catalyst components. Table 1.3 shows a general function of each precious metal. In the past few decades, Pt/Rh TWCs are used commercially at a weight ratio of 5:1 (Pt: Rh) because of their high level of activity and good resistance to sulfur (S) poisoning. Pd has recently been considered a Pt replacement because it was substantially less expensive. However, as the use of Pd in automotive catalysts has increased recently, the price of Pd has been rising, and it is now much less competitive. According to previous studies [30,31], Pt has higher oxidation activity for C_3H_8 than Pd, while the oxidation of alkanes (CH_4 and C_2H_6) on Pd is higher than Pt. It was also found by Yao et al. [30] that the rate of CH_4 and C_2H_6 oxidation over Pd is much faster than that of C_3H_8 oxidation, but the oxidation of these alkanes over Pt is reversed. Even though Pd-based TWC has limitations due to its sensitivity to phosphorous (P), sulfur (S), and lead (Pb) poisoning from the fuel as well as from the lubricant additives [32,33], it has several advantages compared to Pt-based TWCs such as economic consideration, good light-off performance, particularly for UHCs, and good resistance to thermal sintering [34,35].

Table 1.3 General function of precious metal in TWC.

Precious metal	Functions
Pt	Oxidation of CO, HC, and NO_x [29,36,37].
Pd	Oxidation of CO and HC [36-39].
Rh	Promote NO dissociation (reduction of NOx) and Oxidation of CO [29,40].

1.4 Anti-wear (AW) Additives

Anti-wear (AW) additives in lubricating oil are used by the automotive industry to improve engine efficiency and durability. Currently, the most common AW additive is zinc dialkyldithiophosphate (ZDDP) because of its high effectiveness in wear protection. ZDDP has been employed in most current engine oils as an anti-wear, antioxidant, and corrosion inhibiting lubricant additive for a long time. Recently, a new-generation of AW additives, the oil-miscible phosphorus only-containing ionic liquids (ILs), have been developed. This new AW IL additives, when mixed with ZDDP, has demonstrated in reducing engine friction, and thus greater fuel economy than ZDDP.

1.4.1 Zinc Dialkyldithiophosphate (ZDDP)

ZDDP is produced by reacting an alkyl or aryl alcohol with phosphorous pentasulfide (P_2S_5), and the resultant acid called dialkyldithiophosphate from the

reaction is neutralized with zinc oxide. The structure and typical characteristics of ZDDP are shown in Figure 1.3 and in Table 1.4, respectively. The chemical formulation of ZDDP is generally optimized according to engine types. ZDDP is classified either as primary or secondary, depending on the type of alcohol used in the manufacturing process. In Figure 1.3, R represents an alkyl or aryl group, and these alkyl groups can be primary, secondary, and tertiary alkyl groups [41,42]. Typically, the more reactive secondary alkyl ZDDP is being used for gasoline engines, and primary alkyl ZDDP with high thermal stability is used for diesel engines [43,44].

ZDDP

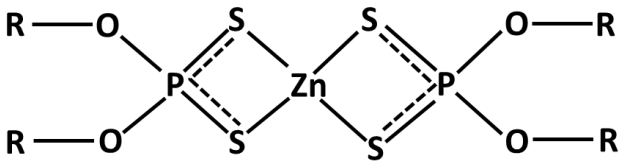

Figure 1.3 Structure of a monomeric zinc dialkyldithiophosphate (ZDDP) [44].

Table 1.4 Typical characteristics of zinc dialkyldithiophosphate (ZDDP) [45].

Additive	Chemistry	Code	Zn (%)	P (%)	S (%)
Zinc Phosphorodithioate	**Secondary, C_6**	**ZDDP-1**	**8.7**	**8.0**	**17.0**
Zinc Phosphorodithioate	**Primary, C_5**	**ZDDP-2**	**10.6**	**9.5**	**20.0**

1.4.2 Ionic Liquids (ILs)

In recent years, significant efforts have been expended in developing new novel lubricant additives that in addition to better performance in reducing friction and wear as well as ashless. Room-temperature ionic liquids (ILs) were originally used as electrolytes in batteries and for metal electrodeposition. These room-temperature ILs were excellent candidates as lubricants or lubricant additives due to its low volatility, non-flammability, and high decomposition temperatures [46-48]. However, the major problem of ILs as neat or base lubricants and additives is its inherent insolubility in common non-polar oil [49-51]. ILs generally composed of quaternary alkylphosphonium cations and various anions are found to be beneficial in reducing friction [52–54]. Figure 1.4 shows typical cations and anions used commonly in ILs. Recently, fully oil-miscible (>50 wt.% solubility in GTL oil) alkylphosphonium-organophosphate ILs have been developed, and these ILs have been found to effectively decrease friction and wear [55-61]. Figure 1.5 shows the structure of ILs, [P8888] [DEHP], and [P66614] [DEHP]

developed with fully oil-miscible alkyl phosphonium-organic phosphate in ILs. One particular IL, [P8888][DEHP] with the typical structure shown at the top of Figure 1.5, when mixed with 0W-16 engine oil has shown to lower friction by 4% to 10% and 82% to 92% lower wear than base oil without additives [62]. Table 1.5 lists the physical properties of [P8888][DEHP] and [P66614][DEHP] additives with different cation structures. Figure 1.6 shows the coefficient of friction and wear compared to different types of engine additives. The mixed additives ([P8888][DEHP] + ZDDP and [P66614][DEHP] + ZDDP) offer the best performance in reducing friction and wear characteristics over either IL or ZDDP additive. Based on Figure 1.6, Qu et al. [63] found that the friction coefficient and the wear volume of the IL+ZDDP additives ([P8888][DEHP] + ZDDP and [P66614][DEHP] + ZDDP) are reduced by 30% and 70%, respectively compared to ZDDP-only additive.

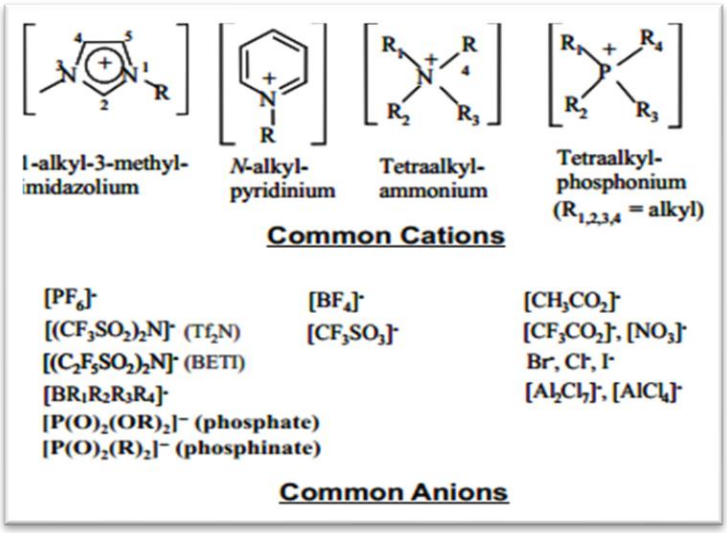

Figure 1.4 Common cations and anions for ionic liquids (ILs) [64].

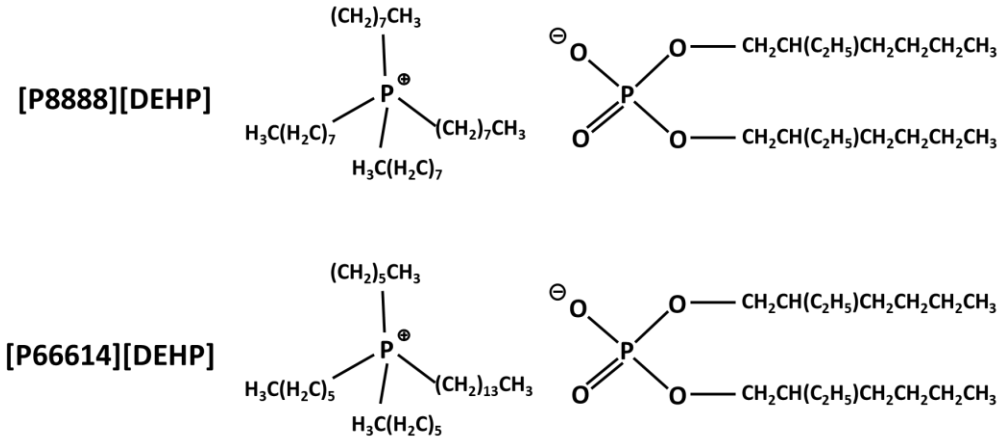

Figure 1.5 Typical structure of [P8888][DEHP] and [P66614][DEHP] [65].

Table 1.5 Molecular weight, oil-solubility, density, and viscosity of selected ILs [62].

Ionic Liquid	Molecular Weight	Density (g/cm^3)	Viscosity of neat IL (cP)			Solubility in GTL oil (wt.%)
			23°C	40°C	100°C	
[P8888][DEHP]	805.26	0.86	>1500	611.8	68.2	>50
[P66614][DEHP]	805.26	0.91	951.0	390.4	45.0	>50

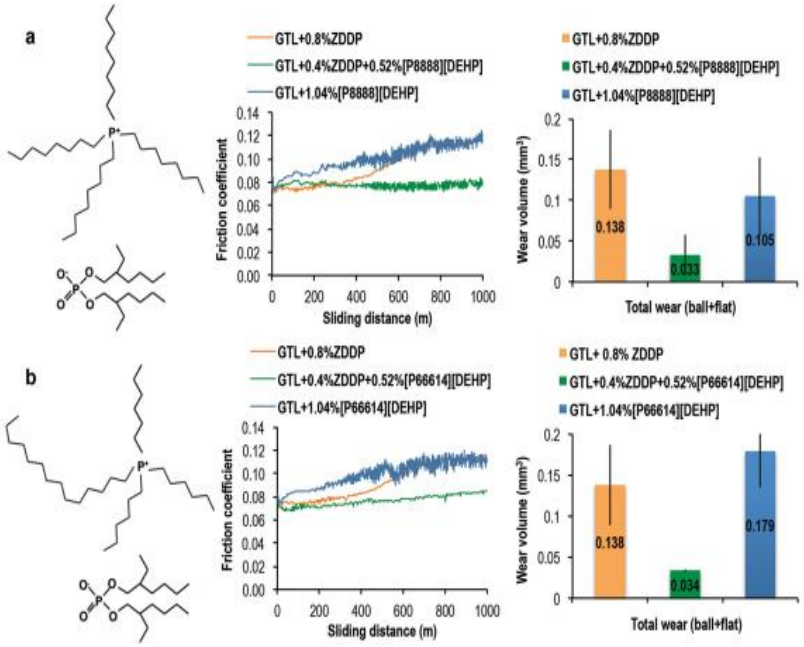

Figure 1.6 Synergistic effects discovered (a) between [P8888][DEHP] and ZDDP and (b) between [P66614][DEHP] and ZDDP [63].

1.5 Scope of Investigation

The purpose of the present study is to investigate the effects of lubricant additives on the performance of Pd-based TWC and the resulting changes in the surface morphology under accelerated engine aging conditions. Specifically, the present study focuses on the poisoning of Pd-based TWC by two different formulations of conventional ZDDP, primary and secondary ZDDP, and a particular fully oil-miscible IL, [P8888][DEHP]. When [P8888][DEHP] is mixed with ZDDP, the mixed additive can reduce the friction coefficient and the wear volume considerably as compared to conventional ZDDP+base oil. However, in order to be the viable candidate as lubricant additives for engine applications, it is important that this mixed IL and ZDDP additive has to be compatible with automotive emissions control. While considerable efforts have been expended in the last twenty years to investigate the impact of ZDDP on the performance of TWCs, not much has been done on the impact of IL on TWCs. To be specific, thus far in the literature, there is only one study that compared the impact of an oil-miscible IL, [P66614][DEHP] and the industry standard ZDDP on the performance of the TWCs, and there is no study involved the mixed IL ([P8888][DEHP]) and ZDDP lubricant additives. This lack of study provides the impetus for the present investigation. It is expected that the results from the present study would provide further insights into the deactivation mechanisms associated with the poisoning of Pd-based TWCs from the mixed IL ([P8888][DEHP]) and ZDDP lubricant additives.

A Westerbeke SBCG single-phase 60 Hz gasoline generator or Genset consisting of a 350 cc water-cooled two-cylinder gasoline engine is used to perform accelerated aging of the TWCs in six different scenarios: neat gasoline

(no additives or NA), gasoline+ZDDP1, gasoline+ZDDP2, gasoline+IL, gasoline+ZDDP1+IL, and gasoline+ZDDP2+IL.

Performance evaluations of the fresh and accelerated engine-aged TWC samples are carried on a bench-flow reactor (BFR) experiments using CLEERS (Crosscut Lean Exhaust Emissions Reduction Simulations) protocol. The thermal aging of the catalyst is investigated by comparing the BFR performance of the NA-aged TWC sample and the fresh TWC sample. In addition, the results of the NA-aged TWC sample are used to examine the effect of lubricant additives on TWC performance as a baseline.

In addition to the BFR performance evaluation, the deactivation mechanisms of the TWC from the thermal aging and lubricant additive poisoning are identified using surface characterization techniques such as N_2 physisorption, electron probe microanalysis (EPMA), X-ray diffraction (XRD), and inductively coupled plasma (ICP) analyses.

A steady-state, one-dimensional continuous-stirred tank reactors (CSTRs) mathematical model is used to predict the performance of a Pd-based TWC sample under the BFR conditions. It is anticipated that the results from the mathematical model in conjunction with those from the BFR and the surface characterization techniques can be used to identify the most dominant deactivation mechanisms.

CHAPTER 2
LITERATURE REVIEW

This chapter provides a review of literature related to the current study on the performance degradation of TWCs. Section 2.1 presents a literature review of the function of the catalyst promoters comprised of mixed oxides containing CeO_2-ZrO_2 for improving and stabilizing the performance of palladium-based three-way catalysts (Pd-based TWCs). Section 2.2 is a literature review of catalyst deactivation, such as sintering and poisoning, as a result of impurities in fuel and engine lubricant additives.

2.1 Promoters for Three-way Catalyst (TWC)

The average exhaust gas temperature at the inlet of the TWC is generally between 300°C and 500°C but can reach up to 1200°C during rapid acceleration and unintended engine misfires. In addition, due to exothermic reactions, such as the oxidation of CO and UHCs on TWC, the temperature of the catalytic converter can reach above 750°C. The components in the catalyst can sinter when exposed to high temperatures continuously, resulting in poor catalytic performance and shortened lifetime. In addition, sulfur (S), phosphorus (P), and zinc (Zn) in the engine lubricant additives and small amounts of S in the gasoline can poison the catalyst components, resulting in a reduction in catalyst performance and shortening the lifetime. Thus, considerable efforts have been attempted to stabilize the catalyst and minimize performance degradation by adding various promoters.

Since the effect of zirconium oxide (ZrO_2) on improving the performance of cerium oxide (CeO_2) in TWCs was not initially well understood, early studies on promoters of Pd/Al_2O_3 TWCs focused on a number of oxides such as La_2O_3 [66-71], VO_x [72-75], Na_2O, and BaO [76-78]. Since 1997, CeO_2 is more commonly used as the oxygen storage for improving the conversion of CO, HC, and NO_x by storing and releasing oxygen according to Ce^{4+}/Ce^{3+} redox reactions. Later on, pure CeO_2 has been replaced by mixed oxides (CeO_2-ZrO_2) by incorporating ZrO_2 into the CeO_2 lattice to improve thermal stability and enhance metal-CeO_2 interaction. Thus, the literature review in this section mainly focused on TWC promoters comprised of mixed oxides containing CeO_2-ZrO_2.

Fernandez-Garcia et al. [79] and Martınez-Arias et al. [80] studied the light-off of CO and NO under stoichiometric $CO+NO+O_2$ gas mixtures for three different TWC formulations: Pd/Al_2O_3, $Pd/(Ce,Zr)O_2$, $Pd/10\%(Ce,Zr)O_2/Al_2O_3$, and $Pd/33\%(Ce,Zr)O_2/Al_2O_3$. As seen in Figure 2.1 and Figure 2.2, the CO oxidation and NO reduction of Ce-Zr mixed oxides Pd-based catalysts are much better than those of Pd-based catalysts without mixed oxides. In addition, the conversion of CO without NO in the simulated gas is 100% in the PdZC catalyst at low temperatures, but oxidation of CO is inhibited when NO is introduced in the simulated gas. They used DRIFTS results to argue that NO inhibited CO oxidation at low temperatures because the passivation of the interface site forms an oxidized state of Pd, which produced lower CO oxidation activity.

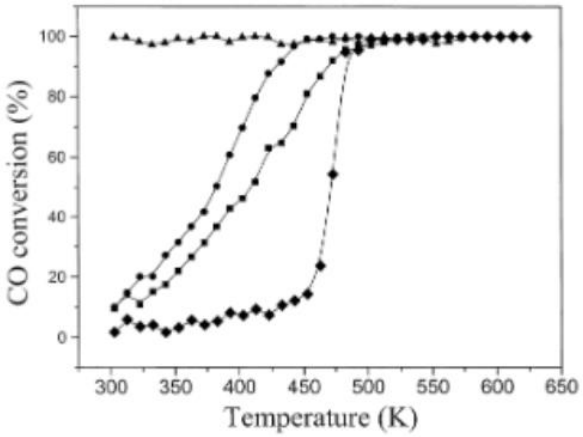

Figure 2.1 CO conversion profiles for the CO+ O_2 reaction over palladium samples: (▲) PdZC; (●) Pd33ZCA; (■) Pd10ZCA; (◆) PdA [79].

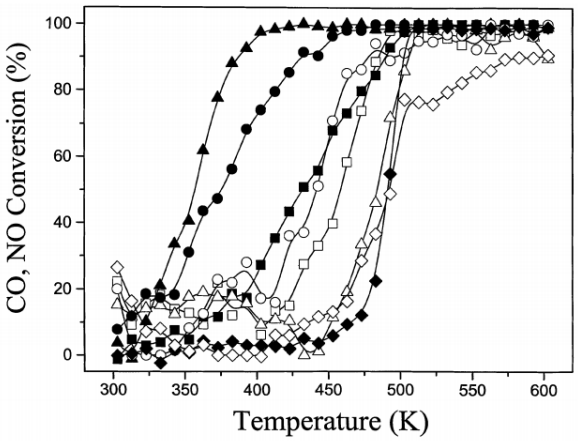

Figure 2.2 Catalyst active for CO (full symbols) and NO (empty symbols) for the CO+NO+O_2 reaction over Pd samples: (▲, △) PdZC; (●, ○) Pd33ZCA; (■, □) Pd10ZCA; (◆, ◇) PdA [80].

Numerous studies have been carried out to investigate the effects of the oxygen storage material (OSC), CeO_2-ZrO_2, on the performance of the Pd-based TWC catalyst. Guo et al. [81] found that high oxygen mobility was observed by adding Pr (praseodymium) and Nd (neodymium) to binary Ce-Zr mixed oxides at low temperatures. Another study by Wu et al. [82] claimed that after the hydrothermal aging at 1050°C, the OSC and DOSC of the Ce-Zr-Pr (CZP) and Ce-Zr-Nd (CZN) samples were much higher than those of the pure Ce-Zr (CZ) sample. Furthermore, the CZP sample showed the best thermal stability among the aged samples, and the results of the BET surface area and XRD analysis confirmed that CZP had little surface area loss and no phase segregation. Additionally, Mikulova et al. [83] investigated the Ce-Zr mixed oxide with Pr ions also found higher oxygen mobility at low temperatures compared to Ce-Nd and Zr-Ce-Nd oxides. According to studies by Wang et al. [84,85], Pd-only TWCs containing Ce-Zr-Pr mixed oxides, improved catalyst performance in both fresh and aged samples, with lower light-off temperatures for the conversion of HC, NO, and CO compared to Pd-only TWCs containing only Ce-Zr mixed oxides, as can be seen in Figure 2.3. They claimed that it is possibly due to the increased OSC and improved reducibility of the Ce-Zr-Pr ternary solid solution. Furthermore, the addition of Nd (5 wt. %) into CZ (Ce-Zr oxides) improved the textural/structural properties of catalysts, enhanced the interaction between the metal and the supports, and increased OSC performance, resulting in improving the TWC activity for aging samples. Wang et al. [86] also investigated TWC samples with rare earth metals such as La, Nd, and Pr doping on $Ce_{0.2}Zr_{0.8}O_2$. They found out that the doping of rare earth metals to $Ce_{0.2}Zr_{0.8}O_2$ mixed oxide would improve the thermal stability, increase BET surface area even after calcination at 1100°C for 4 hours, increased OSC performance, and enhanced the high catalytic activity for the conversion of NO, CO, and HC.

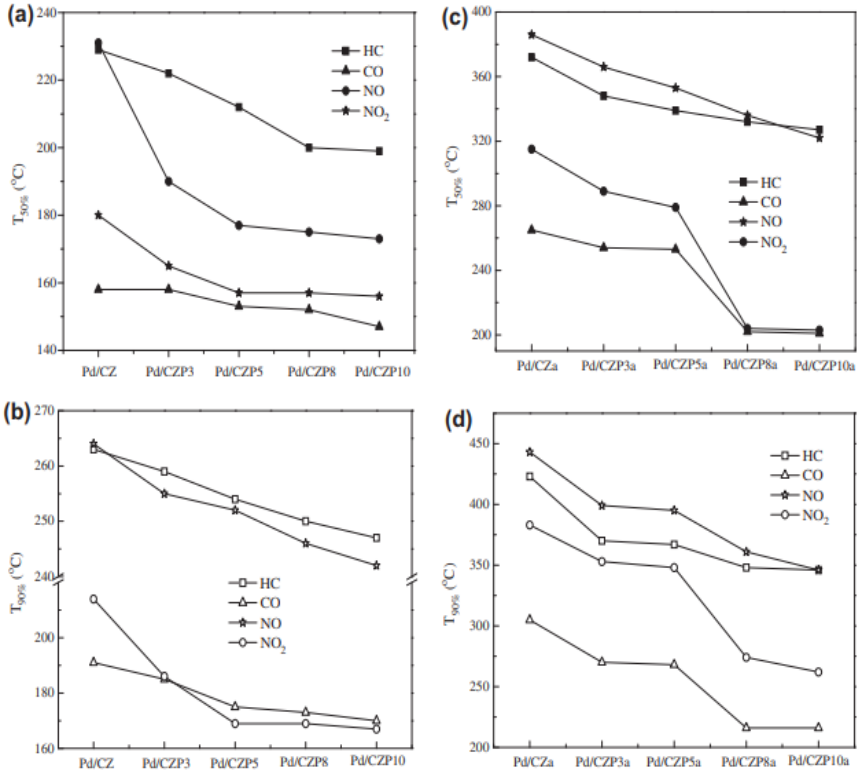

Figure 2.3 Light-off and full-conversion temperature of HC, CO, NO, and NO_2 over all the catalysts (a) light-off temperature over the fresh catalysts, (b) full-conversion temperature over the fresh catalysts, (c) light-off temperature over the aged catalysts, and (d) full-conversion temperature over the aged catalysts [84].

Yttrium (Y) has been studied as a promoter of Ce-Zr mixed oxides. Yamamoto and Tanaka [87] compared the performance of Pd-only catalysts containing Al_2O_3, (Ce-Zr) O_x/Al_2O_3, and (Ce-Zr-Y) O_x/Al_2O_3 as a supporter. They confirmed that Pd-only TWC samples with support containing Y_2O_3 had the best

performance for a 50% conversion window under air/fuel fluctuation conditions, possibly due to improving OSC and stability. Vidmar et al. [88] and Markaryan et al. [89] found that the small amount of Y_2O_3 addition to $Ce_{0.6}Zr_{0.4}O_2$ improved OSC and stability. In a similar study, Yucai et al. [90] observed that the adding of the proper amount Y to mixed oxides ($Ce_{0.6}Zr_{0.3}Y_{0.1}O_2$) had a positive effect on the light-off temperatures for HC, CO, and NO conversion of Pd-only TWC possibly due to the excellent redox properties of Y_2O_3-modified Ce-Zr mixed oxides. Wang et al. [91] studied the effect of Y, Ca, and Ba on the Pd-only TWC with Ce-Zr mixed oxides calcinated at 1100°C in the air for 2 hours. They found that Pd-only TWC with supported Y, Pd/(Ce-Zr-Y) O_x/Al_2O_3, was the best performance for the oxidation of propane as well as for the resistance toward S poisoning. Wang et al. [92] used XPS results to confirm that an appropriate amount of Y_2O_3 might help the stronger interaction between Pd and Zr species to increase Pd dispersion. A number of studies [93-95] investigated the positive effects of oxygen mobility and OSC improvement by incorporating Fe and Ni oxides in Ce-Zr mixed oxides. They found the addition of Fe and Ni helped to improve the performance of Pd-only TWC by the formation of Ce-Zr-M-O (M = Fe and Ni) tertiary solid solution, which facilitated the reduction of Ce^{4+} to Ce^{3+} or the formation of oxygen vacancy.

A few studies on Pd-based TWC performance have been investigated by adding La_2O_3 to Pd/CeO_2-ZrO_2 catalysts. Guo et al. [96] confirmed that the light-off temperature for 50% conversion of the TWC added with La_2O_3 was enhanced after aging for 4 hours at 900°C. Also, improvement of propane (C_3H_8) conversion and thermal stability of TWC by the addition of 10% La_2O_3 was observed by Yao et al. [97] after aging at 1000°C for 5 hours. They confirmed that by adding La_2O_3 to TWCs, high Pd dispersion and reducibility were obtained compared to the TWCs without adding La_2O_3.

Several studies have been conducted to investigate the effects of the formation of Pd-M (M=NiO and Cu) alloy on CO oxidation and NO reduction activity. Hungría et al. reported the performance of Pd-NiO/CeO_2-ZrO_2/Al_2O_3 [98,99] and Pd-Cu/CeO_2-ZrO_2/Al_2O_3 [100] for the CO+NO+O_2 reaction under stoichiometric condition. These studies were found that NiO and Cu enhanced the activity of CO oxidation and NO reduction. They believed that the introduction of NiO led to a preferential interaction between Pd and (Ce-Zr)O_x, which created a more active Pd-(Ce-Zr)O_x interface, improving CO oxidation and NO reduction activity. Also, by the formation of Pd-Cu alloy, N-O bonds could be easily dissociated, which enhanced CO oxidation and NO reduction. However, it has been found that the destruction of the Pd-Cu alloy occurs at high temperatures (above 227°C), resulting in the loss of the positive effect of Cu on the reduction of NO.

Iglesias-Juez et al. [101] compared the activities of CO and NO removal of Pd/CeO_2-ZrO_2 catalysts incorporated with Cr and Cu under stoichiometric conditions of CO+NO+O_2. They reported that the effect of the additive on the CO removal activity was slightly enhanced in the case of the Pd-Cu/CeO_2-ZrO_2 catalyst, mainly due to the presence of the active species Cu(I) as shown in Figure 2.4. Also, adding Cu and Cr for NO removal improved performance between 100°C and 200°C, but it was observed the significantly decreased activity Pd-Cu/CeO_2-ZrO_2 above 180°C. Therefore, the application of Pd-M alloys to TWC operating at high-temperature range requires more effort for thermal stability.

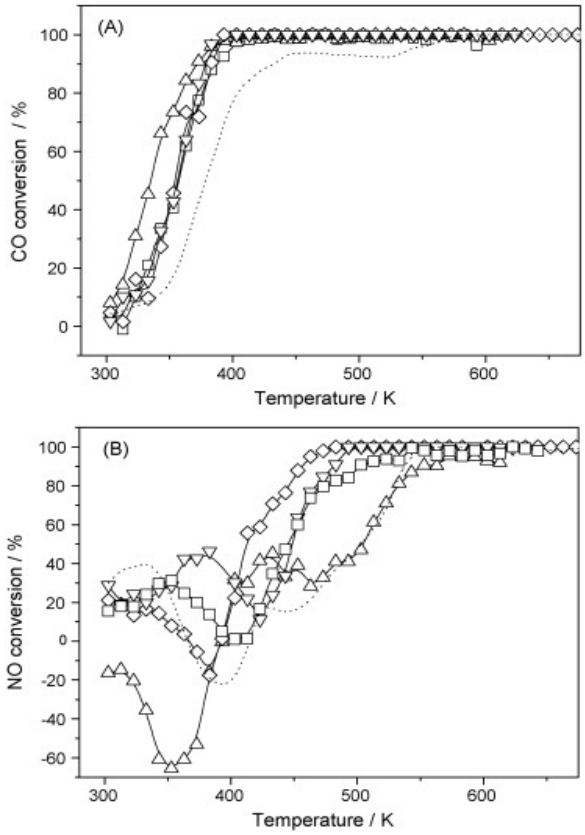

Figure 2.4 CO (A) and NO (B) conversion profiles for the $CO+NO+O_2$ reaction over bimetallic Pd–M samples and monometallic references: (□) PdCZ; (▽) PdNiCZ; (◇) PdCrCZ; (△) PdCuCZ; (dashed line) CuCZ [101].

2.2 Catalyst Deactivations

According to the most recent EPA standard, Tier 3 regulations, the durability requirements for after-treatment have increased from 120,000 miles to 150,000 miles, and research is being conducted to increase catalyst life. Figure 2.5 shows a schematic of the deactivation phenomenon. The main causes of shortening of catalyst durability can be classified into three different categories:

- Poisoning due to strong adsorption of impurities and fouling due to deposit of impurities.
- Sintering and evaporation of precious metals due to high temperature.
- Corrosion/leakage by reaction mixture and mechanical damage.

The deactivation process is a complex phenomenon, and catalyst deactivation occurs at the same time due to various causes during the use of the catalyst.

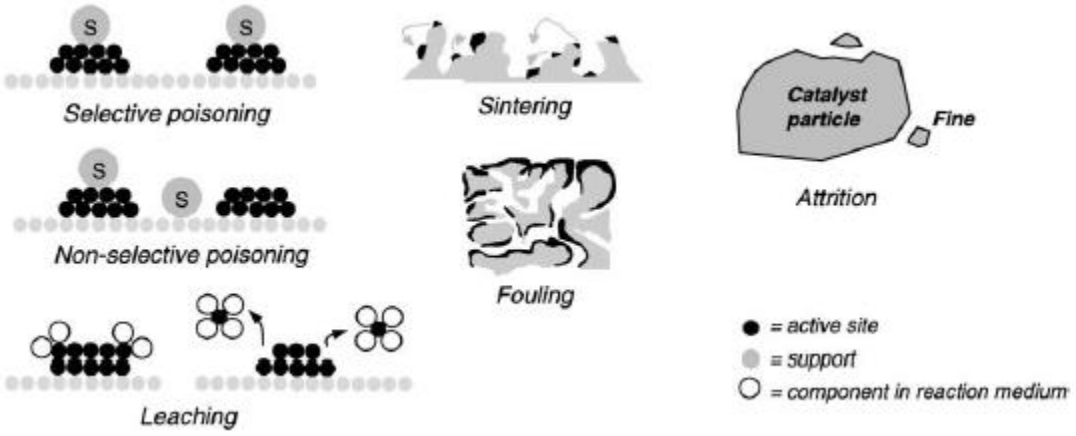

Figure 2.5 Major types of deactivation in heterogeneous catalysis [102].

2.2.1 Sintering

Sintering is a deactivation process due to the agglomeration of catalyst particles by high-temperature exposure, resulting in the loss of the catalytically active surface due to crystal growth of either support or active phase. The loss of support area and catalyst surface area are due to support collapse and pore collapse in the crystal phase of the active phase, respectively [102]. There are several studies to investigate the sintering mechanism of Pd-based TWC and the degradation of the catalyst performance [103-107].

Chen et al. [103] carried out thermal aging in a hydrogen atmosphere for various temperatures and time intervals to determine the sintering behavior of Pd crystallites supported on γ-Al_2O_3. They argued that the sintering of Pd in Al_2O_3 might cause by three different mechanisms: (1) crystallite migration and coalescence, (2) direct ripening, and (3) Ostwald ripening. Xu et al. [104] investigated the contribution of metal particle sintering in Pd/Al_2O_3 under accelerated aging of automotive exhaust catalysts at high temperatures (10 mol% H_2O at 900°C). They argued using chemisorption and TEM results that the loss of catalytically active surface area was due to the growth of particles on the surface of the support rather than encapsulating metal particles inside the support. In addition, they claimed that Ostwald ripening under vapor phase transport was the main reason for the sintering of the Pd/Al_2O_3 catalyst, and Pd particle size was gradually grown by increasing the sintering time as $(time)^{0.5}$. Chen et al. [105] also investigated the effects of temperature on the Pd/Al_2O_3 automotive catalyst. They found that little degradation of Al_2O_3 was observed at high temperatures (~1000°C), and there was no evidence that Pd had undergone significant encapsulation by support. However, Pd particle growth determined by H_2 chemisorption was the main reason for catalyst deactivation in reducing conversion of CO and C_3H_6 by oxidation. Also, according to some studies

[106,107], as more Pd is loaded into the catalyst, the Pd particles sintered more severely due to the higher temperature and higher mileage usage.

Some studies have shown that at high temperatures, noble metals not only increase the particle size but also are encapsulated by the support material of the catalyst (usually CeO_2-ZrO_2), which leads to a decrease in catalyst performance [108-111]. An investigation by Graham et al. [109] claimed that observation of strained PdO associated with catalytic deactivation by noble metal encapsulation indicated that the loss of Pd through encapsulation was greater than the loss of Pd previously realized, and encapsulation was generally through the process of shrinking pores in CeO_2-ZrO_2 supporting materials. A schematic of the various encapsulation steps of aging for Pd particles is shown in Figure 2.6.

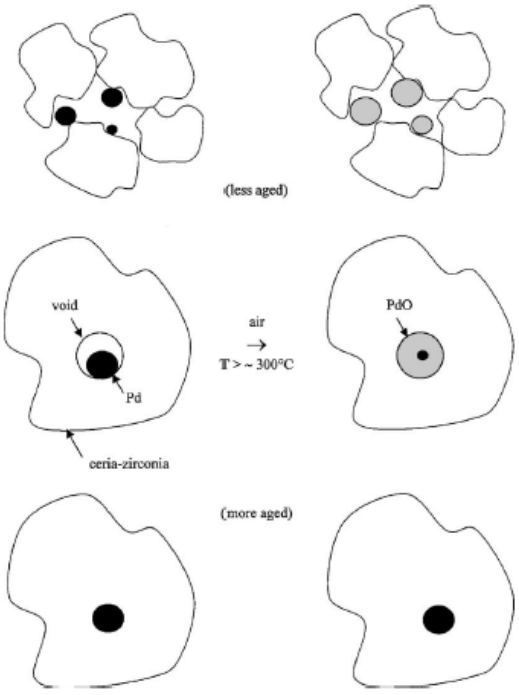

Figure 2.6 Schematic diagram of the various aging stages (early (top), middle (middle), and late (bottom)), in which Pd particles are encapsulated by ceria-zirconia (CeO_2-ZrO_2) [109].

In addition, Graham et al. [110] carried out the accelerated aging with 10 minutes intervals of reducing or oxidizing gas (1% CO/H_2 or 0.5% O_2, respectively, in N_2) at either 1050°C or 1150°C for a total of 12 h. They claimed that the ability to accurately measure the degree of Pd encapsulation was influenced by several factors, but the use of Raman spectroscopy suggested that the presence of modified PdO in the accelerated aging sample provided evidence of Pd encapsulation by CeO_2-ZrO_2. Moreover, the presence of PdO in the XRD pattern was observed as well. In addition, Heo et al. [111] and by Lassi

et al. [112] showed that as the aging temperature and catalyst mileage increased, precious metal particles were sintered as well as encapsulated in the sintered catalyst layer (washcoat), resulting in the CO conversion and OSC gradually decreased due to surface area collapse.

2.2.2 Poisoning

The definition of poisoning is the process of deactivation by strong adsorption of impurities at the catalyst active site. In the case of TWCs, it is well known that poisoning is carried out not only by sulfur (S) in fuel but also by zinc (Zn), sulfur (S), and phosphorus (P) contained in the engine lubricant additives. In the past, because of the use of lead (Pb)-containing gasoline, the impact of Pb in the fuel on the TWC was investigated, but recently, with the use of unleaded gasoline, Pb is no longer considered as a catalyst poisoning impurity. The main components of ZDDP, such as Zn, P, and S, have been shown to form ash during the engine combustion and form compounds on the TWC surface, causing significant deactivation of the TWCs.

2.2.2.1 Poisoning by Sulfur Compounds

Many studies have been conducted on the effect of S poisoning on TWC performance, such as loss of light-off and warm-up activity [32,113-118]. Beck and Sommer [117,119] found that the presence of S had a negative effect of light-off and warm-up performance on both Pd and Pt-Rh catalysts. By using C_3H_6 as a hydrocarbon in the exhaust, they found that S poisoning was

completely reversible for Pt-Rh catalyst, whereas the Pd catalyst was partially irreversible. In addition, Beck et al. [114] investigated the effect of SO_2 on the Pd catalysts supported on Al_2O_3, 5% CeO_2/Al_2O_3, and 8.6% La_2O_3/Al_2O_3. They observed that the impact of S poisoning on the $Pd/Ce/Al_2O_3$ catalyst was partially irreversible at temperatures under 550°C, but it could be reversible when the recover cycle at both rich and stoichiometric feed stream was performed above 700°C as shown in Figure 2.7.

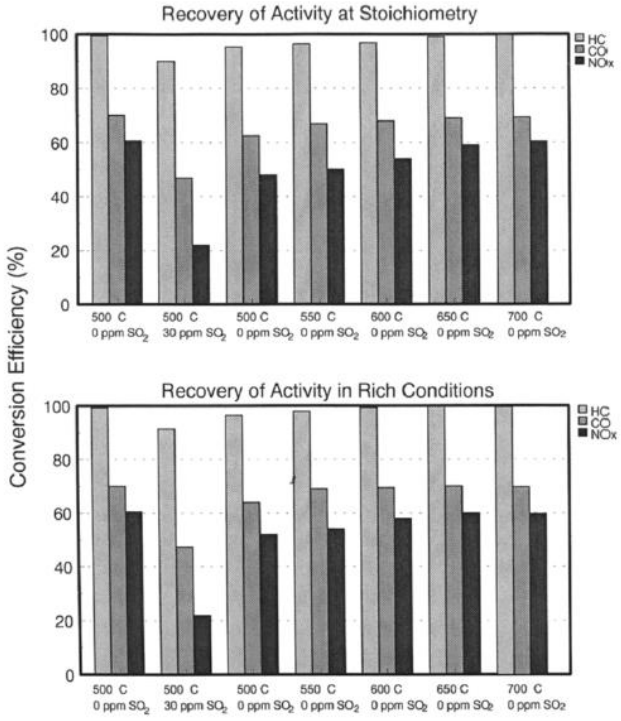

Figure 2.7 Reversibility of performance in Pd catalysts as a function of operating temperature and stoichiometry [114].

Koehl et al. [113] studied the effects of five S levels of 50, 150, 250, 350, and 450 ppm in gasoline on commercial vehicle emissions. They found that the average tailpipe emissions of HC, NMHC, and CO decreased by about 18% each as the S content of gasoline decreased from 450ppm to 50ppm, while the tailpipe emissions of NO_x decreased 8% respectively. However, the use of gasoline containing normal S levels below 50 ppm affected the emissions of HC, NMHC, and CO, but NO_x was not affected. These effects of S on catalyst performance were observed by another Koehl's paper [120].

Yu [116] claimed that the formation of surface sulfite and sulfate groups by Al_2O_3 occurred at temperatures above 200°C from SO_2 and SO_3 caused by PdS oxidation formed by H_2S poisoning of PdO up to 200°C. In addition, according to the H_2 TPR results, most surface sulfite and sulfate groups were removed from the catalyst surface at between 400°C and 600°C and partially restored the catalytic activity.

Recent studies have been addressed the sulfation of ceria [121-124]. Also, Rodriguez et al. [125] claimed with results of X-ray absorption near-edge spectroscopy (XANES) and X-ray photoelectron spectroscopy (XPS) that if SO_2 was adsorbed on pure CeO_2, SO_4 could be formed by the following reaction:

$$CeO_2(solid) + 4SO_2(gas) \rightarrow 2SO(gas) + Ce(SO_4)_2(solid)$$

The effect of the presence of SO_2 on the oxygen storage capacity (OSC) in the exhaust gas was studied by Boaro et al. [126]. The study investigated OSC in CeO_2 and CeO_2-ZrO_2 mixed oxides and observed that both oxides quickly deactivated OSC performance at temperatures below 973K when the feed was SO_2 present.

2.2.2.2 Poisoning by Phosphorus Compounds

At low exhaust temperatures, $Zn_2P_2O_7$ was formed directly on the washcoat surface from the lubricant loss in the exhaust gases, causing site deactivation of the TWCs [127,128]. Also, the formation of cerium orthophosphate, $CePO_4$, has been identified within catalyst washcoat [129-134]. Figure 2.8 schematically shows the deactivation processes of Pd-based TWCs by sintering and poisoning.

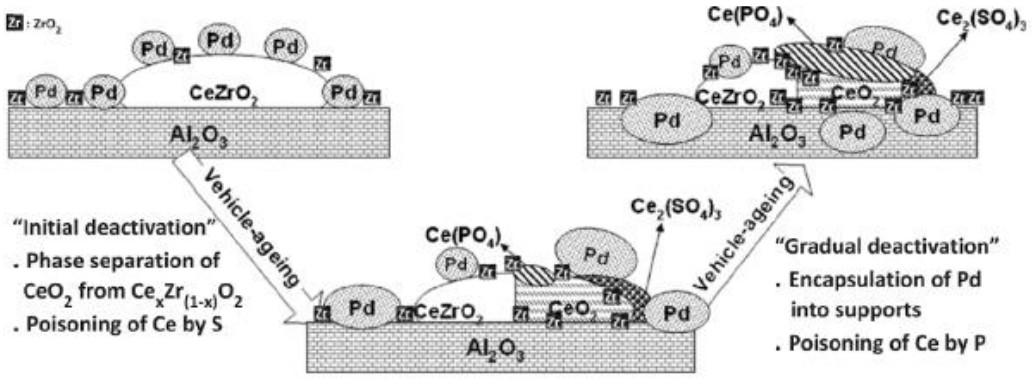

Figure 2.8 Deactivation process of Pd-based TWCs containing $Ce_xZr_{1-x}O_2$ [111].

In a 100,000-mile vehicle test on nine gasoline passenger cars, the effects of different amounts of phosphorus (P) lubricating oil (0.11, 0.08, and 0.06% by weight) on TWC (Pt/Rh dual bed catalytic converter) were investigated by Culley et al. [135]. The Federal test procedure (FTP) results showed that the P of the

lubricating oil had a significantly negative effect on HC and CO emissions. Light-off test results also showed that more P in the lubricant oil negatively affected the conversion of NO, CO, and HC in the field trial TWC catalysts.

The zinc pyrophosphate compound, $Zn_2P_2O_7$, forms an amorphous glaze that acts as a diffusion barrier for the active sites of catalyst and micropores, resulting in a degradation of light-off performance [128,136]. The formation of cerium orthophosphate, $CePO_4$, within the catalyst washcoat is observed as other investigations of TWC poisoning resulting from high-mileage field-service with ZDDP [129-134]. The formation of $CePO_4$ is associated with the high-temperature decomposition of $AlPO_4$, a poisoning precursor due to the adsorption of phosphoric acid in the feed stream exhaust gases [130-132]. Scanning electron microscopy (SEM) and electron probe microanalysis (EPMA) studies of deactivated field-service catalysts have shown preferential adsorption of P at the inlet portion of catalysts within a few inches, and the P concentration profile decreased with increasing distance from the catalyst inlet [129,133]. In addition, it has been shown that P diffuses into the upper layer of the washcoat (usually limited to a depth of 40 μm), and P has a high affinity for washcoat materials and becomes chemically strongly absorbed.

The presence of P in high-mileage TWCs was confirmed by Granados et al. [137]. They analyzed the P, Zn, and Pb content using X-ray Fluorescence Spectroscopy (XFS) for a fresh TWC and two field-deactivated TWCs with 44,000 km and 66,000 km, referred by Granados et al. as u-44 and u-66, respectively. As expected, their results showed that P accumulation in TWCs was higher in high mileage field-deactivated TWC. XRD patterns showed that $Zn_2P_2O_7$ and weak reflections from $CePO_4$ were identified for two field-deactivated TWCs (u-44 and u-66). Moreover, from the light-off curves for NO

reduction and CO and C_3H_6 oxidation, the strongest deactivation occurred in NO reduction and C_3H_6 oxidation, but not in the CO oxidation reaction.

Other studies attributed the degradation of TWCs from P to the formation of $CePO_4$, and possibly $Zn_2P_2O_7$. The formation of $CePO_4$ interferes with the $Ce^{+4} \leftrightarrow Ce^{+3}$ redox behavior resulting in oxygen storage inhibition of the TWCs. Consequently, the presence of these compounds is the main reason for the increase in THC and CO light-off temperatures [128-130].

P is absorbed in the catalyst inlet portion of the first few centimeters and deposited on top of the washcoat layer [132,135,136,138]. Also, depending on the average temperature of the exhaust gas, the operating time, and the concentration of P on the washcoat, the depth of migration into the washcoat was observed differently. Rokosz et al. [129] analyzed P chemistry and P distribution from inlet, middle, and outlet regions of the bricks with two catalysts labeled T1 (120,000 miles) and T2 (102,000 miles). The T1 and T2 were obtained from the field, and the XRD pattern indicated that T1 and T2 had a relatively higher concentration of $MgZn_2(PO_4)_2$ and $CaZn_2(PO_4)_2$, respectively. XRF and BET surface area results clearly demonstrated that P, Zn, and Ca (calcium) are all preferentially absorbed at the inlet of catalysts, reducing the available surface area. The XRF results obtained at the inlet, middle, and rear positions and BET surface area results of the T1 and T2 catalysts are shown in Table 2.1. And, Figure 2.9 shows the conversion of propylene (C_3H_6) by comparing a fresh sample with an aged catalyst (T1) core cored at different locations. They found that the light-off temperature for propylene dramatically decreased from the inlet to the middle and the outlet sections, which was related to the degree of P contamination. More P deposition in the first 1 inch of the catalyst was observed by Culley's study [135]. Figure 2.10 shows the amount of P deposited within a few inches of catalyst.

Table 2.1 Surface area and P, Zn, and Ca concentrations for two field-deactivated catalysts at the inlet, middle, and rear locations [137].

Catalyst	Location	Contaminant Levels (wt. %)			BET SA ($m^2/g_{cat.}$)
		P	Zn	Ca	
T1	Inlet	5.3	3.1	0.5	2.9
	Middle	2.5	0.5	0.0	7.6
	Outlet	1.2	0.3	0.0	7.7
T2	Inlet	3.3	1.6	0.4	5.0
	Middle	1.4	0.3	0.0	10.7
	Outlet	0.5	0.1	0.0	8.7

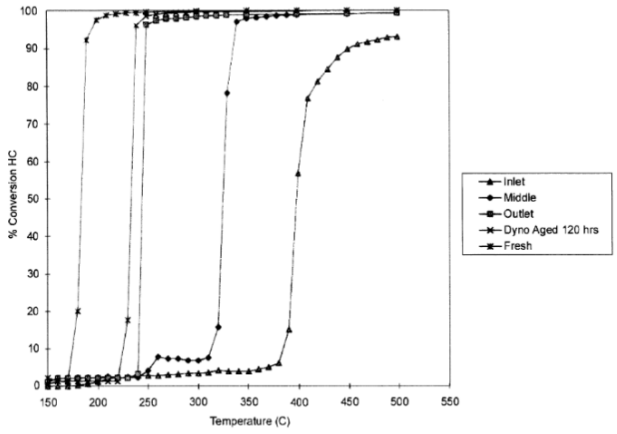

Figure 2.9 Conversion of propylene as a function of temperature over various core samples of taxi-type catalyst. From left to right: fresh catalyst; dynamometer-aged catalyst; outlet, middle, and inlet samples of T1 [129].

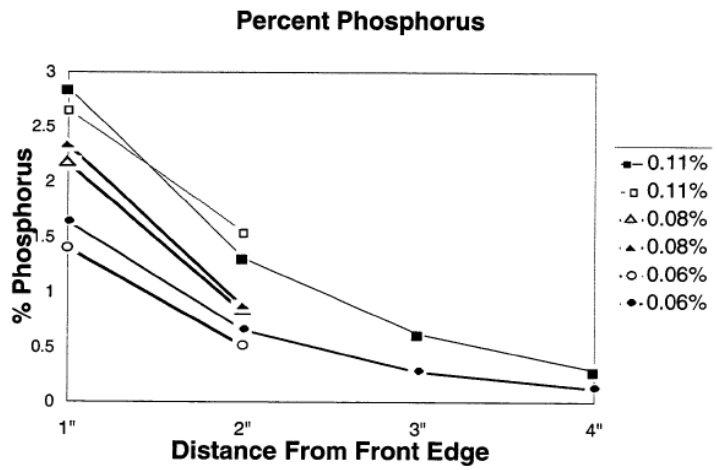

Figure 2.10 The amount of P deposited on the catalyst within a few inches, depending on the amount of P contained in the lubricant [135].

While considerable efforts have been expended in investigating the impact of ZDDP on the performance of TWCs, not much has been done on the impact of IL on TWCs. In a recent study, Xie et al. [134] investigated the impact of a particular IL, [P66614][DEHP] on the TWCs against the industry standard ZDDP. It is worth to mention here that the IL employed by Xie et al., [P66614][DEHP], had a different formulation and components than [P8888][DEHP] used in the present investigation. They performed aging of the TWC samples on a 3500W single-phase Briggs and Stratton gasoline Genset in three different scenarios: neat gasoline (no-additive, or NA), gasoline+ZDDP, and gasoline+IL. After aging the performance of the engine-aged TWC samples as well as the fresh sample was evaluated on a bench-flow reactor (BFR) and characterized using a variety of characterization techniques such as powder X-ray diffraction (XRD), electron

probe microanalysis (EPMA), electrospray analyses, inductive coupled plasma mass spectroscopy (ICP-MS), and nuclear magnetic resonance (31P NMR). They found severe contamination of P observed in the inlet section compared to the middle and outlet sections by EPMA results, and it is shown in Figure 2.11. Figure 2.12 shows that the inlet section samples T50 for FUL_ZDDP and FUL_IL for NO, CO, and C_3H_6 are significantly higher than the T50 for the middle section samples, which has affected the catalyst performance according to the amount of P contamination as seen in EPMA results. In addition, they found that the impact of IL on the performance of TWCs was less severe than that of ZDDP. The water gas shift reaction (WGS) and the oxygen storage capacity (OSC) of the IL-aged TWC sample were less affected than those of the ZDDP-aged TWC sample. Furthermore, the P in the washcoat of the ZDDP-aged TWC sample was predominantly $CePO_4$, whereas it was $AlPO_4$ in the IL-aged TWC sample.

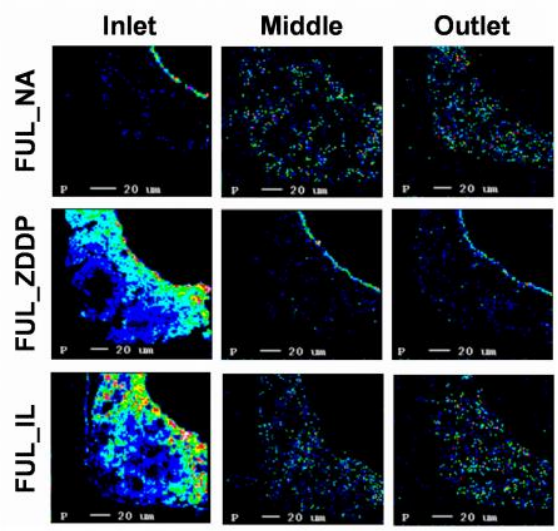

Figure 2.11 EPMA elemental maps of P for the inlet, middle, and outlet sections of FUL_NA, FUL_ZDDP, and FUL_IL [134].

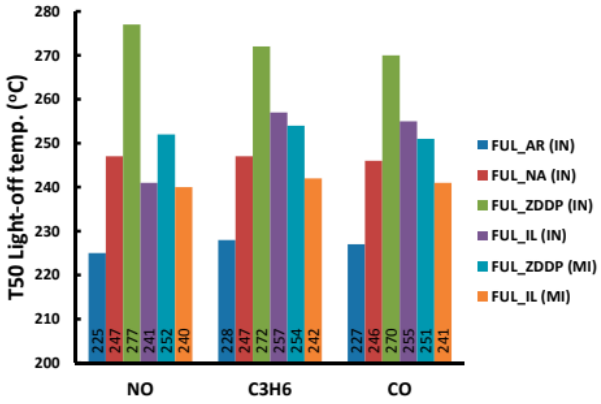

Figure 2.12 T50 light-off temperatures of NO, C_3H_6, and CO for FUL_AR(IN), FUL_NA(IN), FUL_ZDDP(IN), FUL_IL(IN), FUL_ZDDP(MI), and FUL_IL(MI) [134].

CHAPTER 3
EXPERIMENTAL METHODS AND PROCEDURES

This chapter describes the experimental methods and procedures used for the accelerated engine aging of a three-way catalyst (TWC) using an engine bench, and the evaluation of TWC performance on a bench flow reactor (BFR). Additionally, surface characterization techniques used in the present investigation are provided in detail. Section 3.1 presents an overview of an engine-bench called Genset for performing accelerated aging by exposing lubricant additives to TWC at a target temperature. In addition, this section describes the preparation process of a cored TWC sample obtained from a full-size TWC for mounting in a Genset after-treatment system. Section 3.2 provides a description of the bench-flow reactor (BFR) and its components for evaluating the performance of TWC samples. Section 3.3 presents BFR experimental protocols proposed by Cross-Cut Lean Exhaust Emission Reduction Simulations (CLEERS) to investigate the TWC performance. Finally, the principles and overviews of the various surface characterization techniques used in the present study are described in Section 3.4.

3.1 Stoichiometric Gasoline Engine Bench for Accelerated Engine-Aging

3.1.1 Stoichiometric Gasoline Engine Bench (Genset)

A Westerbeke 3.5 SBCG single-phase 60Hz marine gasoline generator, called Genset, is used for exposing the three-way catalysts (TWCs) to lubricant additives. The lubricant additives (IL, ZDDP1, ZDDP2, IL+ZDDP1, and IL+ZDDP2) blended into the GTL base oil are dissolved into gasoline in the fuel tank and introduced into the combustion chamber through a fuel injector during engine operation. The exhaust gases containing the lubricant additive are emitted into the atmosphere through the TWC. As the exhaust gases pass through the TWC, the components in the lubricant additives are exposed to the catalyst at high temperatures and have an impact on it. By calculating the consumption of lubricant oil over the catalyst's full-useful-life (~150,000 miles), this method can simulate the accelerated poisoning of the TWC in a short period of time caused by lubricant burning between the piston rings and cylinder liner during engine operation. The specifications of the Genset are shown in Table 3.1. The Genset consists of a water-cooled 350 cc two-cylinder gasoline engine operating at a constant speed of 2200 rpm, an electric generator, and an aftertreatment system consisting of a Pd-based TWC. The engine produces a peak power of 10.5 hp at 3600 rpm and peak torque of 21 ft-lbs at 2200 rpm. A photograph of the Genset and a schematic of an engine bench are shown in Figures 3.1 and 3.2, respectively.

Table 3.1 Specification of GENSET.

Number of cylinders	**2 cylinders**
Type	**4 cycle**
Displacement	**0.35 liter**
Compression ratio	**9.2:1**
Rated RPM	**2200**
Governor	**Electronic**

Figure 3.1 Photograph of stoichiometric engine bench for exposing TWC to lubricant additives.

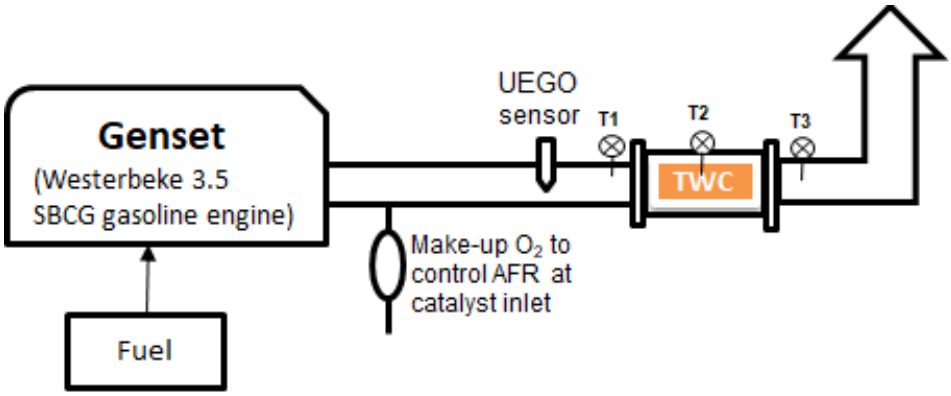

Figure 3.2 Schematic of stoichiometric engine bench for exposing TWC to lubricant additives.

The Genset has an electric fuel injection system controlled by a universal exhaust gas oxygen (UEGO) sensor or lambda sensor. The sensor is installed between the downstream of the engine exhaust manifold and upstream of the TWC to monitor the concentration of oxygen in the exhaust gases. This offers feedback control of the fuel injection to ensure stoichiometric AFR is attained across the TWC. The maximum midbed catalyst temperature during normal operation at an applied load of 1.75 kW and 2200 rpm is approximately 480°C, but this temperature is too low to carry out accelerated aging of the catalyst. Thus, in order to increase the catalyst target temperature, an oxygen injection system is installed upstream of the lambda sensor to introduce additional O_2 in the exhaust manifold. When O_2 is injected into the exhaust gases, the AFR sensor would indicate more fuel (lambda is above 1) would be needed in the combustion chamber even though the engine is operating at stoichiometric condition. This results in a fuel-rich combustion event, and thus excess HCs and

CO would leave the combustion chamber, and after being mixed with the excess O_2 would enter the TWC and create exothermic reactions resulting in higher TWC temperatures. In this manner, the catalyst temperature can be manipulated by adjusting the amount of O_2 injected upstream of the lambda sensor during the accelerated aging of the TWC when exposed to additives.

Three type-K thermocouples labeled as T1 to T3 are used to measure the exhaust gases and the catalyst midbed temperatures. Thermocouples labeled T1 and T3 measure the inlet and outlet exhaust gases temperatures, respectively, whereas thermocouple labeled T2 measures the catalyst midbed temperature. Figure 3.3 shows the temperature change with the amount of injected O_2 into the exhaust gas stream. In this study, the target initial midbed temperature of the TWC is 700°C, and Figure 3.3 indicates that an O_2 flow rate of about 4.5 LPM is required to reach the target midbed catalyst temperature. Gasoline (E10) with a maximum of 30 ppm of sulfur (S) is used to minimize the effect of S poisoning of the TWC. To simulate accelerated exposure of the TWC to lubricant additives, gasoline mixed with appropriate lubricant additive is used to generate exhaust gases containing decomposing products of the lubricant additives to which the TWC is exposed.

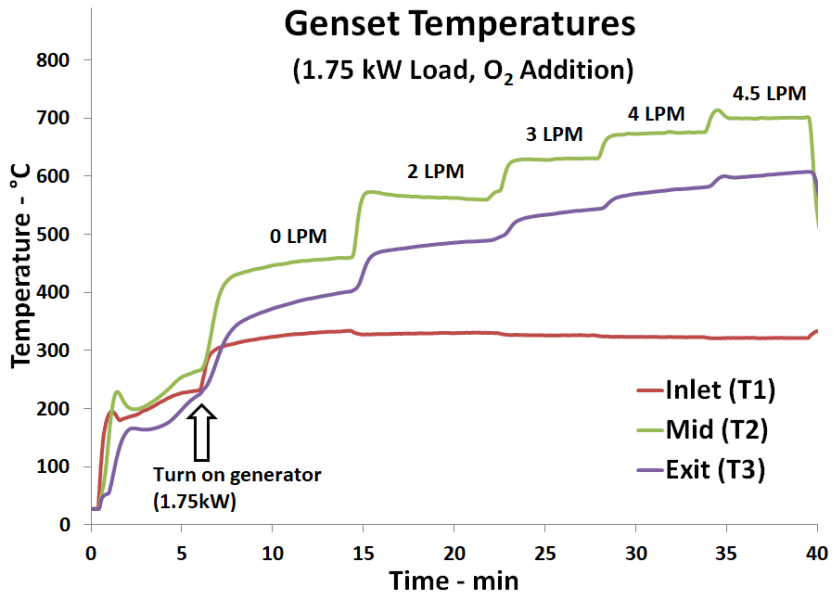

Figure 3.3 Temperature change for gas inlet, TWC midbed, and gas outlet temperature with changing amount of O_2 injection at 1.75 kW.

3.1.2 Pd-based Three-way Catalyst (TWC) and Preparing for Accelerated Aging

The TWCs used for accelerated aging in the present study are obtained from a 2009 MY Jeep Liberty V6 from a local dealership. This Pd-based TWC consists of a γ-Al_2O_3 washcoat (high surface area and relatively good thermal stability) in addition to CeO_2 (oxygen storage material), and promoters such as BaO, ZrO_2, etc. for improving the performance of the catalyst. This commercial monolith Pd-based catalyst consists of a front section and a rear section that

mainly differs from each other in the aspects of cell density and precious group metal (PGM) content. The front section has a high precious metal content (total PGM loading of 0.6% with a ratio of 8:1 of Pd: Rh) and a cell density of 600 cpsi while the rear section has a low precious metal content and a cell density of 400 cpsi. A photograph in Figure 3.4 shows how a cored sample for engine aging is obtained from the full-sized TWCs.

These full-sized TWCs, 105 mm in diameter and 85 mm in length, are cored three pieces with a diameter of 42 mm and a length of 85 mm to expose the catalysts to decomposing products of lubricant additives on the Genset. Each cored catalyst is wrapped in 3M™ Interam™ Mat Mount 1600HT insulation to prevent gas bypass and heat loss between the catalyst and steel can, and it is mounted in a 45 mm diameter and a 180 mm length steel can.

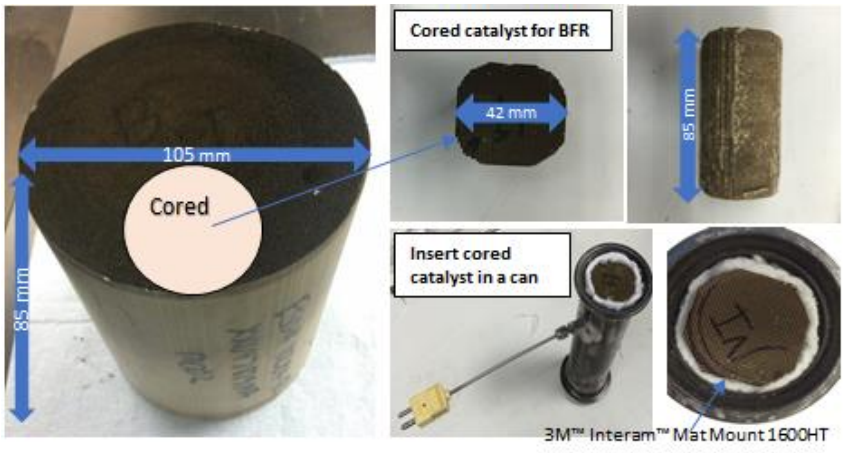

Figure 3.4 Cored sample obtained from full-sized TWC for mounting in the Genset aftertreatment system.

3.1.3 Exposure of Anti-wear Additives

In order to simulate the accelerated exposure of anti-wear additives on the TWC, the amount of oil consumption for the full-useful-life of the TWC of approximately of 150,000 miles is estimated based on a study of West et al. [139] on the oil consumption rate of several vehicles using the standard road cycle (SRC). Based on this research, the consumption rate of lubricant additives is between 15 and 90 kg/km for typical gasoline vehicles. In the present investigation, exposure of the lubricant additives to the TWC is based on the worst-case scenario, assuming that the total amount of additives mixed with fuel has an oil consumption rate of 90 kg/km. Table 3.2 presents the parameters that are needed to estimate the necessary amount of additives for accelerated aging of the samples. The amount of estimated exposure ZDDP2, based on the maximum consumption of lubricant additives of 90 mg/km, is calculated as 32g, assuming 1% additive in the lubricant oil. In order to expose the TWC to the same amount of phosphorous (P) with the ZDDP2 accelerated-aging scenario, different amounts of additives were mixed with the gasoline (E10). For the accelerated-aging scenarios, approximately 45.7g of ZDDP1, 40 g of IL, 20 g of IL plus 22.9 g of ZDDP1 for IL+ZDDP1, and 20 g of IL plus 16 g of ZDDP2 for IL+ZDDP2 are blended with 9.6 gallons of gasoline. The Genset is operated for approximately 24 hours to introduce the required maximum consumption of the AW additives from the fuel tank to the exhaust system directly.

Table 3.2 Key parameters for calculating the amount of additive required for accelerated-aging.

Parameters	
Engine size	2.4 L-eng
Oil consumption rate	145 mg/mile [139]
Normalized oil consumption	60 mg/mile/L-eng
Oil density	0.85 g/ml
Catalyst full-useful-life	150,000 miles
Engine/catalyst ratio	1.5 L-eng/L-cat
Westerbeke 3.5 SBCG catalyst volume	0.228 L-cat
Oil consumption in lifetime	16.4 L-oil/L-cat
Assuming additive concentration in lubricating oil	1.00%

3.2 Bench Flow Reactor System

3.2.1 Bench Flow Reactor (BFR) Overview

The bench flow reactor (BFR) consists of five major components: mass flow controllers (MFCs), a steam generator, a quartz tube reactor enclosed in a temperature programmable furnace, a data acquisition system (DAQ), and a Fourier Transform Infrared (FTIR) spectrometer. A photograph and schematic diagram of BFR is shown in Figures 3.5 and 3.6, respectively. The individual gases of the simulated exhaust gases are introduced into the BFR system using MFCs with a composition similar to that of the exhaust gases from a gasoline engine. The volumetric flow rate of constituent gaseous species of the simulated exhaust gases is determined based on a gas hourly space velocity (GHSV) of 60,000 h^{-1} according to the protocols proposed by cross-cut lean exhaust emission reduction simulations (CLEERS) for gasoline engines. The GHSV is given by Equation 3.1, in which Q_{total} is the total volumetric flow rate of the simulated exhaust gases, and $V_{catalyst}$ is the volume of the catalyst sample in the reactor.

$$\mathrm{GHSV}\ (\mathrm{h}^{-1}) = \frac{\mathrm{Q_{total}}}{\mathrm{V_{catalyst}}} \tag{3.1}$$

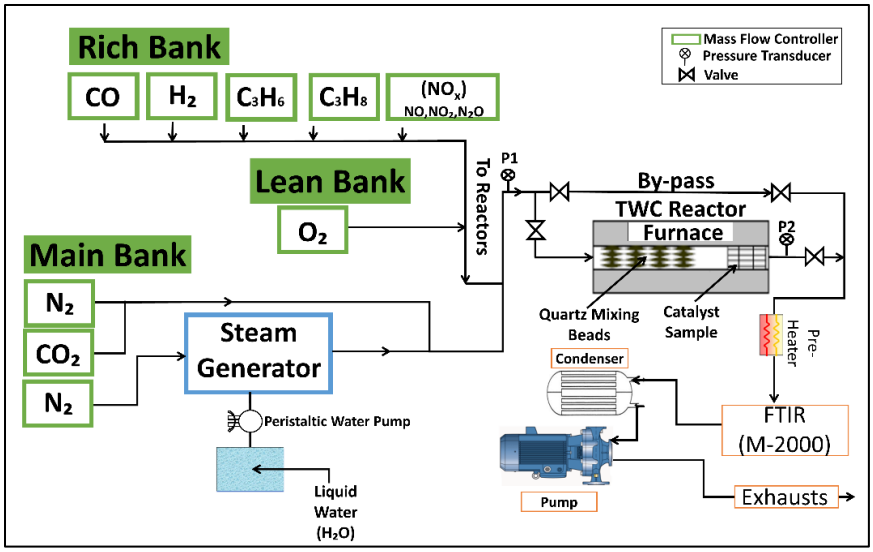

Figure 3.5 Schematic of bench-flow reactor system.

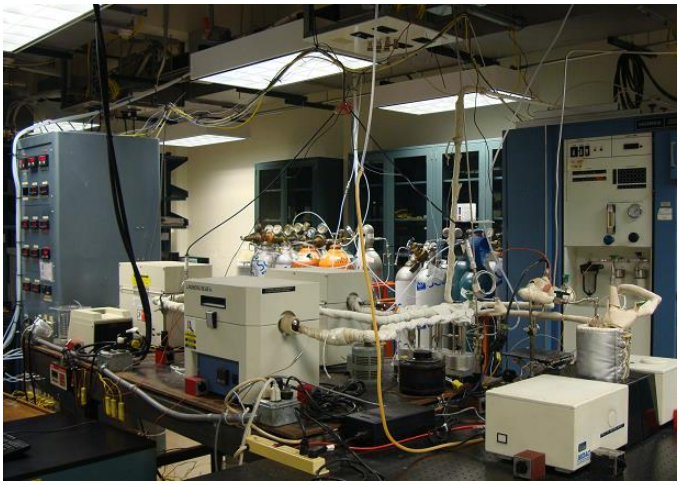

Figure 3.6 Photograph of bench-flow reactor (BFR) system.

Two three-way switching valves are used to alternate the flow between the lean and rich banks. The switching valves are used to perform desulfation for engine-aged TWC samples and to carry out an oxygen storage capacity (OSC) experiment for all TWC samples. Each gas that passes through the MFCs is supplied from the individual gas cylinder.

A peristaltic water pump is used to inject de-ionized water into a steam generator consisting of a quartz tube enclosed in a Lindberg Minimite tubular furnace. N_2 is used as the carrier gas to sweep the steam generated from the evaporation of the de-ionized water due to high temperature. With a furnace temperature of the steam generator of 300°C, an exit steam temperature of 255°C is obtained. To avoid the formation of unwanted ammonium nitrate (NH_4NO_3) and water condensation, all the stainless-steel tubing of the BFR are wrapped with heating tapes and maintained at least at a temperature of 180°C.

The TWC reactor consisting of a quartz tube of 25.0 mm outside diameter and 43.0 cm long is placed inside a Lindberg Minimite tubular furnace to control the inlet temperature of the simulated gas introduced to the catalyst. The upstream section of the quartz tube is filled with quartz beads of 5 mm in diameter to ensure good mixing and uniform heating of the incoming gas. Fresh and engine-aged TWC samples with a diameter of 2.2 cm, a length of 2.54 cm, and a cell density of 600 cpsi wrapped in ULTRA-TEMP^{TM} 390 ceramic tape strands (to prevent gas bypass) are placed in the downstream section of the quartz tube close to the exit of the furnace. A schematic of the TWC reactor and a photograph of the cored TWC sample are shown in Figure 3.7. Three Omega Type-K thermocouples are used to measure the simulated gas and TWC temperatures. Two of the thermocouples positioned on opposite sides of the TWC, at approximately 5 mm from the inlet and outlet, are used to measure the inlet (T1) and exit (T3) gas temperatures. The remaining thermocouple located in

the middle of the catalyst is used to obtain the mid-catalyst wall temperature (T2, midbed).

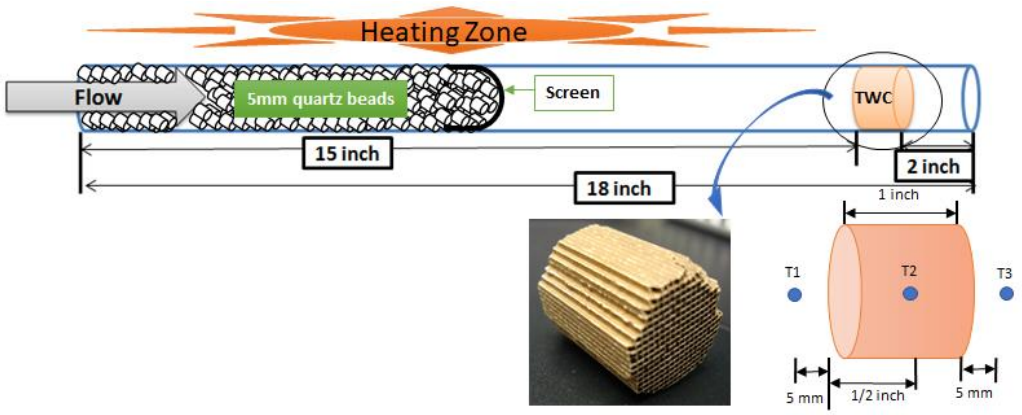

Figure 3.7 Schematic and photograph of the TWC bench-flow reactor (BFR) and three thermocouple locations.

A LabVIEW-based DAQ using a virtual control panel is employed to control the flow rate of the constituent gases and to record temperatures in real-time at a frequency of 1 Hz. The inlet and exit concentrations of NO, CO, C_3H_6, C_3H_8, CO_2, NH_3, and N_2O are measured with a MIDAC-M2000 Fourier transform infrared spectroscopy (FTIR) spectrometer using the software Essential FTIR.

3.2.2 Mass Flow controllers (MFCs)

Mass flow controllers (MFCs) are used to accurately and quickly control the volumetric flow rates of the constituent of the simulated exhaust gases from gas cylinders to the BFR. The volumetric flow rate of each gas component is regulated using the MFC, which is adjustable from 0.1 to 10 LPM. The internal structure of an MFC is shown in Figure 3.8. For accuracy, the MFC used for each gas employs between 60 and 90% of the maximum capacity of the MFC. An MFC consists of an inlet port, an outlet port, a mass flow sensor, CPU, and a proportional control valve. The mass flow sensor inside the MFC has an unheated coil on the upstream and a heated coil in the downstream. When the gas enters the MFC through the inlet port, the introduced gas flows into the capillary of the mass flow sensor and a bypass. Then, the mass flow sensor compares the temperature difference between the upstream and downstream coils from which the mass flow rate is calculated. Under the flow conditions, the heat of the upstream coil is absorbed by the gas molecules and transferred to the downstream coil, resulting in a temperature difference between the two coils. The faster the flow rate, the larger the temperature difference between the coils. The mass flow rate resulting from this temperature difference is converted to an electrical signal by a bridge circuit. The output signals of sensors and input signals controlled by LabVIEW range between 0 to 5V, corresponding to zero flow and its full scale, respectively. The CPU mounted in the MFC compares the voltage of the mass flow sensor with the value of the input signal to proportionally adjust the valve and obtain the required flow rate. All MFCs are calibrated with N_2 gas, and the mass flow rate for the actual flow gas needs to recalculate in terms of N_2 flow rate using a correction factor called the K factor to account for the difference in atomic weight. Gas factors (K factor) and properties used in this study are shown in Table 3.3.

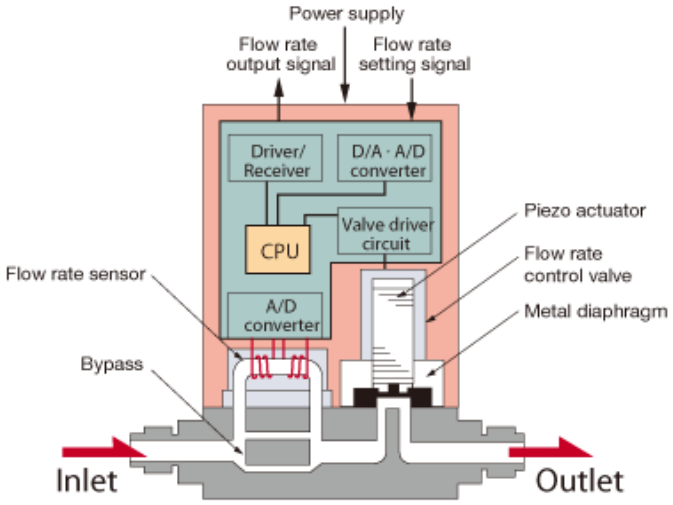

Figure 3.8 Internal structure of a mass flow controller (MFC) [140].

Table 3.3 Actual gas properties and gas factors (K factors).

Actual Gas	*K Factor Relative to N_2*	*C_p [Cal/g]*	*Density [g/l]*
Air	1.0000	.240	1.293
Ammonia, NH_3	.7310	.492	.760
Carbon Dioxide, CO_2	.7382	.2016	1.964
Carbon Monoxide, CO	1.00	.2488	1.250
Hydrogen, H_2	1.0106	3.419	.0899
Nitro Oxide, NO	.990	.2328	1.339
Nitrogen, N_2	1.0000	.2485	1.25
Nitrogen Dioxide, NO_2	.737	.1933	2.052
Nitrous Oxide, N_2O	.7128	.2088	1.964
Oxygen, O_2	.9926	.2193	1.427
Propane, C_3H_8	.35	.399	1.967
Propylene, C_3H_6	.40	.366	1.877

3.2.3 Peristaltic Pump and Steam Generator

The Cole Parmer Masterflex™ model, a peristaltic pump with adjustable flow rates from 0.1 to 580 cc/min, injects de-ionized water using an inner diameter of a 0.8 mm Tygon tube. A photograph of the peristaltic pump is shown in Figure 3.9. The de-ionized water supplied by the peristaltic pump is mixed with the carrier gas N_2, and the two-phase mixture enters a heated stainless-steel tube of 12.7 cm in outer diameter installed inside a Lindberg Minimite furnace. The front portion of the tube is packed with quartz wool, and the rear portion is packed with 3.0 mm quartz beads. The injected de-ionized water is absorbed into the quartz wool and evaporated at a furnace temperature setting of 300°C. The vaporized water is then swept by the carrier gas N_2 over the quartz beads where mixing occurs prior to entering the BFR.

Figure 3.9 Photograph of water pump for injection de-ionized water into steam generator (Cole Parmer Masterflex™).

3.2.4 Fourier Transform Infrared Spectroscopy (FTIR) Spectrometer

A Fourier Transform Infrared Spectroscopy (FTIR) spectrometer is commonly utilized in the analysis of multiple gases' identification and quantity. Since the FTIR analyzer can function even under adverse conditions — such as high temperature and the presence of acid gases like NO_x, SO_x, HCL, etc.—it can be used in automotive emission control research, where multiple gaseous species can be measured simultaneously and in real-time at high temperatures. Every gas molecule has a unique absorption spectrum when it is exposed to infrared (IR) light since all molecular structures have a unique combination of atoms. If the molecule possesses rotation and vibration, the IR spectrum of gas species can be obtained due to a change in the dipole moment. Consequently, monatomic and homonuclear diatomic molecules such as N_2, O_2, H_2, F_2, Cl_2, etc., which have no electronegativity, cannot be measured by the FTIR analyzer because they do not possess the rotational spectrum. Since each gas species has unique absorption spectra called fingerprint at the characteristic wavelengths in the infrared region, FTIR can use a unique spectral fingerprint to identify unknown gaseous compounds compared to a reference. The absorbance can be calculated from transmittance, which is the ratio of the intensity measured with sample gas to the intensity of the background spectrum. Since the absorbance is directly proportional to the gas concentration, the calculated absorbance can be used to quantify the concentration of the sample gas. The units of transmittance and wavenumber are a percentage and reciprocal centimeters (cm^{-1}), respectively.

In this study, a FTIR spectrometer, MIDAC-M2000 with heated gas cell maintained at 195°C, is employed to analyze the gas concentrations through the catalyst with the provided software, Essential FTIR. The FTIR is managed independently of the computer for LabVIEW. The internal structure of a typical

Michelson interferometer and a photograph of FTIR (MIDAC M-series) are shown in Figures 3.10 and 3.11, respectively. The M-series FTIR mainly consists of a fixed mirror, a moving mirror, a beamsplitter, a gas sample cell, a HeNe laser, an infrared (IR) source, and an MCT detector. The M-2000 FTIR spectrometers can be used from 6000 to 400 cm^{-1} spectra range with potassium bromide (KBr) optics due to its suitable transmission (7000 ~ 400 cm^{-1}). A high-resolution sample cell with zinc selenide (ZnSe) windows and multiple path lengths of 3.0-m is employed. The gas sample cell is heated to around 200°C to avoid ammonia nitrate (NH_4NO_3) formation, which can severely corrode the gold-coated mirrors in the sample cell. In the present study, the MIDAC FTIR spectrometer is used to measure the concentration of NO, NO_2, CO, C_3H_6, C_3H_8, CO_2, NH_3, and N_2O.

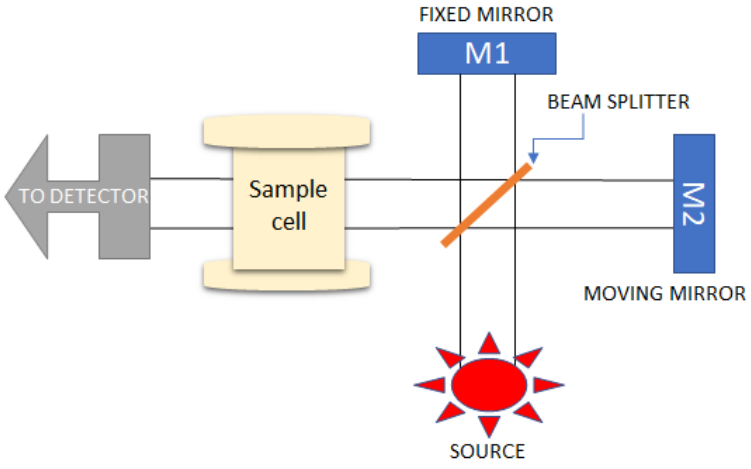

Figure 3.10 Internal structure of IR energy and the mirrors (A typical Michelson interferometer).

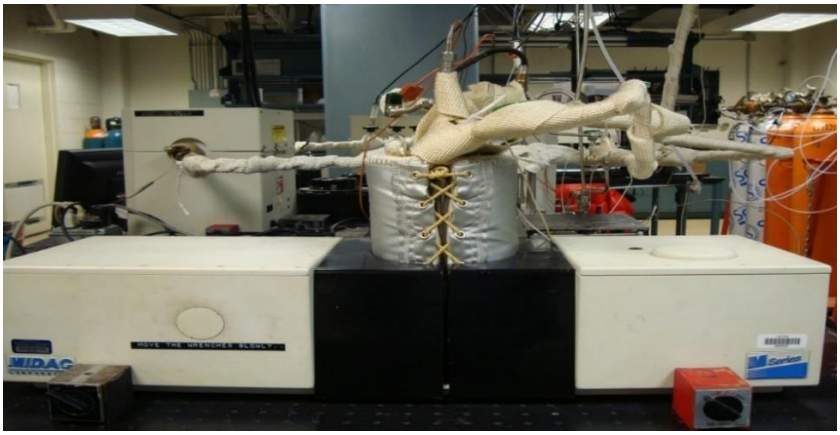

Figure 3.11 Photograph of the MIDAC M2000 Fourier transform infrared analyzer (FTIR, MIDAC M2000).

3.3 Bench-Flow Reactor Evaluation of Fresh and Aged Three-Way Catalysts (TWCs)

The bench-flow reactor (BFR) is used to evaluate the performance of fresh and engine-aged three-way catalyst (TWC) samples. After accelerated aging on the engine bench, the front section of engine-aged TWC samples is used for performance evaluation on the BFR, since the front section is expected to be the most contaminated from the engine lube-oil additives. For BFR evaluation, the TWC samples of 22 mm in diameter and 25.3 mm long are cored from the center of the front section of accelerated engine-aged TWC samples. The cored samples have approximately 290 cells. Exhaust gas simulation concentrations and TWC performance tests are performed with reference to the Crosscut Lean Exhaust Emissions Reduction Simulations (CLEERS) protocols.

3.3.1 Start-up Procedures for Bench Flow Reactor (BFR)

Prior to performing the evaluation on the bench flow reactor (BFR), the stainless-steel tubing, the steam generator furnace, and the FTIR sample cell are preheated to the required temperatures of 180, 300, and 200°C, respectively using heating tapes and preheater. To minimize the use of expensive research-grade gases, only house air is used to circulate in the BFR during warm-up. In order to stabilize the FTIR analyzer, it is necessary to wait a little longer even after the sample cell temperature reaches the target temperature of 200°C. Once preheating and stabilization of the FTIR are achieved, a gas mixture of N_2, CO_2, and steam vapor or N_2 gas is passed through the by-pass line to obtain the FTIR background spectrum necessitated by the experiment type. The concentration of

all target gas species – such as NO, NO_2, CO, C_3H_6, C_3H_8, CO_2, NH_3, and N_2O – is confirmed by FTIR's standard calibration curve for each gas species that flowed through the by-pass line. Once the desired temperatures are reached and the concentration of each gas is verified, the performance evaluation of the fresh and engine-aged TWC samples on the BFR is initiated.

3.3.2 Procedure De-greening of Fresh Sample and De-sulfating of Engine-aged Samples

Before performance evaluation on the BFR fresh TWC sample is subjected to the degreening process. The purpose of the de-greening process is to stabilize the fresh TWC sample such that repeatable results can be obtained. On the other hand, degreening is not needed for accelerated engine-aged TWC samples since they have already stabilized at high temperatures for long periods of time during the accelerated aging process. The gas composition during the degreening process consists of 10% CO_2, 10% H_2O, and N_2 balance at a GHSV of 60,000 h^{-1} and gas inlet temperature of 700°C for four hours.

The purpose of this study is to investigate the impact of lubricant additives on the performance of the TWCs. As mentioned in Section 3.1.3, all engine lubricant additives (ZDDP1, ZDDP2, IL, IL+ZDDP1, and IL+ZDDP2) are exposed to a TWC based on the same amount of P during accelerated aging. However, even though the amount of S contained in the fuel is small (less than 30 ppm), it may still have adverse effects on the performance of the TWC. Since IL does not contain S compounds, minimizing the S compounds on the catalyst to exclude the influence of S is important when comparing the impact of P component of the IL and ZDDP engine additives on the TWCs. Therefore, the desulfation process

is carried out on the BFR prior to the performance evaluation of all accelerated engine-aged TWC samples. It is known that S poisoning can be reversible under the lean condition at high temperatures. Thus, the desulfation is performed at a gas inlet temperature of 700°C using a slow cycle consisting of 2 minutes lean and 2 minutes rich for a total of two hours. The lean cycle consists of 0.3% O_2, 0.2% H_2, 13% H_2O, and N_2 balanced, whereas the rich cycle consists of 0.3% O_2, 1.0% CO, 13% H_2O, and N_2 balanced at a GHSV of 60,000 h^{-1}.

3.3.3 Bench-Flow TWC Evaluation Protocol

Table 3.4 provides gas compositions and concentrations for different combustion engine cases. The simulated gas composition of the S-GDI combustion mode is used in this study. Also, in the present study, two types of hydrocarbons (HCs): propylene (C_3H_6) and propane (C_3H_8), are used to represent high and less reactive HC in the simulated engine exhaust gases, respectively.

Table 3.4 Simulated engine exhaust compositions for gasoline engines from CLEERS protocols [141].

Constant components	**S-GDI (Stoichiometric GDI)**	**L-GDI (Lean gasoline direct injection)**	**LTC-G (Low temperature combustion of gasoline)**
O_2	0.74%	9%	12%
H_2O	13%	8%	6%
CO_2	13%	8%	6%
Variable components (ppm)			
CO	5000	2000	2000
NO	1000	500	100
Hydrocarbon (ppm) on C_1 basis (the concentrations in parenthesis are used for the liquid HC species)			
Total HC	3000		
C_2H_4	700 (1050)		
C_3H_6	1000 (1500)		
C_3H_8	300 (450)		
i-C_3H_{18}	1000		

3.3.3.1 Oxygen Sweep Experiment

As mentioned in Section 1.3, the performance of TWCs for the conversion of NO, CO, and UHCs is most efficient at a stoichiometric condition. As the air-fuel ratio (AFR) increases slightly to a lean condition, the NO concentration will suddenly increase. Thus, for a given composition of the exhaust gases consisting

of C_3H_6, C_3H_8, CO, and NO, the O_2 concentration at stoichiometric can be calculated theoretically using the definition of stoichiometric reaction, in which the only species in the products are H_2O, CO_2, and N_2. The simulated exhaust gases consist of 850 ppm C_3H_6, 100 ppm C_3H_8, 0.5% CO, 0.1% NO, 0.167% H_2, 13% H_2O, 13% CO_2, and balanced N_2. Equation 3.2 shows the stoichiometric reaction between the simulated exhaust gases and oxygen.

$$\begin{aligned} &\mathbf{0.13\ CO_2 + 0.13\ H_2O + 0.00167\ H_2 + 0.001\ NO + 0.005\ CO +} \\ &\mathbf{0.00001\ C_3H_8 + 0.00085\ C_3H_6 + 0.73138\ N_2 + 0.0072\ O_2} \\ &\mathbf{\rightarrow 0.13462\ H_2O + 0.13785\ CO_2 + 0.73138\ N_2} \end{aligned} \tag{3.2}$$

Equation 3.3 shows the percentage of O_2 in the stoichiometric condition.

$$\boldsymbol{O_{2,stoich}} = \frac{(\mathbf{0.0072})}{\mathbf{1} + (\mathbf{0.0072})} * \mathbf{100} \ = \ \mathbf{0.72}\ \% \tag{3.3}$$

However, the actual O_2 concentration is slightly different from the theoretical value due to experimental error. Therefore, in order to determine the exact concentration of O_2 at a stoichiometric condition where maximum conversion of CO, C_3H_6, C_3H_8, and NO is obtained, an oxygen sweep with a concentration of O_2 (varying between 0.4 and 0.8%) in the simulated exhaust gases is performed on the fresh and accelerated engine-aged TWC samples at an inlet gas temperature of 500°C and a GHSV of 60,000 h^{-1}.

3.3.3.2 Temperature Sweep Experiment

Once the O_2 concentration at stoichiometric condition is determined, the light-off temperature ramps are performed on all TWC samples with O_2 concentration in the simulated exhaust gases corresponding to the stoichiometric condition. Figure 3.12 shows the protocol of the temperature profile used for the temperature sweep experiment. The light-off temperature ramps are carried out for all TWC samples, which are performed by ramping up the furnace temperature from 100°C to 600°C at 5°C per minute and cooling down the furnace while holding its temperature at 130°C. The temperatures at 50% (T50) and 90% (T90) conversion for CO, C_3H_6, C_3H_8, and NO are obtained from the light-off temperature ramps, and from which the impact of lubricant additives on the performance of TWCs can be assessed. In addition, the formation of NH_3 and N_2O provides information that can help to understand the reaction pathway associated with NO species at temperatures between 100°C and 600°C.

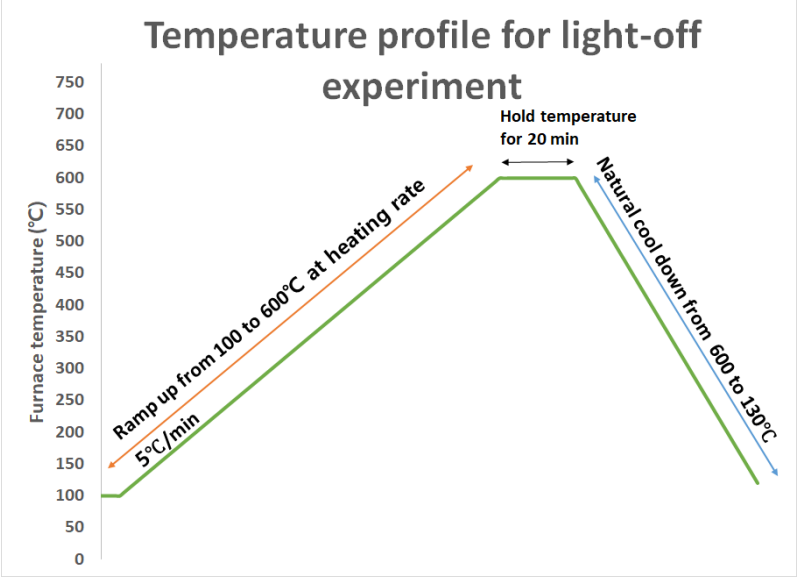

Figure 3.12 Temperature profile for temperature sweep experiment.

3.3.3.3 Water Gas Shift (WGS) Reaction Experiment

Additionally, the impact of anti-wear additives on the water gas shift (WGS: $CO+H_2O \rightarrow H_2+CO_2$) reaction for fresh and accelerated engine-aged TWC samples are investigated in the temperature range between 200°C and 550°C in 50°C increments, using a mixture consisting of 0.5% CO, 13% H_2O, and balanced N_2 at a GSHV of 60,000 h^{-1}. This reaction is one of the most important reactions over the TWC under fuel-rich conditions, in which CO and H_2O in the exhaust gas are consumed as well as H_2, and which affects the reduction of NO by the formation of NH_3 and/or N_2O.

3.3.3.4 Oxygen Storage Capacity (OSC) Experiment

The impact of lubricant additives on ceria (CeO_2), the oxygen storage material and one of the key constituents of the TWC's washcoat, is investigated by the oxygen storage capacity (OSC) experiment. The experiment is carried out for fresh and accelerated engine aging samples in a temperature range from 300°C to 550°C in 50°C increments using a slow cycle consisting of 2 minutes lean and 2 minutes rich for a total of 4 cycles in a total duration of 16 minutes. The lean cycle consists of 0.72% O_2 and N_2 balance, whereas the rich cycle consists of 0.5% CO and N_2 balance at a GSHV of 60,000 h^{-1}.

3.4 Surface Characterization Studies

In order to determine the effects of contaminants from anti-wear additives on the change of material properties of the TWC's washcoat, fresh and accelerated engine-aged TWC samples are characterized using electron probe microanalysis (EPMA), powder X-ray diffraction (XRD), Brunauer-Emmett-Teller (BET) surface area measurements, and inductively coupled plasma-mass spectrometry/optical emission spectroscopy (ICP-MS/OES). The results from the surface characterization studies can then be correlated with the performance degradation, from which the deactivation mechanisms can be elucidated.

3.4.1 Electron Probe Microanalysis (EPMA)

Electron probe microanalysis (EPMA) is used to obtain qualitative elemental maps and quantitative concentration profiles or line-scans of Mg, Al, Si, P, S, Zn, Fe, Zr, Ca, Ce, and O at a cross-section of the washcoat. The operation principle of EPMA is that electrons accelerated by a certain accelerating voltage (15-20 kV) from a probe (such as an electron beam) or electron gun collide with a specimen and emit not only heat but also scattered electrons and X-rays. The schematic of the EPMA structure and signals emitted when accelerated electrons impact on a specimen are shown in Figure 3.13. When the electron beam bombards the specimen, characteristic X-rays, elastic scattering (back-scattering electrons (BSE)), inelastic scattering (secondary electrons (SE)), cathodoluminescence (CL), etc., are generated. Elastic scattering changes the trajectory of the beam electrons in the specimen without changing the electrons' energy, whereas inelastic scattering transfer energy from

the beam electrons to the atoms of the specimen without changing the direction. The SE come from atoms that have absorbed the energy of the electron beam and can be used to obtain high-resolution images of the specimen surface. On the other hand, the BSEs reflect off the specimen and from deeper within the specimen and produce a composition map of the sample, which is useful for analyzing multiphase samples. A schematic of the X-ray generation process is shown in Figure 3.14. The characteristic X-ray is generated as follows: Firstly, the electrons from the primary beam remove an electron from one of the inner shells, resulting in an ionized and unstable state of the atom. Secondly, the ionized atom, which becomes unstable by forming inner shell vacancy from which the electron is removed, restores stability when the vacancy is filled from an electron from the outer shell, and the X-ray photon is emitted. The difference in the ionization energy of the electrons associated with the transition is equal to the energy of the emitted X-ray, called the characteristic X-ray. Since each element has specific ionization energies for each subshell, the difference between the energies is a characteristic of the elements involved in the generation of X-ray photons, and EPMA uses this principle to analyze the sample components and the amount of each element. An energy dispersive spectrometer (EDS) and a wavelength dispersive spectrometer (WDS) are used as X-ray detectors for qualitative and quantitative analysis. Additionally, SE and BSE are employed to obtain an image of the specimen. The BSE image, especially, is widely used for EPMA analysis since it can reveal a rough compositional distribution of the specimen.

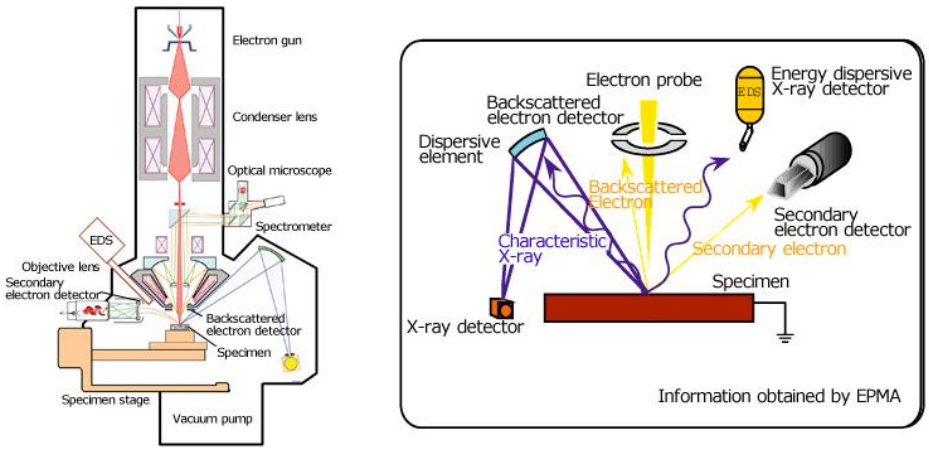

Figure 3.13 Schematic of EPMA structure and produced signal impinging on a specimen [142].

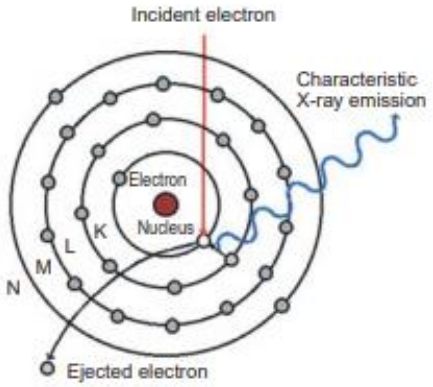

Figure 3.14 Schematic of the mechanism of characteristic X-ray generation [143].

The image of the elemental micrograph shows the qualitative distribution of elements in the catalyst. Therefore, using EPMA analysis, it is possible to identify structural damage of the γ-alumina washcoat (such as crackings and delamination) and Zn, S, and P poisoning of accelerated engine-aged TWCs. The EPMA instrument, a JXA-8200 (JEOL), is equipped with a backscatter detector and five wavelength dispersive spectrometers (WDS). Since more P and Zn deposition in the first 1 inch of the catalyst was observed in previous studies, analyzing the inlet section of the catalyst is important to reveal the effect of lubricant additives on the TWC samples. Therefore, to prepare for EPMA analysis, fresh and accelerated engine-aged TWC samples are divided into sections with a cross-section of about 1 cm from the inlet and analyzed using the central portion of the cross-sectional samples. The TWC sample is placed in a phenol ring and covered with resin to hold it in place. After the resin hardened, the surface of the sample is carefully polished to be flat and smooth using 1 μm diamond paste to ensure the accuracy of the analysis.

3.4.2 X-ray Diffraction (XRD)

X-ray diffraction (XRD) is employed to identify the chemical compound and crystalline phases of the samples and obtain particle size. XRD results when X-rays collide with atoms in a periodic lattice, and it is used to obtain information about the sample since diffraction angles and intensities are unique to the chemical compounds. Figure 3.15 shows a two-dimensional schematic of incident X-ray diffraction.

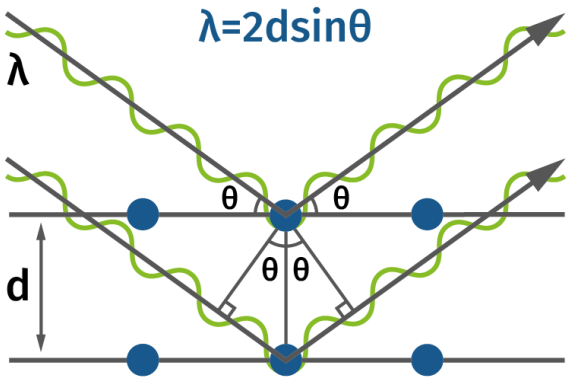

Figure 3.15 X-ray diffraction in 2-D [144].

When the crystal structure collides with the monochromatic X-ray radiation of wavelength (λ), Bragg reflections occur due to atomic lattice spacing (d), which acts as a three-dimensional diffraction grating that diffracts incident X-ray at specific angles. Bragg's Law, which expresses the relationship between the wavelength of incident X-rays (λ), the interplanar spacing of the crystal (d), the angle of incidence (θ), and the number of the reflections (n) is shown in Equation 3.4.

$$2\mathrm{d}\sin\theta = n\lambda, \qquad \mathrm{n} = 1, 2, 3, \ldots \tag{3.4}$$

Since θ is measured from XRD patterns, and λ is the characteristic wavelength of incident X-rays, the crystal spacing (d) can be calculated using the XRD pattern. In addition, the specimen can be identified from the calculated crystal spacing since each crystalline material has a unique d-spacing.

An XRD instrument mainly consists of an X-ray tube, a sample holder, and an X-ray detector. X-rays are produced when accelerated electrons strike a metal target. In the X-ray tube, a heating filament functioning as a cathode is used to produce electrons. The electrons are accelerated by supplying a high voltage, and these high-speed electrons bombard the anode metal (Cu, Fe, Mo, Cr), which is a ground potential. As a result, X-ray photons of characteristic energy and wavelength are produced when accelerated electrons dislodge inner shell electrons with enough energy. For single-crystal diffraction, the most commonly used target material for the anode is copper (Cu), and the characteristic wavelength of CuKα radiation is 1.5418 Å. While the detector is moving in a circle around the sample at a selected angle 2θ between 0 and 90°, the X-ray is directed towards the slowly rotating sample, and the intensity of the reflected X-ray is recorded at an angle of 2θ. The X-ray intensity in counts/s is measured by a detector and plotted against the angle of the incident X-ray (2θ = 0-90°).

Powder XRD is used to detect the physicochemical properties of the washcoat components, including average PGM crystallite size and phase transitions of γ-Al_2O_3 as a result of thermal aging. The sectioned samples are scraped to remove the γ-Al_2O_3 washcoat from the cordierite substrate. Approximately 20 mg of the washcoat is ground up and mixed with acetone in the cavity of a zero-background circular tray of 3.8 cm in diameter. Continuous theta-two theta (TTH) scans are performed on the PANalytical X'Pert diffractometer from 5 to 90° with a CuKα radiation source (λ=1.540598 Å) in a scan mode of 0.02° in 2s. For measurement, a 10 mm mask (beam length) coupled with 1/4˚ fixed slits, a 1/2˚ anti-scatter slit, and a 0.02 rad Soller slit is used. The diffractograms are analyzed with X'Pert Highscore® and Jade 6.5® using powder diffraction files (PDF) from the International Center for Diffraction Data (ICDD). The XRD patterns obtained are used to determine changes in the chemical

composition of γ-Al_2O_3 washcoat and the formation of sulfates, $AlPO_4$, $CePO_4$, and $Zn_2P_2O_7$ due to the lubricant additive exposure.

3.4.3 Physisorption (Brunauer-Emmett-Teller Surface Area, Pore size, and Pore-volume)

Physical adsorption, called physisorption, is the process in which gaseous atoms/molecules are adsorbed onto the surface of a solid at low temperatures that occur due to van der Waals forces. The electronic orbital patterns of the species involved are not significantly changed during physisorption. Physisorption is usually used to measure the BET surface area, pore size distribution, and pore volume in a solid. Physisorption is performed at an adsorption isotherm with increasing relative pressure (P/P_0) by using nitrogen (N_2) or argon (Ar) gas as an adsorbate at liquid nitrogen temperature of 77K and liquid argon temperature of 83K, respectively. The amount of vapor adsorbed when a relative pressure (P/P_0) is close to unity is used to derive the total pore volume by assuming the pores are filled with a liquid adsorbate. An adsorption isotherm of the amount of gas adsorbed by the material at a constant temperature is plotted as a function of relative pressures. Six different isotherms (IUPAC classification) are illustrated in Figure 3.16. The shape of the isotherms and the hysteresis loops describes the characteristics of the adsorbent, and Table 3.5 explains the characteristics of the adsorbent according to different types of isotherms.

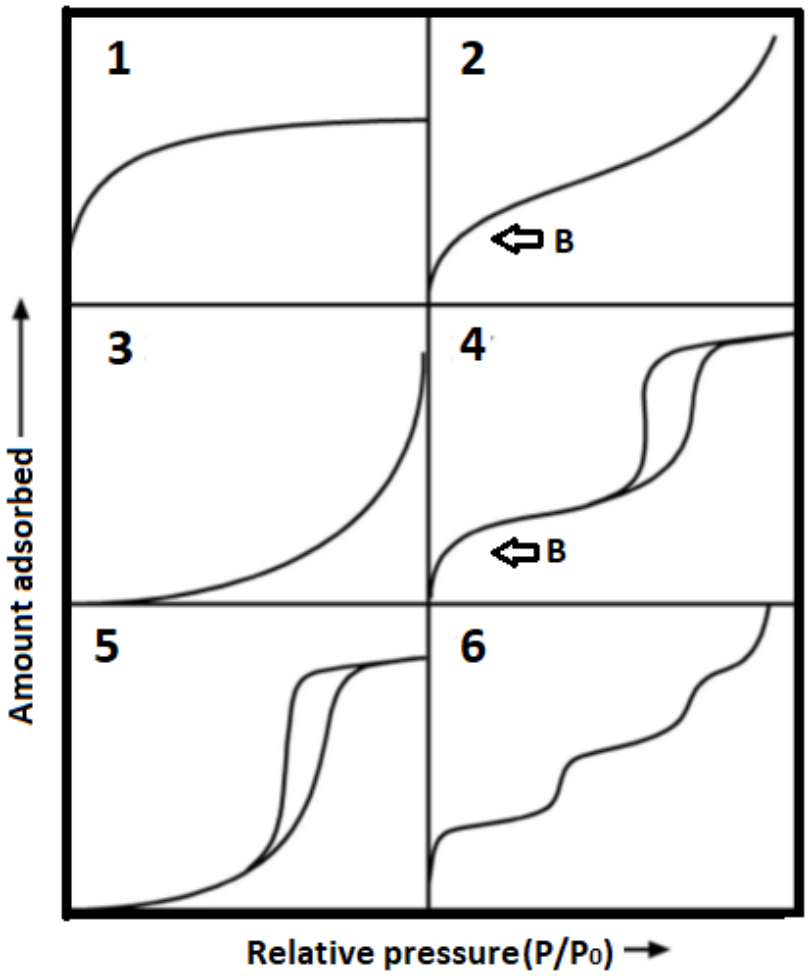

Figure 3.16 IUPAC classification of sorption isotherms [145].

Table 3.5 Describe the characteristics of the adsorbent for six different types of isotherms [145,146].

Type	Characteristics of adsorption
1	1. Microporous adsorbent 2. As regards the adsorbate uptake rate, the accessible micropore volume is more important than the total internal surface area
2	1. Non-porous or macroporous adsorbent (unrestricted monolayer-multilayer adsorption can occur) 2. The inflection point, called point B, indicates that the multilayer adsorption starts to occur from a monolayer coverage
3	1. Non-porous or microporous adsorbent 2. The adsorbate-adsorbate interactions play a more important role than adsorbate-adsorbent interactions
4	1. Mesoporous adsorbent 2. There is a hysteresis loop associated with the occurrence of pore condensation 3. The inflection point appears at the initial part of the type 4 as in case of the type 2
5	1. Mesoporous adsorbent 2. There is a hysteresis loop as in case of the type 4, but the adsorbent-adsorbate interactions are relatively weak due to the inflection point does not appear
6	1. Non-porous adsorbent with homogeneous surface (special case)
Note: macroporous (exceeding 500 Å in diameter), mesopores (between 20 and 500 Å in diameter), micropores (less than 20 Å in diameter)	

One of the most widely used methods to determine the surface area is the Brunauer-Emmett-Teller (BET) [147], which extends the Langmuir theory from a monolayer to multilayer adsorption using the following hypotheses:

1. Gas molecules physically are adsorbed on a solid (adsorbent) in multilayers
2. Only gas molecules in adjacent layers interact with each other
3. The Langmuir theory can be applied to each adsorption layer

Based on the hypotheses above, the BET equation is expressed as:

$$\frac{1}{W\left(\frac{P_0}{P}-1\right)} = \frac{1}{W_m C} + \frac{C-1}{W_m C}\left(\frac{P}{P_0}\right) \tag{3.5}$$

where P_0/P is the relative pressure, W is the weight of gas adsorbed at the relative pressure, W_m is the weight of monolayer adsorbed gas of surface coverage, and C is the BET constant.

The BET constant, C, is calculated using Equation 3.6.

$$\mathrm{C} = \exp\left(\frac{E_1 - E_L}{RT}\right) \tag{3.6}$$

where E_1 is the heat of adsorption for the first monolayer, and E_L is the heat of adsorption, which is equal to the heat of liquefaction or vaporization of the second or higher layers.

A typical BET plot is shown in Figure 3.17. The surface area of the sample can be determined using the BET equation (Equation 3.5) together with the information of Type 2 and 4 adsorption isotherms (see Figure 3.16). Typically, the BET plot is obtained using five data points in a relative pressure range between 0.05 to 0.35. If the BET plot is linear with a positive slope, then the BET method is suitable for obtaining the surface area.

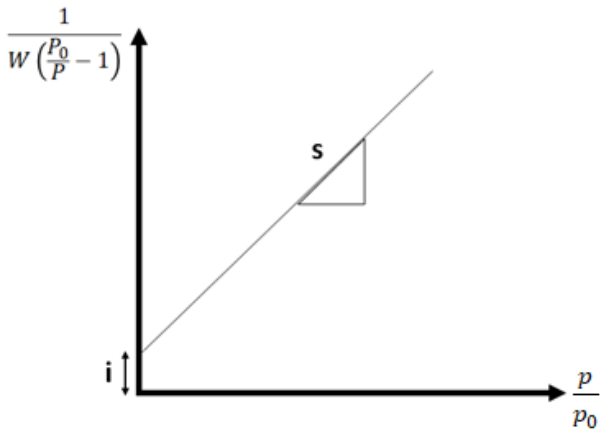

Figure 3.17 Typical example of the BET plot.

Equations 3.7 to 3.11 below are used to obtain the specific surface area, $S_{BET,}$ from the BET plot. The slope (s) and the y-intercept (i) can be obtained directly from the BET plot of Figure 3.17:

$$s = \frac{C-1}{W_m C} \tag{3.7}$$

$$i = \frac{1}{W_m C} \tag{3.8}$$

The weight of the monolayer adsorption gas of surface coverage, W_m, is obtained by combining Equations 3.7 and 3.8.

$$W_m = \frac{1}{s+i} \tag{3.9}$$

Once W_m is known, the total surface area, S_{total}, of the sample is calculated using Equations 3.10.

$$S_{total} = \frac{W_m \, N \, A_{cs}}{M} \tag{3.10}$$

where N is Avogadro's number, M is the molecular weight of the adsorbate, and A_{cs} is the cross-sectional area of the adsorbate. For N_2, the value of A_{cs} is taken to be 16.2 $Å^2$ when the N_2 monolayer is assumed to be hexagonally close-packed at 77K.

Finally, the specific surface area BET (S_{BET}) is calculated using Equations 3.11.

$$S_{BET} = \frac{S_{total}}{w} \tag{3.11}$$

where w is the weight of the solid sample (adsorbent).

BET surface area measurements of the TWC washcoat are performed in a Quantachrome gas sorption system (Autosorb iQ), from which the loss of surface area as a result of thermal aging and lubricant additive poisoning can be determined. Prior to gas adsorption analysis, the pretreatment is performed on approximately 500 mg TWC powder sample (washcoat only), which is placed in a quartz sample cell. The pretreatment referred to as degassing or outgassing process, is used to remove adsorbed moisture and other contaminants from the powder sample. In this study, the degassing process is performed at 180°C for 3 hours under a flow of a mixture of He and N_2. Once degassed, the weight of the sample is measured again, and then the sample cell with the degassed powder sample is transferred to the analysis station where it is submerged in liquid nitrogen. The adsorption isotherm (amount of adsorbate as a function of relative

pressure) is obtained by performing N_2 adsorption experiments at a liquid nitrogen temperature of 77K. In addition, the desorption isotherm is obtained by decreasing relative pressures. Pore size distribution and specific pore volume are calculated from the desorption isotherms by the Barrett, Joyner, and Halenda (BJH) method [148].

3.4.4 Inductively Coupled Plasma (ICP) Spectroscopy

Inductively coupled plasma (ICP) analyzer is a surface characterization technique used to detect and measure the chemical elements present in the samples using plasma and a spectrometer. Gas atoms are separated by positive ions (cations) and electrons at high temperature, and plasma flame is generated when the high frequency is introduced into induction coils, which induce electric field and magnetic field. A schematic of the plasma torch for generating the plasma is shown in Figure 3.18. Generally, ICP uses argon gas as a plasma gas, and the plasma is generated by the interaction of a radiofrequency field (RF field) and argon gas. The plasma temperature can reach a maximum temperature of approximately 10,000K, and at such a high temperature, the crystalline elements of the sample can be completely atomized.

In this study, inductively coupled plasma mass spectrometry (ICP-MS) and inductively coupled plasma optical emission spectroscopy (ICP-OES) are used for measuring all the chemical elements present in the fresh and accelerated engine-aged TWC samples quantitatively. The TWC powder sample is fused with sodium peroxide (Na_2O_2) over a Bunsen burner and then dissolved in water. The resulting solution is acidified and delivered to a spray chamber by a peristaltic pump to form an aerosol. The aerosol is led to a high-temperature argon plasma

generated at the tip of a quartz tube by an induction coil through which an alternate current flow. Due to the high temperature of the plasma (~6000-7000K), ionization of the sample takes place from which high-energy electrons are liberated. As the high-energy electrons drop to the lower energy levels, photons at certain wavelengths are emitted. Each element possesses its own characteristic emission spectrum, and thus, the spectrum can be acquired with a spectrometer to determine the type and concentration of the element. In this manner, ICP-OES can be used to measure the total concentration of S, P, Zn, Pd, Rh, etc. in fresh and accelerated engine-aged TWC samples.

Similarly, for ICP-MS, the prepared sample solution is introduced into a peristaltic pump for delivering to a spray chamber, and the aerosol is injected into an argon-plasma. However, unlike ICP-OES, the ions from the argon-plasma are separated according to their mass-to-charge ratio using a quadrupole mass spectrometer (MS), and the concentration of elements is measured by a detector in proportion to the ion signal. ICP-MS analysis is best to employ in situations in which a large number of elements and their amounts are required to be identified. For this reason, in the present study, ICP-MS analysis is used to measure 60 elements in a fresh TWC sample, from which the chemical makeup of fresh TWC can be identified. On the other hand, for TWCs exposed to lubricant additives, only selective chemical elements such as P, S, and Zn, the major components of lubricant additives, are of particular interest; and they can be easily measured by ICP-OES analysis.

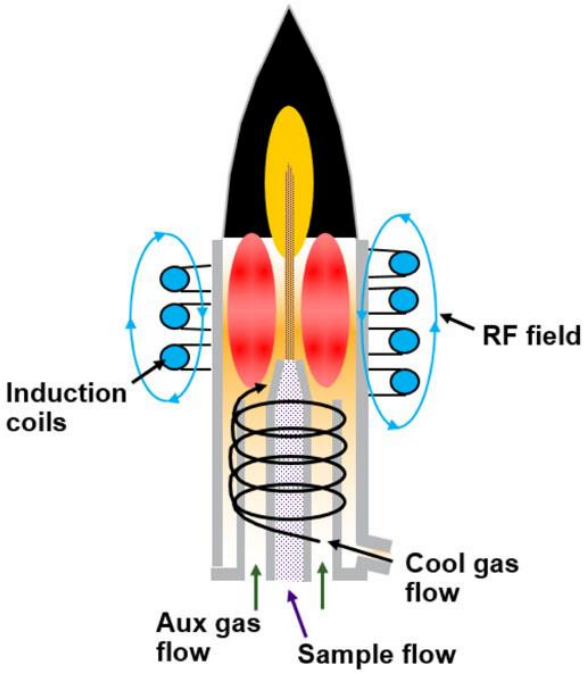

Figure 3.18 Plasma torch [149].

CHAPTER 4
RESULTS AND DISCUSSION

This chapter is divided into two main sections and devoted to the discussion of the results obtained from the current study. Section 4.1 addresses the performance and material characterization of fresh and NA-aged TWCs, from which the deactivation mechanisms due to thermal aging is identified. The effects of poisoning of various types of lubricant additives such as primary ZDDP (ZDDP1), secondary ZDDP (ZDDP2), IL and mixed additives of IL and ZDDP (IL+ZDDP1 and IL+ZDDP2) on the performance and material characterization of Pd-based TWCs are presented in Section 4.2. The NA-aged TWC sample is used as a baseline, to which the performance and material characterization of Pd-based TWCs exposed to lubricant additives are compared. Only in this manner, the effects of thermal aging on the performance of Pd-based TWCs can be isolated from those of poisoning from lubricant additives. The performance of all TWCs is evaluated on a bench flow reactor (BFR) using the protocols prescribed by CLEERS. In addition, the surface characterization techniques such as inductively coupled plasma (ICP) analysis, Brunauer-Emmett-Teller (BET) surface area, pore-volume, pore size distribution, electron probe microanalysis (EPMA), and X-ray diffraction (XRD) are used to identify the deactivation mechanisms and morphological changes in the accelerated engine-aged TWC samples.

4.1 Fresh and No-Additive (NA) TWC Samples (Thermal Aging)

The accelerated aging of an NA-aged TWC sample is performed on a gasoline engine bench for 24 hours with a catalyst midbed temperature at 700°C. Although such temperature is not high enough to induce a phase transformation of the washcoat (γ-Al_2O_3 to α-Al_2O_3), it can still cause a reduction of the washcoat surface area and sintering of precious metals through thermal deactivation. Before the performance evaluation with a bench flow reactor (BFR), the fresh sample is degreened, and the NA-aged TWC sample is desulfated according to the protocols described in Section 3.3.2. Figure 4.1 shows typical temperature profiles of the inlet and exit gas streams as well as the catalyst's midbed of the NA-aged TWC sample for four lean/rich cycles during desulfation. The furnace temperature is set between 770°C and 775°C so that the catalyst midbed temperature reaches 700°C during the lean cycle (0.3% O_2, 0.2% H_2, 13% H_2O, and balance N_2). As seen in Figure 4.1, during the rich and lean cycle, the inlet and outlet gas temperature profiles only slightly change within 10°C. On the other hand, during the rich cycle (0.3% O_2, 1.0% CO, 13% H_2O, and balanced N_2), the midbed catalyst temperature increases from 700°C to 740°C due to the exothermic CO oxidation reaction on the washcoat of the TWC.

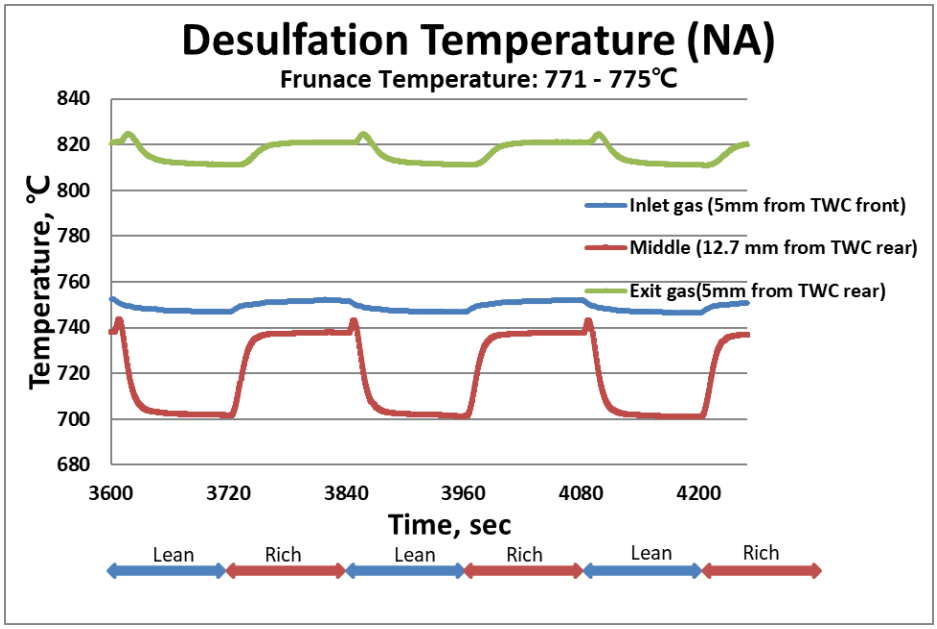

Figure 4.1 Typical temperature profiles at the inlet, middle, and exit of NA-aged TWC sample in four lean/rich cycles during desulfation.

4.1.1 Performance Evaluations on Bench-Flow Reactor (BFR)

Oxygen sweep experiment is performed on the degreened fresh and desulfated NA-aged TWC samples at an inlet gas temperature of 500°C with O_2 concentration varying between 0.4 and 0.8% (fuel-rich to fuel-lean). The main purpose of the oxygen sweep experiment is to determine the exact O_2 concentration at the stoichiometric condition. Because the conversion of NO is maximum at the stoichiometric condition and decreases drastically with increasing O_2 concentration (lean condition), the point at which the NO concentration begins to increase is taken to be the stoichiometric condition. Once

the concentration of O_2 at stoichiometric condition is determined, a temperature sweep is performed on both samples at the stoichiometric condition by increasing the furnace temperature from 100°C to 600°C at a rate of 5°C per minute. Simultaneously, the concentrations of CO, C_3H_6, C_3H_8, NO, N_2O, and NH_3 are measured, from which the conversion of CO, C_3H_6, C_3H_8, and NO as a function of temperature is obtained in the form of the light-off curve. From the light-off curve, temperatures at 50% (T50) and 90% (T90) conversion for CO, C_3H_6, C_3H_8, and NO are obtained, from which the impact of thermal aging on the TWC performance is evaluated. Additionally, the effect of thermal aging on the water gas shift (WGS, $CO+H_2O \rightarrow H_2+CO_2$) reaction for both fresh and NA-aged TWC samples is investigated at inlet gas temperatures between 200°C and 550°C in 50°C increments. The WGS reaction is one of the most important reactions that not only affects CO conversion but also produces H_2, which is a NO reductant. Finally, oxygen storage capacity (OSC) is performed on both samples to investigate the impact of thermal aging on ceria (CeO_2), which is the oxygen storage material.

As mentioned in Section 3.3.3.1 of Chapter 3, the point at which the NO concentration begins to increase is used to determine the concentration of O_2 at the stoichiometric condition. Figure 4.2 shows the effect of O_2 concentration on the conversion of NO, CO, C_3H_6, and C_3H_8, as well as the formation of NH_3, N_2O, and NO_2 at an inlet gas temperature of 500°C for the fresh TWC sample. A temperature of 500°C is selected to ensure the conversion of NO, CO, C_3H_6, and C_3H_8 to be at least 90% at the stoichiometric condition. As shown in Figure 4.2 (b), a drastic increase in NO concentration is observed at an O_2 concentration of 0.73%, which is indicative of the stoichiometric condition, whereas the concentrations of CO, C_3H_6, C_3H_8, NH_3, and N_2O are minimum.

Below stoichiometric in the fuel-rich condition, since the oxidation of CO is low when O_2 is insufficient, in the fuel-rich conditions (below stoichiometric), CO is preferentially reduced by WGS reaction and NO-CO reduction reaction rather than by oxidation reaction. In addition, CO, CO_2, and H_2 can be produced by the steam reforming reaction (SR, $C_mH_n + H_2O \rightarrow CO_2 + H_2$) from UHCs such as C_3H_6 and C_3H_8, over Pd under fuel-rich conditions. As a result, CO concentration is very high in fuel-rich conditions and readily reacts with water vapor to produce H_2 from the WGS. In the fuel-rich condition, H_2 is also produced from the SR reactions, and in the absence of O_2, H_2 produced from both WGS and SR reactions reacts with NO to yield NH_3, as seen in Figures 4.2 (a) and (b). As the O_2 concentration increases from 0.4 to 0.73%, the oxidation reaction of H_2 and CO produced from WGS and SR reactions with O_2 becomes more dominant, resulting in a decrease in CO and NH_3.

Beyond stoichiometric in the fuel-lean condition, the oxidation of NO reductants such as CO, C_3H_6, C_3H_8, H_2, etc. is more preferential than the reduction reactions, resulting in a lack of NO reductants and consequently an increase in NO concentration. Furthermore, in the fuel-lean conditions, NO_x can be converted to N_2O and N_2 when H_2 is deficient (H_2 / NO_x <2.5) [150,151], and a small amount of N_2O is produced under oxygen-rich conditions (O_2 concentrations above 0.73%).

The oxygen sweep experiment is also performed on the NA-aged TWC sample under similar conditions. As seen in Figures 4.3 (a) and (b), a similar trend is observed in the concentration of CO, C_3H_8, NO, and N_2O as the O_2 concentration is varied. At stoichiometric condition, the O_2 concentration for the NA-aged TWC is found to be 0.74%, which is similar to that of the fresh TWC sample.

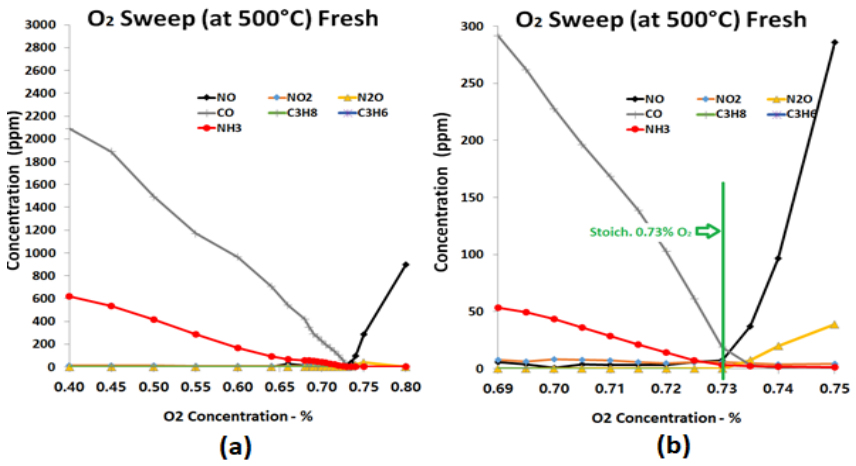

Figure 4.2 Oxygen sweep with O_2 concentration varying between 0.4 to 0.8% for fresh TWC sample at 500°C (a) full scale and (b) zoomed in.

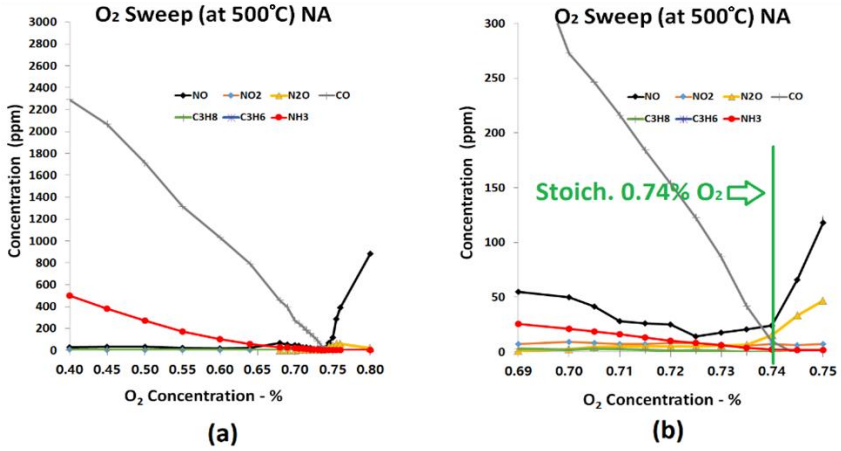

Figure 4.3 Oxygen sweep from 0.4 to 0.8% of O_2 for the NA-aged TWC sample at 500°C (a) full scale and (b) zoomed in.

Figures 4.4 (a) through (f) show the effect of O_2 concentration on the concentration of NO, CO, C_3H_6, C_3H_8, NH_3, and N_2O for both fresh and NA-aged TWC samples at an inlet gas temperature of 500°C, respectively. As seen in Figures 4.4 (a), (b) and (d), the NA-aged TWC sample results show a higher concentration or a lower conversion of NO, CO, and the least reactive C_3H_8 than the fresh TWC sample as the O_2 concentration is varied between 0.4 and 0.8%. On the other hand, the conversion of the more reactive C_3H_6 for both fresh and NA-aged TWC samples is 100%. The reduction in the performance of the NA-aged TWC sample can be attributed to the sintering of Pd particles and the reduction of the surface area of the γ-Al_2O_3 washcoat as a result of thermal aging. The reduction in the surface area of the NA-aged TWC sample will be shown in terms of BET surface areas in Section 4.1.2. In the fuel-rich condition with the O_2 concentration below the stoichiometric condition of 0.73%, the fresh TWC sample exhibit a higher concentration or formation of NH_3 than the NA-aged TWC sample, as seen in Figure 4.4 (e). At high temperatures, the formation of NH_3 from NO and H_2 is traditionally expressed by the following reaction pathway [151,152]:

$$NO + 2.5H_2 \rightarrow NH_3 + H_2O \qquad (4.1)$$

In Equation 4.1, H_2 required for the formation of NH_3 is produced from WGS reaction as well as SR reaction of C_3H_6 and C_3H_8, both under fuel-rich conditions at an inlet gas temperature of 500°C. As will be seen later in Figure 4.8, at an inlet gas temperature of 500°C, the reaction rate of the WGS reaction is highest, and thus the amount of H_2 produced is largest. Under fuel-rich conditions and in the presence of CO, NO, and H_2, NH_3 can also be formed by an additional reaction pathway described by Equation 4.2 [151].

$$NO + CO + 1.5H_2 \rightarrow NH_3 + CO_2 \quad (4.2)$$

According to Oh et al. [151], the presence of CO and H_2O increases the formation of NH_3 due to additional H_2 produced from the WGS reaction. In the NA-aged TWC sample, less H_2 is produced from the WGS reaction due to the sintering of Pd particles and hence the reduction of Pd reactive sites as a result of thermal aging. Thus, the formation of NH_3 for the NA-aged TWC sample is less than that for the fresh TWC sample at fuel-rich conditions.

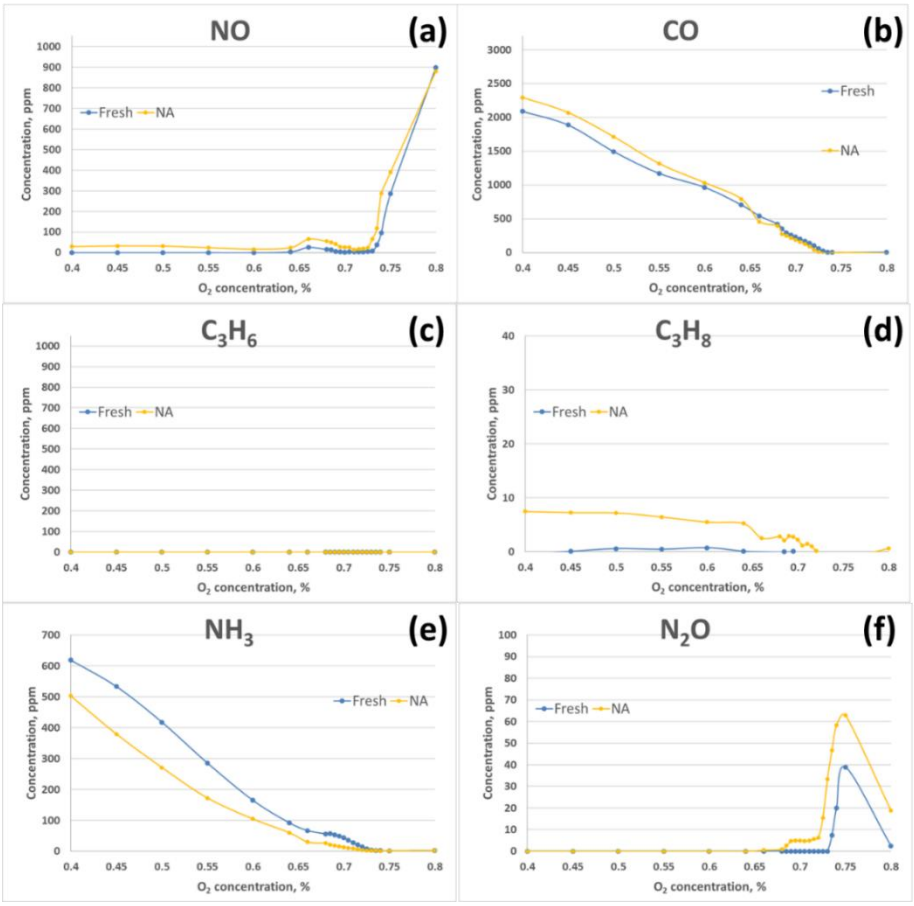

Figure 4.4 Effects of O_2 concentration on the concentration of (a) NO (b) CO (c) C_3H_6 ,and (d) C_3H_8 and formation of (e) NH_3 and (f) N_2O for fresh and NA-aged TWC samples with O_2 concentration varying from 0.4 to 0.8%.

Once the O_2 concentration at stoichiometric condition is determined from the oxygen sweep experiment, a temperature sweep experiment is performed, from which the light-off curves for both fresh and NA-aged TWC samples are obtained. From the light-off curves, the temperatures at 50% (T50) and 90%

(T90) conversion of NO, CO, C_3H_6, and C_3H_8 can be found for both samples. Figures 4.5 (a) to (d) show light-off curves for NO, CO, C_3H_6, and C_3H_8 of both fresh and NA-aged TWC samples, respectively. In addition, Figures 4.5 (e) and (f) show the formation of NH_3 and N_2O for both fresh and NA-aged TWC samples, respectively. As seen in Figure 4.5 (a), NO conversion after an initial increase shows a sudden decrease in the temperature range between 250°C and 330°C, during which the conversion of CO and C_3H_6 reaches a maximum of 100%, and NH_3 is no longer produced (see Figures 4.5 (b), (c), and (e)). Such results explain that within this temperature range, reductants for NO such as H_2, CO, or C_3H_6-- which are suitable for NO conversion-- are exhausted mainly due to oxidation reaction. Figure 4.5 (e) shows that the NA-aged TWC sample produces more NH_3 than the fresh TWC sample at temperatures between 150°C and 280°C, which is possibly related to the degradation of CO conversion in the NA-aged TWC sample. It has been reported that the presence of CO in the simulated gas can enhance due to oxidation NH_3 formation by providing an additional reaction pathway [153-157]. Furthermore, NH_3 can be produced at low temperatures in the range between 150°C and 280°C by the following overall reaction involving NO, CO, and H_2O:

$$2NO + 5\mathrm{CO} + 3H_2O \rightarrow 3NH_3 + 5CO_2 \qquad (4.3)$$

Based on the light-off curves in Figure 4.5, the temperatures at 50% (T50) and 90% (T90) conversion of NO, CO, C_3H_6, and C_3H_8 for both fresh and NA-aged TWC samples are obtained and plotted in Figures 4.6 (a) and (b), respectively. As can be seen in Figure 4.6 (a), the NA-aged TWC sample has higher T50 than the fresh sample for NO, CO, and C_3H_6 by 9, 10, and 9°C, respectively, but lower for C_3H_8 by 25°C. Furthermore, the NA-aged TWC sample has a higher T90 than the fresh TWC sample for CO and C_3H_6 by 10 and 11°C,

but lower for NO and C_3H_8 by 22 and 25°C as shown in Figure 4.6 (b). To account for the reduction in T50 of NO and C_3H_8 as well as T90 of NO for the NA-aged TWC sample compared with the fresh TWC sample. Figures 4.5 (a) and (f) show the delay of NO and higher formation of N_2O of the fresh TWC sample at temperatures between 300°C and 500°C. This indicates that an increase in T50 and T90 for NO and C_3H_8 in the fresh TWC sample is associated with higher N_2O formation in the same temperature range.

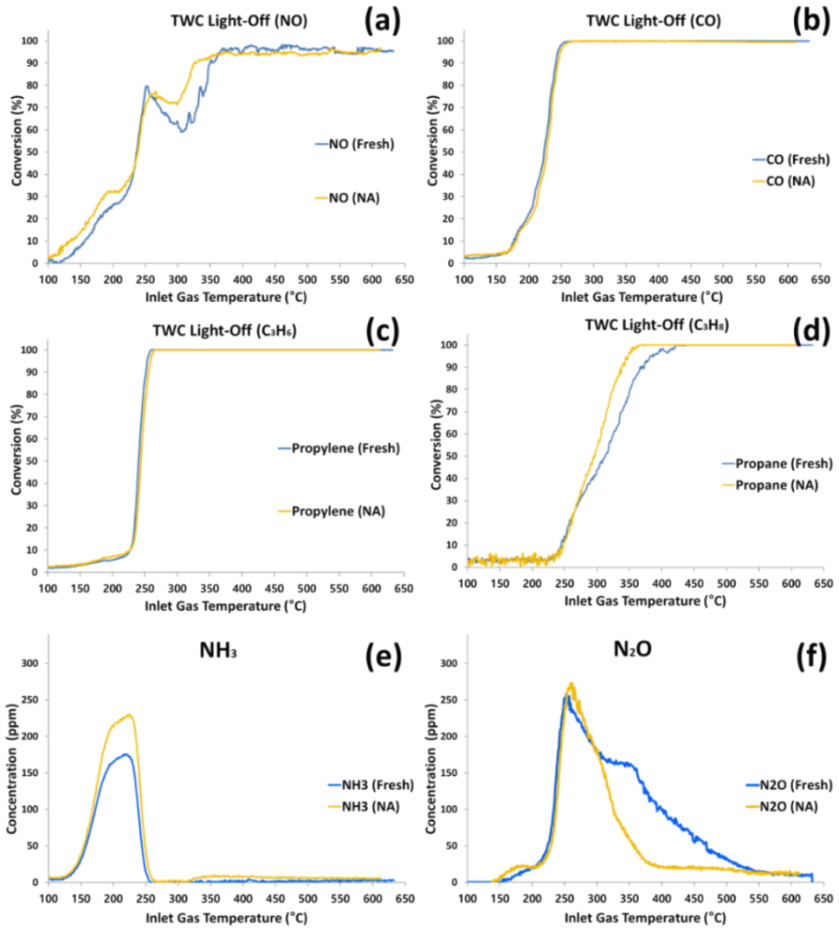

Figure 4.5 Effect of inlet gas temperature on the conversion (a) NO, (b) CO, (c) C_3H_6, and (d) C_3H_8, and the formation of (e) NH_3 and (f) N_2O for fresh and NA-aged TWC samples at stoichiometric condition of 0.73% O_2 with inlet gas temperature varying between 100°C and 640°C.

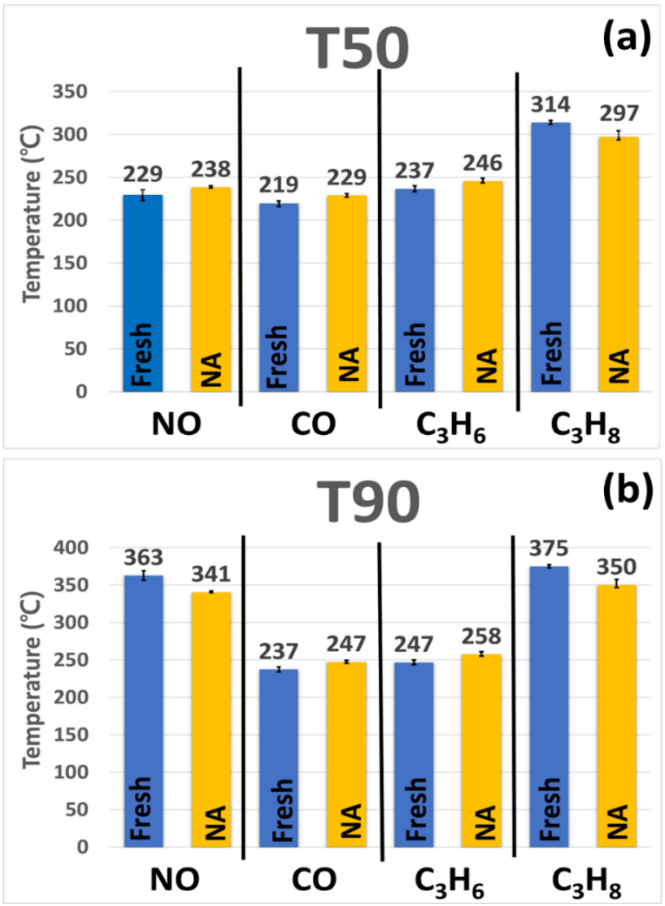

Figure 4.6 (a) T50 and (b) T90 of NO, CO, C_3H_6, and C_3H_8 for fresh and NA-aged TWC samples.

The effect of thermal aging on the oxygen storage capacity (OSC) of ceria is also investigated using the BFR. During the lean cycle, O_2 is stored in the mixed oxide ($Ce_xZr_{1-x}O_2$) and on the Pd sites, the stored O_2 is subsequently released and reacts with CO during the rich cycle to produce CO_2. OSC is calculated based on the amount of CO_2 produced. Figure 4.7 shows the OSC for

fresh and NA-aged TWC samples in the temperature range between 300°C and 550°C at a 50°C increment. The result in Figure 4.7 indicates that the degradation of the OSC performance of the NA-aged TWC sample is due to the agglomeration of cerium oxide and sintering of Pd particles at all temperatures investigated in the present study. A midbed temperature of 700°C achieved during accelerated engine aging is high enough for the agglomeration of CeO_2, causing a decrease in OSC [12,158]. Both fresh and NA-aged TWC samples reach their maximum performance at 450°C.

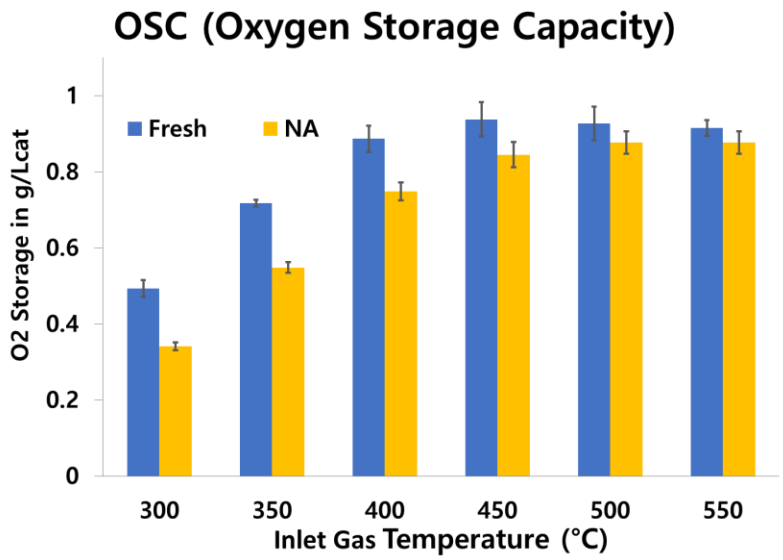

Figure 4.7 Oxygen storage capacity (OSC) for fresh and NA-aged TWC samples at temperatures between 300°C and 550°C.

The effect of thermal aging on the water gas shift (WGS) reaction ($CO+H_2O \rightarrow CO_2+H_2$) is also investigated. WGS is an essential reaction of TWC, where CO and H_2O react under fuel-rich conditions to produce H_2, a strong reductant of NO_x. Figure 4.8 shows the WGS for fresh and NA-aged TWC samples at temperatures between 200°C and 550°C at a 50°C increment. Since it is not possible to measure H_2, a homonuclear diatomic molecule, by the FTIR, the amount of H_2 produced is estimated by the amount of CO_2 produced. As shown in Figure 4.8, less CO_2 and consequently less H_2 is produced by the NA-aged TWC sample produces at temperatures between 350°C and 450°C due to the sintering of Pd, and agglomeration of CeO_2 [159-161]. It is well-known that the WGS reaction predominantly occurs on the surface of noble metals and that ceria further promotes this reaction [12,159,161–163].

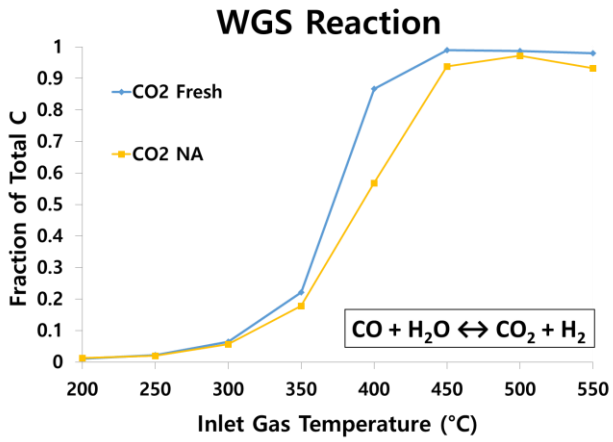

Figure 4.8 Formation of CO_2 in water gas shift (WGS) reaction for fresh and NA-aged TWC samples at temperatures between 200°C and 550°C.

4.1.2 Surface Characterization Analysis Results

In the present study, inductively coupled plasma optical emission spectroscopy (ICP-OES) is performed on both fresh and NA-aged TWC samples. Specifically, for the NA-aged TWC samples, ICP-OES is used to identify accumulated contaminants in the TWC washcoat and obtain the amount of accumulated contaminants by weight. The γ-Al_2O_3 of the TWC washcoat is crucial since its large surface area (~200m^2/g) would provide high dispersion for the Pd active sites. And the rate of CO and UHCs oxidation, NO_x reduction, and WGS reaction is dependent on the number of Pd active sites. For this reason, physisorption, from which BET for surface area measurement and BJH method for pore volume and pore size distribution are obtained, is used to quantify the effects of thermal aging on the reduction of the surface area of the washcoat. Additionally, X-ray diffraction (XRD) is used to detect the change in physicochemical properties of the washcoat components, including average PGM crystallite size and phase transitions of γ-Al_2O_3. Lastly, the electron probe microanalyzer (EPMA) provides a way to examine the relative zinc (Zn) and phosphorus (P) content and distribution in the washcoat of the TWC samples exposed to anti-wear (AW) additives. In this subsection, the deactivation mechanisms of thermally aged TWCs are identified using the surface characterization techniques mentioned above.

The ICP-MS analysis examines the type and quantity of noble metals, washcoat, promoters, and cordierite components used in the TWC. For the reasons given in Section 3.4.4, ICP-MS is used to analyze, identify, and quantify 32 elements present in the fresh TWC sample only. Table 4.1 shows the concentration of all elements detected from the fresh TWC sample determined from ICP-MS analysis. As seen in Table 4.1, the major elements detected are magnesium (Mg), aluminum (Al), zirconium (Zr), barium (Ba), and cerium (Ce),

which are the elements that form cordierite ($2MgO \cdot 2Al_2O_3 \cdot 5SiO_2$), γ-Al_2O_3 washcoat, and oxygen storage material (mixed oxides CeO_2-ZrO_2). Additionally, the precious metals, Pd and Rh, are detected at a ratio of 8:1. And more importantly, the amount of P—a major component in the IL and ZDDP additives—in fresh TWC sample is minute (<20 ppm). Figures 4.9 (a) and (b) show the ICP-OES results for P and Zn concentrations of fresh and NA-aged TWC samples, respectively. Although no lube oil additive is added to the fuel during accelerated-engine aging of the NA-aged TWC sample, a small amount of P is found in the NA-aged TWC sample from the exposure to the ZDDP additive from the Genset lube oil during the engine-bench aging. On the other hand, Zn, the other major component of the ZDDP additive, is not detected in either the fresh or the NA-aged TWC samples.

Table 4.1 Concentration of various elements in fresh TWC sample determined from ICP-MS analysis.

Mass Spec Semi-Quantitative Screen

GLI Sample ID B-2960 Sample Amt 257.53 mg
Data Sheet Final Volume 50 mL
Reference 1809 Dilution Factor 5

Element	Result	Element	Result
Lithium	8 ppm	Cadmium	<2 ppm
Beryllium	<2 ppm	Indium	<2 ppm
Boron	3 ppm	Tin	<2 ppm
Sodium	407 ppm	Antimony	<2 ppm
Magnesium	Major	Tellurium	<2 ppm
Aluminum	Major	Cesium	<2 ppm
Phosphorus	<20 ppm	Barium	Major
Potassium	72 ppm	Lanthanum	3687 ppm
Calcium	N/A	Cerium	Major
Scandium	12 ppm	Praseodymium	99 ppm
Titanium	711 ppm	Neodymium	19 ppm
Vanadium	<2 ppm	Samarium	2 ppm
Chromium	N/A	Europium	<2 ppm
Manganese	16 ppm	Gadolinium	2 ppm
Iron	N/A	Terbium	<2 ppm
Cobalt	3 ppm	Dysprosium	<2 ppm
Nickel	2458 ppm	Holmium	<2 ppm
Copper	<2 ppm	Erbium	<2 ppm
Zinc	30 ppm	Thulium	<2 ppm
Gallium	88 ppm	Ytterbium	<2 ppm
Germanium	N/A	Lutetium	<2 ppm
Arsenic	<2 ppm	Hafnium	475 ppm
Selenium	<2 ppm	Tantalum	<2 ppm
Rubidium	<2 ppm	Tungsten	<2 ppm
Strontium	181 ppm	Rhenium	<2 ppm
Yttrium	2687 ppm	Iridium	<2 ppm
Zirconium	Major	Platinum	5 ppm
Niobium	<2 ppm	Gold	<20 ppm
Molybdenum	7 ppm	Thallium	<2 ppm
Ruthenium	<2 ppm	Lead	3 ppm
Rhodium	603 ppm	Bismuth	<2 ppm
Palladium	4737 ppm	Thorium	4 ppm
Silver	4 ppm	Uranium	<2 ppm

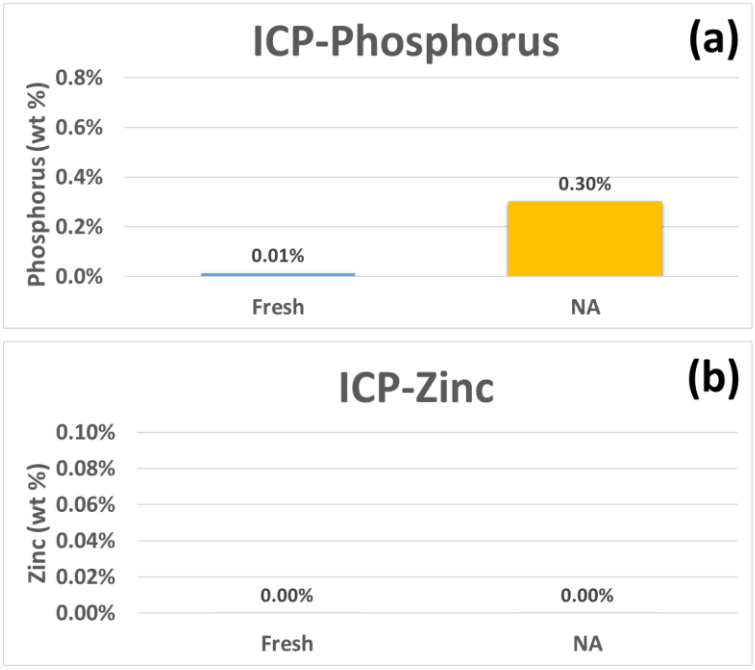

Figure 4.9 ICP-OES results of (a) P and (b) Zn in weight percent for fresh and NA-aged TWC samples.

The TWC washcoat's high surface area γ-Al_2O_3 support is important in keeping the Pd catalyst particles well-dispersed, and BET measurements are utilized to quantify the changes in surface area. As can be seen in Figure 4.10, the BET surface areas of fresh and NA-aged TWC samples are 99.2 m^2/g and 83.4 m^2/g, respectively, indicating the impact of thermal aging on the surface area of NA-aged TWC sample. Moreover, Figure 4.11 shows the BJH pore volumes (a) and pore sizes (b) of fresh and NA-aged TWC samples. Fresh and NA-aged TWC samples have a relatively similar pore size, but the pore-volume of the NA-aged TWC sample is 5.49% lower than that of the fresh TWC sample.

Such results indicate that the catalyst's temperature of 700°C during the aging process for 24 hours drops the surface area of the catalyst by 16% and pore volume by 5.5%.

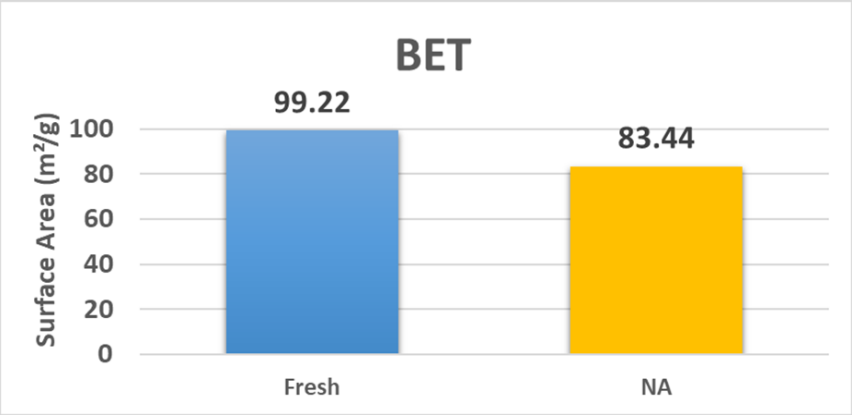

Figure 4.10 BET surface area measurements of fresh and NA-aged TWC samples.

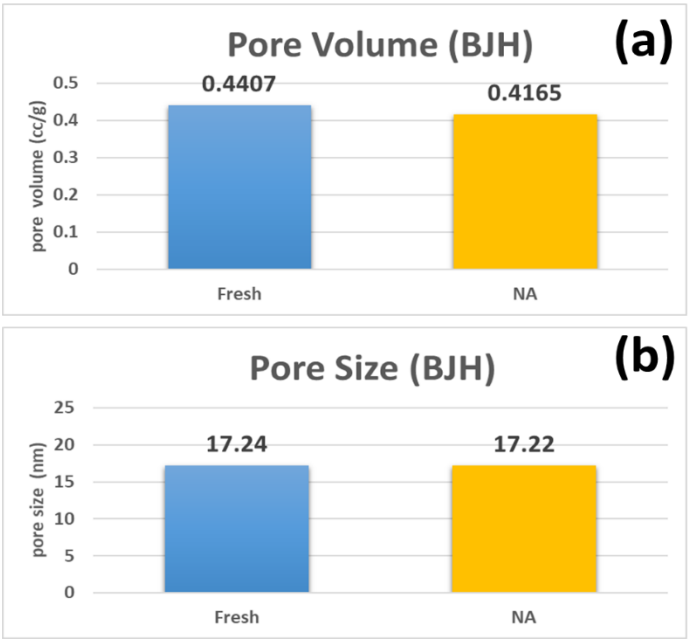

Figure 4.11 (a) Pore volume and (b) pore size (BJH method) measurements of fresh and NA-aged TWC samples.

Figure 4.12 shows the XRD patterns of the washcoat of fresh and NA-aged TWC samples. The peak denoted by (▼) at 2θ = 29.5° is assigned to the mixed ceria-zirconia oxide ($Ce_{1-x}Zr_xO_2$). The peaks denoted by (○) at 2θ = 10, 21.7, 26.4, and 28.5° indicates the presence of the remnant of the cordierite substrate in the washcoat powder. Despite considerable effort in removing the washcoat from the cordierite substrate, all samples inadvertently did contain a small amount of cordierite. The peaks at 20.4, 22.83, 24.91, 25.89, 26.89, 28.81, 31.57, 32.82, 36.23, 40.82, 42.65, 42.96 and 44.06° are assigned to $BaSO_4$ (■), a washcoat stabilizer [164]. Pd (◆) and PdO (●) peaks at 2θ = 39.6 and 33.9°,

respectively, are barely visible for both samples due to their small sizes. Even though trace amount of P, mainly from exposure to the engine lubricant additive during engine operation, is detected in the NA-aged TWC sample by ICP-OES and EPMA analysis, but peaks of P-contained compounds such as $Zn_2P_2O_7$ and $CePO_4$ are not detected in XRD patterns. In addition, the Pd peak at $2\theta = 39.6°$ is clearly visible for the NA-aged TWC sample but not for the fresh TWC sample, which attests to the sintering of Pd particles during thermal aging. Thus, the predominant deactivation mechanism of the NA-aged TWC sample is due solely to thermal aging rather than poisoning from lubricant additives. Therefore, the results of the NA-aged TWC sample from the BFR experiments, such as T50, T90, OSC, and WGS reaction, can be used as a baseline and compared to which the effect of additive poisoning on the performance of the TWC.

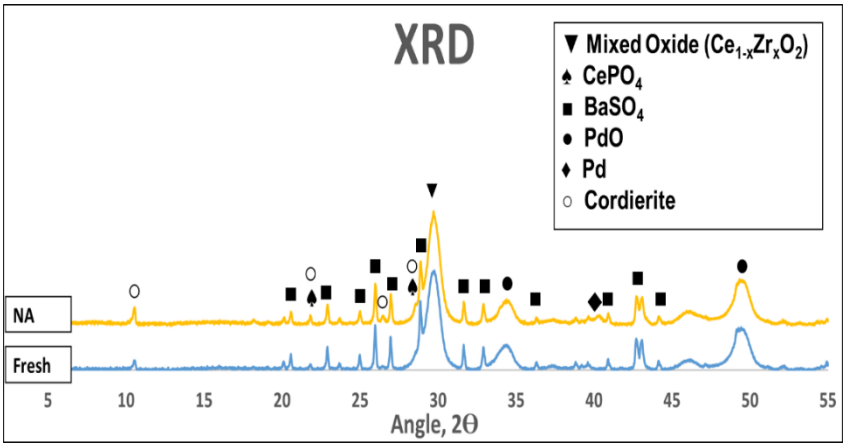

Figure 4.12 X-ray Diffraction (XRD) patterns of fresh and NA-aged TWC samples.

Results obtained from EPMA analysis provide a way to map the Zn and P content and distribution in the washcoat of the TWCs. Elemental maps of Zn and P for fresh and NA-aged TWC samples are shown in Figures 4.13 (a) and (b), respectively. Figure 4.13 (a) shows no overlayer of Zn on the washcoat surface of the fresh TWC sample, whereas a trace amount is found in the NA-aged TWC sample. Moreover, a thin layer of P overlayer and slightly P penetration throughout the washcoat of the NA-aged TWC sample are shown in Figure 4.13 (b). The presence of P in the NA-aged TWC sample is due to the contamination of the engine lubricant additive from the Genset engine that is consumed during the engine operation. Furthermore, as shown in Figure 4.9 (a), a small amount of P (0.3% wt.) is also detected through ICP-OES.

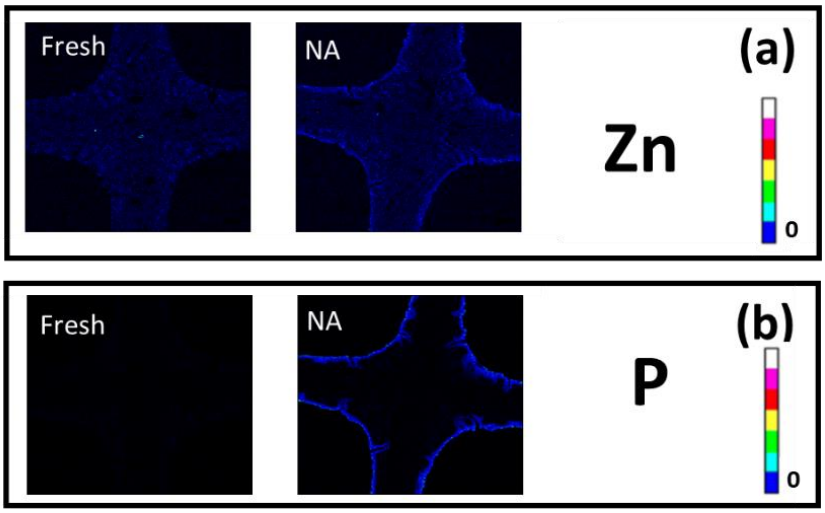

Figure 4.13 EPMA elemental maps of (a) zinc and (b) phosphorus at the inlet of fresh and NA-aged TWC samples.

4.2 Poisoning of Pd-based TWCs by Lubricant Additives

This section investigates the effects of lubricant additives such as IL, ZDDP1, ZDDP2, IL+ZDDP1, and IL+ZDDP2 on the performance of Pd-based TWCs. Section 4.2.1 presents the results obtained from BFR experiments and surface characterization studies for IL-, ZDDP1-, and ZDDP2-aged TWC samples. Section 4.2.2 compares the effects of single ZDDP additive (ZDDP1 and ZDDP2) and mixed lubricant additives (IL+ZDDP1 and IL+ZDDP2) on the performance of Pd-based TWCs.

4.2.1 IL ([P8888][DEHP]) vs. Primary ZDDP vs. Secondary ZDDP

4.2.1.1 Performance Evaluations on Bench-Flow Reactor (BFR)

As explained in detail in Section 4.1.1.1, the O_2 sweep experiment is performed to determine the concentration of O_2 at the stoichiometric condition based on the drastic increase in NO concentration. Figure 4.14 shows the effect of O_2 concentration on the concentration of NO for the thermally-aged TWC sample (NA), and the TWC samples that have been exposed to lubricant additives (IL, ZDDP1, and ZDDP2) at an inlet gas temperature of 500°C. Based on the onset of increasing NO concentration, an O_2 concentration of 0.73% at a stoichiometric condition is obtained for all TWC samples.

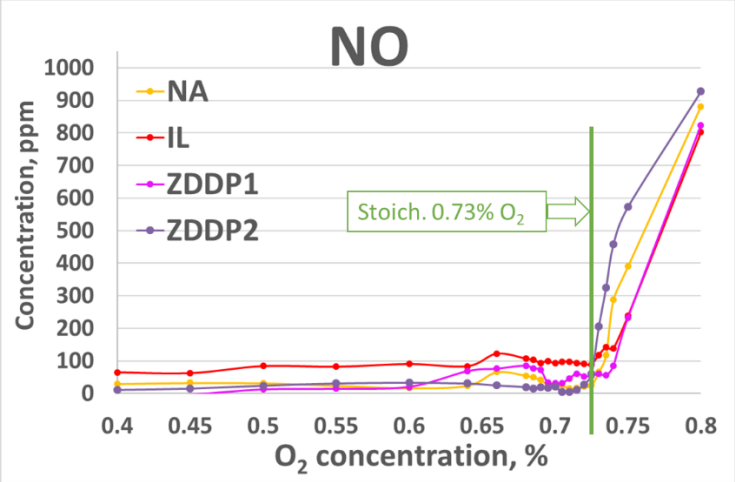

Figure 4.14 Effect of O_2 concentration on the concentration of NO for NA-, IL-, ZDDP1-, and ZDDP2-aged TWC samples with O2 concentration varying between 0.4 and 0.8%.

Using an O_2 concentration of 0.73%, a temperature sweep is performed from which T50 and T90 are obtained for all samples with the furnace temperatures varying from 100°C to 600°C. Figures 4.15 (a) to (d) show light-off curves for NO, CO, C_3H_6, and C_3H_8 for NA-, IL-, ZDDP1-, and ZDDP2-aged TWC samples, respectively. Additionally, the formation of NH_3 and N_2O for all TWC samples is shown in Figures 4.15 (e) and (f), respectively. Interestingly, in the temperature range between 150°C and 280°C, IL- and ZDDP2-aged TWC samples produce more NH_3 (Figure 4.15 (e)) and increase NO reactivity (Figure 4.15 (a)) than NA- and ZDDP1-aged TWC samples. As seen in Figure 4.15 (a), the NO light-off curves of the TWC samples exposed to lubricant additives are similar to that of the NA-aged TWC sample. The NO conversion decreases at temperatures between 250°C and 300°C, during which the conversion of CO and

C_3H_6 reaches 100% (Figures 4.15 (b) and (c)). As discussed in detail in Section 4.1 for fresh and NA-aged TWC samples, in this temperature range, the oxidation of NO reductants such as H_2, CO, or C_3H_6 is more reactive than the NO reduction reaction, resulting in a decrease in the NO conversion and the formation of NH_3. The reduction in NO conversion in the temperature range between 250°C and 300°C is coincident with an increase in N_2O formation (Figure 4.15 (f)). In addition, the NA-aged TWC sample produces more N_2O than IL-, ZDDP1-, and ZDDP2-aged TWC samples at temperatures between 230°C and 280°C. As shown in Figures 4.15 (b), (c), and (d), for TWC samples exposed to lubricant additives (IL, ZDDP1, and ZDDP2), the conversion of CO, C_3H_6, and C_3H_8 occurs at higher temperatures as compared to NA-aged (thermal aging only) TWC sample, indicating a higher T50 and T90. The impact of lubricant additives (poisoning) on the performance of TWC is clearly seen in Figures 4.15 (b), (c), and (d). In particular, the IL lubricant additive has the greatest impact on TWC performance of CO and C_3H_6 conversions compared to the ZDDP1 and ZDDP2 lubricant additives. In addition, based on the conversion of CO, C_3H_6, and C_3H_8, the ZDDP1-aged TWC sample has less impact on the performance of TWC than the ZDDP2-aged TWC sample. This is possibly due to lower P, Zn, and S content of ZDDP1 lubricant additive than that of ZDDP2 lubricant additive.

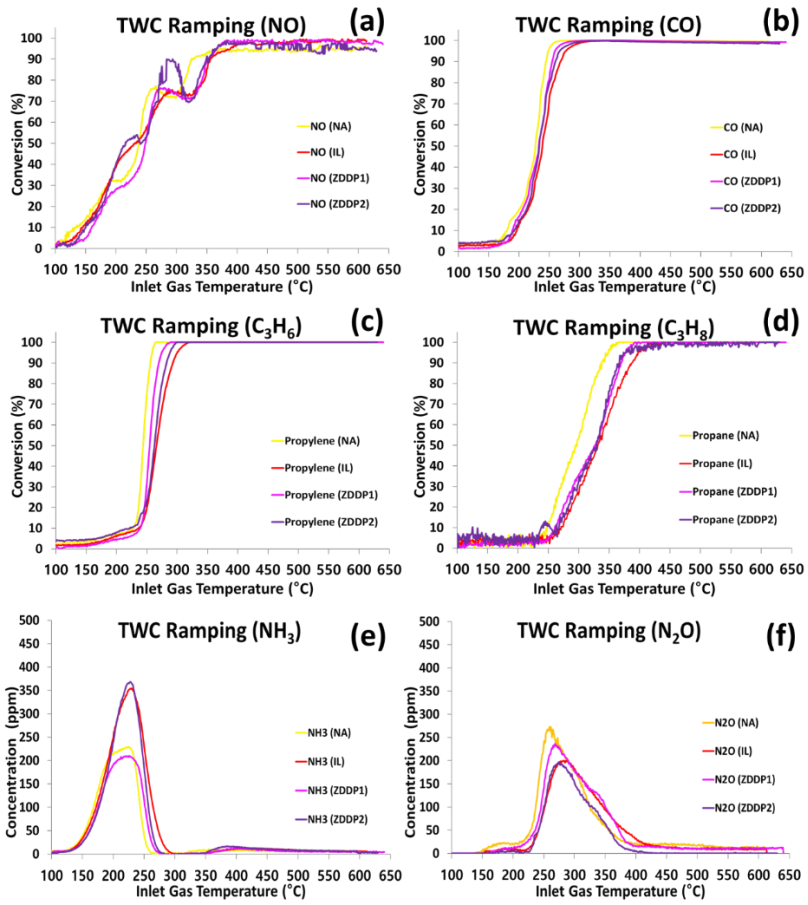

Figure 4.15 Effect of inlet gas temperature on the conversion of (a) NO, (b) CO, (c) C_3H_6, and (d) C_3H_8 and formation of (e) NH_3 and (f) N_2O for NA-, IL-, ZDDP1-, and ZDDP2-aged TWC samples at stoichiometric condition of 0.73% O_2.

From the light-off curves for NO, CO, C_3H_6, and C_3H_8, the temperatures at 50% (T50) and 90% (T90) conversion of each gas species for NA-, IL-, ZDDP1-, and ZDDP2-aged TWC samples are obtained and plotted in Figures 4.16 (a) and

(b). In addition, the difference in T50 and T90 between NA-aged TWC sample and lubricant additives-aged TWC samples is given in Table 4.2. T50 for CO, C_3H_6, and C_3H_8 of IL-, ZDDP1-, and ZDDP2-aged TWC samples is higher than that of the NA-aged TWC sample, indicating lubricant additives have an additional impact on the performance of the TWC in addition to thermal aging. Similarly, all lubricant additive-aged TWC samples have higher T90 than NA-aged TWC samples for NO, CO, C_3H_6, and C_3H_8. As seen in Figure 4.16, the IL- and ZDDP2-aged TWC samples show a similar increase in T50 and T90 for CO, C_3H_6, and C_3H_8 compared to that of NA-aged TWC sample. Surprisingly, the T50 and T90 for CO, C_3H_6, and C_3H_8 of the ZDDP1-aged TWC sample are lower than those of the ZDDP2-aged TWC sample even though Zn, P, and S are present in both lubricant additives. It is possibly due to lower concentration of Zn, P, and S in ZDDP1 than ZDDP2 lubricant additive, as will be confirmed in the results of ICP-OES and EPMA in Section 4.2.1.2. In previous studies [131,134,137], the decrease in THC and CO conversions has also been observed due to the presence of P in the conventional ZDDP.

Surprisingly, T50 for NO of the ZDDP2-aged TWC sample is 20°C lower than that of NA-aged TWC sample. As mentioned previously, the NO light-off curves exhibit no definite trend since the NO conversion is very sensitive to the reactivity of the reductants such as H_2, CO, and C_3H_6, especially in the temperature range between 150°C and 300°C. (see Figure 4.15 (a)). Therefore, it is difficult to assess the effects of lubricant additives on the performance of TWC based on the light-off behavior of NO conversion. On the other hand, the light-off behavior of CO, C_3H_6, and C_3H_8 can be used to characterize the performance degradation of the TWC either due to thermal aging as well as poisoning from lubricant additives.

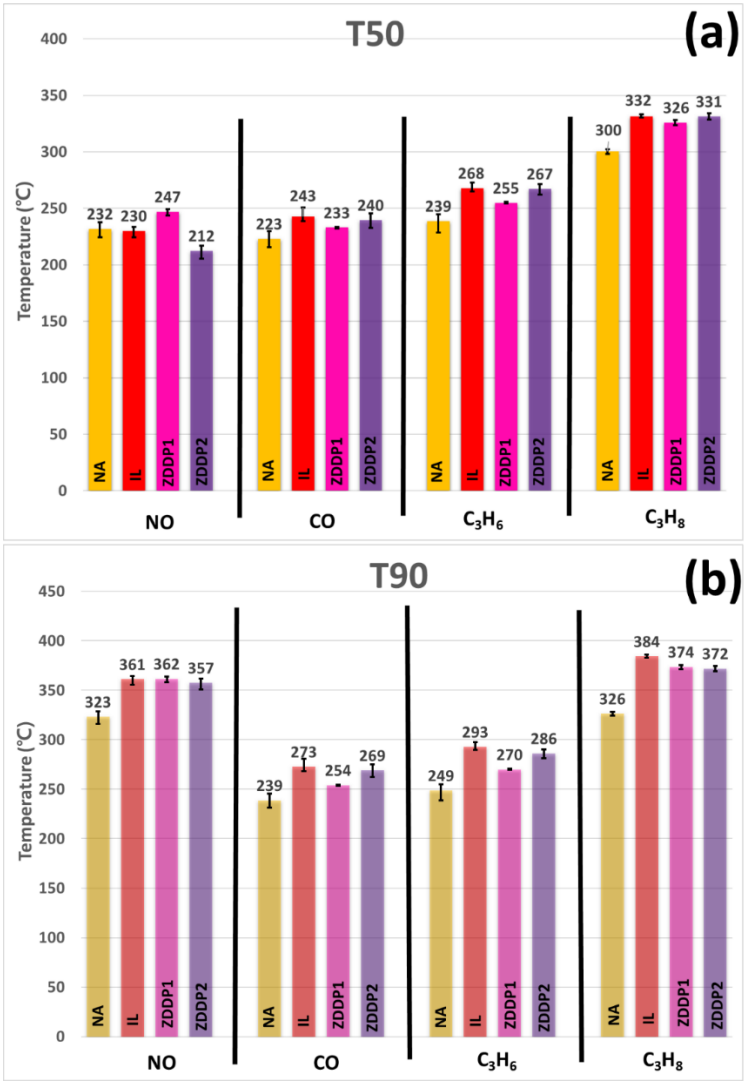

Figure 4.16 (a) T50 and (b) T90 of NO, CO, C_3H_6, and C_3H_8 for NA-, IL-, ZDDP1-, and ZDDP2-aged TWC samples.

Table 4.2 Temperature difference in T50 and T90 between NA- and IL-, ZDDP1-, and ZDDP2-aged TWC samples for NO, CO, C_3H_6, and C_3H_8.

Gas species	Sample	Temperature difference compared to NA	
		T50 (°C)	T90 (°C)
NO	IL	-2	+38
	ZDDP1	+15	+39
	ZDDP2	-20	+34
CO	IL	+20	+34
	ZDDP1	+10	+15
	ZDDP2	+17	+30
C_3H_6	IL	+29	+44
	ZDDP1	+16	+21
	ZDDP2	+28	+37
C_3H_8	IL	+32	+58
	ZDDP1	+26	+46
	ZDDP2	+31	+48

Figure 4.17 shows the OSC for thermally-aged TWC sample (NA) and TWC samples exposed to lubricant additives (IL, ZDDP1, and ZDDP2) with inlet gas temperature varying between 300°C and 550°C in 50°C increment. As seen in Figure 4.17, the degradation in the OSC performance is more severe for IL- and ZDDP2-aged TWC samples, whereas the ZDDP1-aged TWC sample is the least affected when compared to the NA-aged TWC sample. As discussed in

Section 4.1.1, the degradation of the OSC performance for the NA-aged TWC sample is mainly due to the agglomeration of CeO_2 at high temperatures. On the other hand, the most degraded IL- and ZDDP2-aged TWC samples are subjected to poisoning from lubricant additives as well as thermal aging. Furthermore, the degradation in the OSC performance of the IL-aged TWC sample is less severe than that of the ZDDP2-aged TWC at temperatures above 300°C. One possible explanation is that in addition to P, ZDDP2 lubricant additive also has other OSC degradation components such as Zn and S, whereas IL only contains P. Surprisingly, the degradation of the OSC of ZDDP1-aged TWC sample is similar to that of NA-aged TWC sample, even though P, S, and Zn are present in ZDDP1 lubricant additive. In a recent study, Xie et al. [134] investigated the impact of an oil-miscible IL ([P66614][DEHP]) and an industry-standard ZDDP on OSC of TWC. They found the impact of the ZDDP lubricant additive, they did not specify the type of their ZDDP, on OSC is less severe--approximately 25% reduction in the OSC compared to the NA-aged TWC sample at temperatures above 450°C--than the result of ZDDP2 obtained in the present study. On the other hand, the IL ([P66614][DEHP]) lubricant additive has less impact on the OSC of TWC in all temperature ranges, which is in contrast to the IL ([P8888][DEHP]) used in the present study. The discrepancy between the results obtained by Xie et al. and the results obtained in the present study is possibly due to different aging temperature and aging time of the accelerated engine aging protocol.

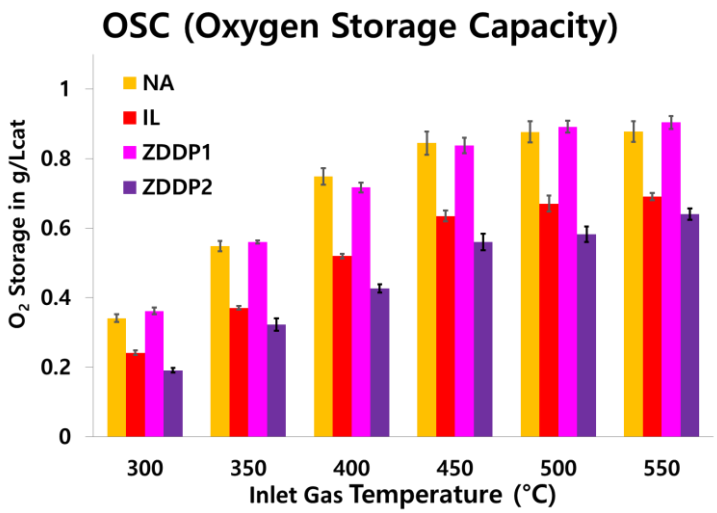

Figure 4.17 Oxygen storage capacity (OSC) for NA-, IL-, ZDDP1-, and ZDDP2-aged TWC samples at inlet gas temperatures between 300°C and 550°C in a 50°C increment.

The impact of lubricant additives on the WGS reaction is investigated. Figure 4.18 shows the concentration of CO_2 produced from WGS reaction for NA-, IL-, ZDDP1-, and ZDDP2-aged TWC samples at temperatures between 200°C and 550°C in 50°C increment. The maximum WGS reaction for all samples occurs at 500°C. As expected, significant WGS reactivity losses for the IL- and ZDDP2-aged samples above 300°C are mainly due to poisoning from lubricant additives. This is another indication that both the IL and ZDDP2 additives have the same impact on the TWCs, and that the P-content of the additives is the key contributing factor to the degradation of the TWCs. Interestingly, ZDDP1 lubricant additive has less impact on the OSC performance than either IL or ZDDP2 lubricant additives, as shown in Figure 4.17. The

degradation of the WGS reaction for the IL, ZDDP1, and ZDDP2 additives can be attributed to the formation of either Zn or P compounds on the washcoat surface [165-167]. As mentioned before, it is well-known that the WGS reaction mainly occurs over the noble metals, and with those sites completely or partially covered with either Zn or P compounds, the reactivity of those sites is reduced considerably. Also, it has been reported the presence of CeO_2 in the Pd/Rh TWC catalyst is known to enhance the WGS reaction [12,159,161–163]. Therefore, it can be inferred that the WGS reaction of the ZDDP1-aged TWC sample with less reduction in OSC performance (see Figure 4.17) is higher than that of IL- and ZDDP2-aged TWC samples.

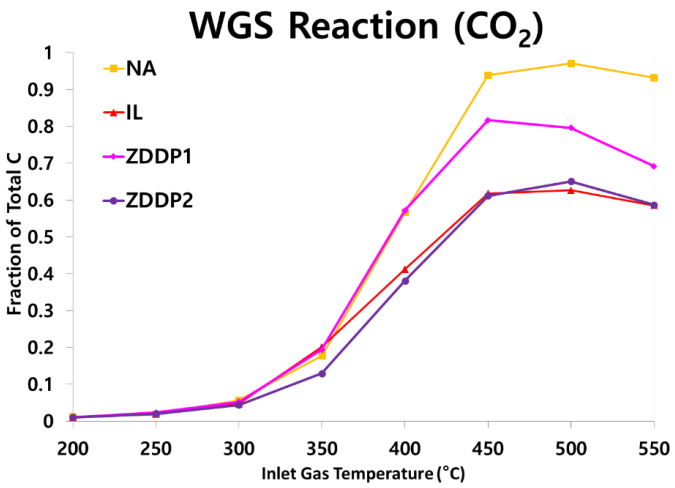

Figure 4.18 Formation of CO_2 in water gas shift (WGS) reaction for NA-, IL-, ZDDP1-, and ZDDP2-aged TWC samples at inlet gas temperatures between 200°C and 550°C.

4.2.1.2 Surface Characterization Analysis Results

ICP-OES analysis is used to determine the weight percentage of P and Zn in the washcoat of the TWC samples. The NA-aged TWC sample is used as a baseline to which the TWC samples that have been exposed to lubricant additives (IL, ZDDP1, and ZDDP2) are compared. Figures 4.19 (a) and (b) show the ICP-OES weight percent result for P and Zn for NA- IL-, ZDDP1-, and ZDDP2-aged TWC samples, respectively. As seen in Figure 4.19 (a), all TWC samples exposed to lubricant additives contain large amounts of P, with the smallest amount being 0.30 wt.% in the NA-aged TWC sample, and similar amounts are observed in the IL- and ZDDP2-aged samples, 1.31 and 1.38 wt.%, respectively. On the other hand, the ZDDP1-aged TWC sample shows the lowest exposure to P compared to the IL- and ZDDP2-aged TWC samples, which is somewhat surprising since the dose of P remained constant throughout the experiment. According to a previous study by Wang et al. [168], lubricant oil containing secondary ZDDP (ZDDP2) exhibited higher phosphorus retention (~96%) than lubricant oil containing mixed primary (ZDDP1) and secondary ZDDPs (~88%) because of different phosphorus volatility. Thus, it can be inferred from Wang's study that during the accelerated engine aging, more phosphorus is retained on the TWC due to the higher phosphorus volatility of ZDDP1 lubricant additive than the lower phosphorus volatility ZDDP2 lubricant. Although there are uncertainties such as the different locations of the sample taken for ICP analysis, it is clearly seen that all samples exposed to lubricant additives contain large amounts of P. The P detected in the NA-aged TWC sample originated from the lubricant of the engine, as discussed previously in Section 4.1.1.

On the other hand, as shown in Figure 4.19 (b), the highest amount of Zn is detected in the ZDDP1-aged TWC sample, whereas a smaller amount is observed in the IL-aged TWC sample, as expected since the IL does not contain

Zn. It should be noted that these Zn levels are near the detection limit of the instrument and should not be an indication of big differences across the samples, but instead, they clearly indicate a low level of Zn is captured in these samples.

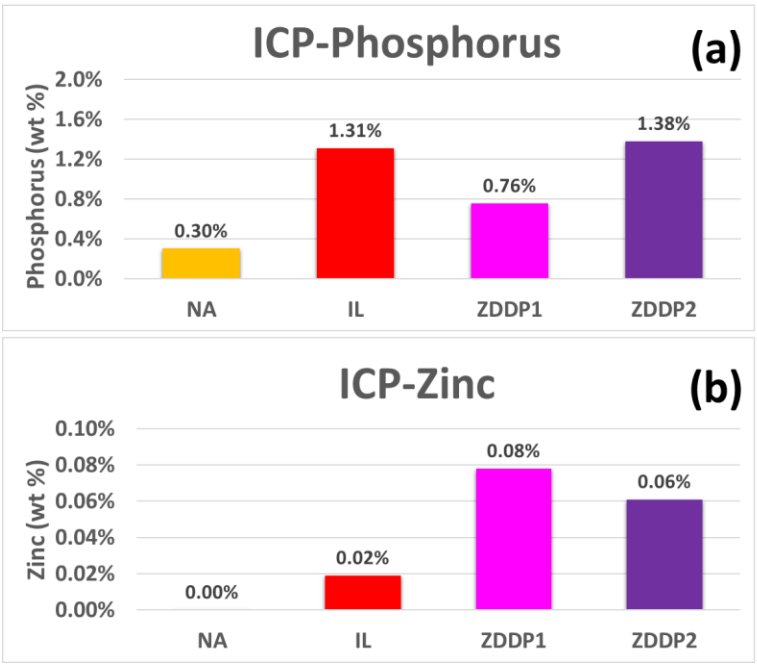

Figure 4.19 ICP-OES results of (a) P and (b) Zn in weight percent for NA-, IL-, ZDDP1-, and ZDDP2-aged TWC samples.

To determine the impact of thermal aging and lubricant additive poisoning on the surface area of TWC, N_2 physisorption measurement is performed only on the washcoat of NA-, IL-, ZDDP1-, and ZDDP2-aged TWC samples. The results

of the BET surface area of each sample are given in Figure 4.20. Results indicate that the NA-aged TWC sample has the largest BET surface area of 83.44 m^2/g, whereas the TWC sample aged with IL has the smallest surface area of 74.81 m^2/g. In addition, the reduction of surface area for IL-, ZDDP1-, and ZDDP2-aged TWC samples compared to the NA-aged TWC sample is 10, 7, and 3%, respectively. It should be noted that N_2 physisorption for all samples is performed with as much cordierite removed as possible, the discrepancy in the BET surface area of IL-aged TWC sample and ZDDP1- and ZDDP2-aged TWC samples is possibly due more cordierite in the IL-aged TWC samples. However, it is clearly observed that further reduction in the surface area of the TWC samples that have been exposed to lubricant additives (IL, ZDDP1, and ZDDP2) are caused by both lubricant additive poisoning and thermal aging. Hussain [169] agreed with these findings based on their BET surface area results.

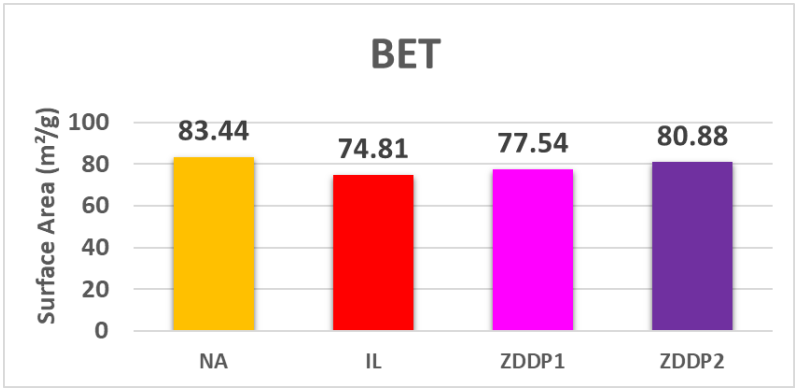

Figure 4.20 BET surface area measurements of NA-, IL-, ZDDP1-, and ZDDP2-aged TWC samples.

Figures 4.21 (a) and (b) present the BJH pore volumes and pore sizes of NA-, IL-, ZDDP1-, and ZDDP2-aged TWC samples, respectively. As shown in Figure 4.21 (a), the BJH pore volumes of IL- and ZDDP2-aged TWC samples are similar, whereas the ZDDP1-aged TWC sample has less effect on pore volume compared to the NA-aged TWC sample. On the other hand, the BJH pore size of all TWC samples is the least affected, as can be seen in Figure 4.21 (b). This suggests there is not blocking or occluding of the pores by the compounds formed from the components of the lubricant additives such as P, Zn, S, etc.

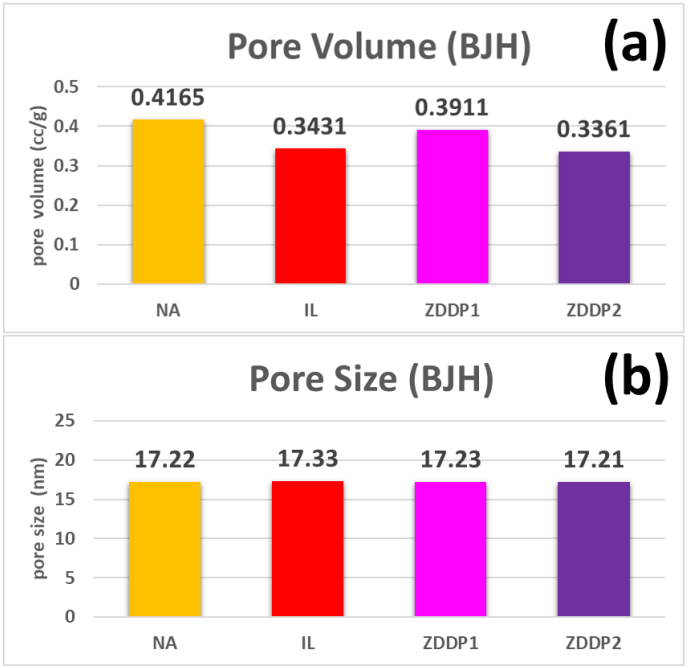

Figure 4.21 (a) Pore volume and (b) pore size (BJH method) measurements of NA-, IL-, ZDDP1-, and ZDDP2-aged TWC samples.

XRD spectra are used to identify compounds formed within NA-, IL-, ZDDP1-, and ZDDP2-aged TWC samples (washcoat only), and the XRD patterns of those samples are shown in Figure 4.22. It should be noted that since the XRD patterns of cerium phosphate ($CePO_4$) peaks and cordierite peaks mostly overlap, intensity variations in $CePO_4$ peaks are apparent in lubricant additive aging samples. The intensity of $CePO_4$ peaks for ZDDP2- and IL-aged TWC samples is stronger than that of the ZDDP1-aged TWC sample. The formation of $CePO_4$ in TWC due to lubricant additives (conventional ZDDP and IL) was confirmed by Xie et al. [134]. Even though Zn is a major component of ZDDP1 and ZDDP2 lubricant additives, no peaks associated with Zn, such as $Zn_2P_2O_4$, are observed in the ZDDP1- or ZDDP2-aged TWC samples XRD patterns. The peak of Pd at 2θ = 39.6° for the TWC samples exposed to lubricant additives (IL, ZDDP1, and ZDDP2) is larger and broader than the NA-aged TWC sample, indicating larger particle sizes and the lower dispersion.

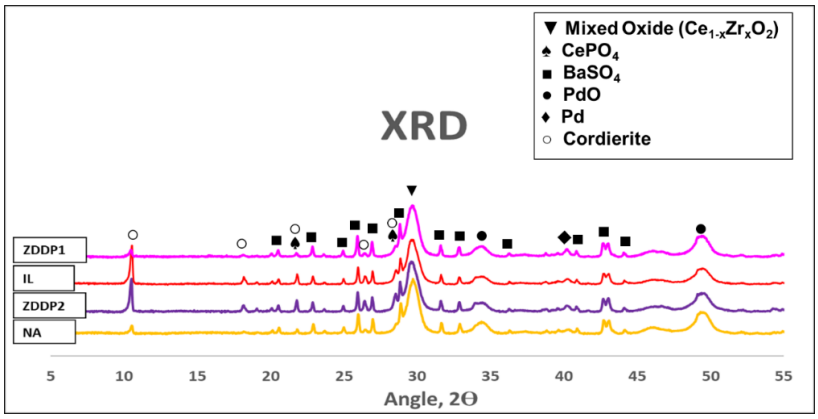

Figure 4.22 X-ray Diffraction (XRD) patterns for NA-, IL-, ZDDP1-, and ZDDP2-aged TWC samples.

EPMA analysis is performed to detect the presence of P and Zn in the washcoat of each TWC sample. EPMA micrographs of Zn and P for NA-, IL-, ZDDP1-, and ZDDP2-aged TWC samples are shown in Figures 4.23 (a) and (b), respectively. A thin layer of highly concentrated Zn is observed on the washcoat surface of the ZDDP1- and ZDDP2-aged TWC samples (bright green) with lower concentrations (blue) penetrating deeper into the washcoat, whereas only a low concentration of Zn is seen in the washcoat of the IL-aged TWC sample. The result is not surprising because Zn is present only in ZDDP1 and ZDDP2, but not in IL. Furthermore, as mentioned in Section 4.1.2, only a trace amount of Zn is detected in the NA-aged TWC sample, mainly through the consumption of the lubricant oil during the operation of the engine.

On the other hand, the thin layer of highly concentrated Zn on the ZDDP2-aged TWC sample is more highly visible and contiguous than that on the ZDDP1-aged TWC sample, as confirmed by the ICP results (see in Figure 4.19 (a)). As mentioned before, it is surprising that even the dose of P is kept constant during the accelerated engine poisoning engine, the amount of P detected on IL-, ZDDP1- and ZDDP2-aged TWC samples is different. As mentioned before, it is surprising that even the dose of P is kept constant during the accelerated engine poisoning engine, the amount of P detected on IL-, ZDDP1- and ZDDP2-aged TWC samples is different. This is possibly due to different phosphorus volatility of ZDDP1 and ZDDP2 lubricant additives [168]. But one thing certain is that all TWC samples exposed to lubricant additives are contaminated with large amount of P as compared to the NA-aged TWC sample. Five notable features are observed from the EPMA micrographs of P shown in Figure 4.23 (b). Firstly, the presence of P occurs mainly on the washcoat surface with evidence of P penetration inside the washcoat. Secondly, the P overlayer for the NA-aged TWC sample is much thinner than that for IL-, ZDDP1-, and ZDDP2-aged TWC

samples. Thirdly, the P overlayer for the ZDDP1-aged TWC sample appears to be thinner than that for the ZDDP2-aged TWC sample, which observed the same result in the ICP-OES analysis (see in Figure 4.19 (a)). Fourthly, a high concentration of P is observed on the washcoat surface for ZDDP1- and ZDDP2-aged TWC samples (red) as compared to the IL-aged TWC sample (primary green). Finally, the concentration of P in the overlayer of the IL-, ZDDP1-, and ZDDP2-aged TWC samples is much higher than that of the NA-aged TWC sample. The high levels of P are not surprising here but are a clear indication that the interactions are similar for each of the additives. The low concentration of P in the NA-aged TWC sample is simply due to lube oil consumption through the natural operation of the engine.

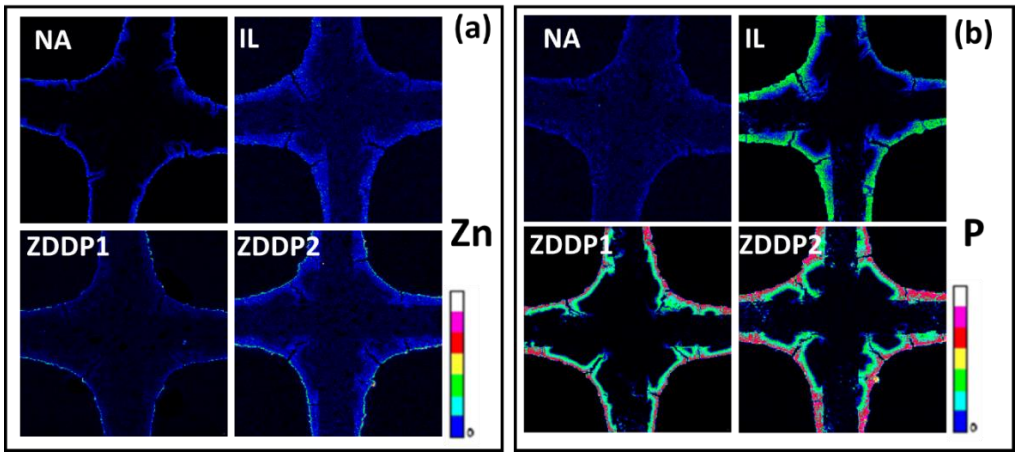

Figure 4.23 EPMA elemental maps of (a) Zn and (b) P at the inlet of NA-, IL-, ZDDP1-, and ZDDP2-aged TWC samples.

4.2.2 IL+Primary ZDDP (IL+ZDDP1) vs. IL+Secondary ZDDP (IL+ZDDP2)

4.2.2.1 Performance Evaluations on Bench-flow Reactor

As described in detail in Sections 4.1.1 and 4.2.1.1, the O_2 sweep experiment is carried out to determine the concentration of O_2 at the stoichiometric condition based on an abrupt increase in NO concentration between stoichiometric and fuel-lean conditions. Figure 4.24 shows the effect of O_2 concentration on the concentration of NO for NA-, ZDDP1-, ZDDP2-, IL+ZDDP1-, and IL+ZDDP2-aged TWC samples at the inlet gas temperature of 500°C. In Figure 4.24 and subsequent figures, the results for NA-, ZDDP1-, and ZDDP2-aged TWC samples are also shown for comparison purposes. Coincidentally, the NO concentration for all TWC samples begins to increase rapidly at an O_2 concentration of 0.73%, which is not much different from a theoretical value of 0.72% at stoichiometric condition (see Section 3.3.3.1).

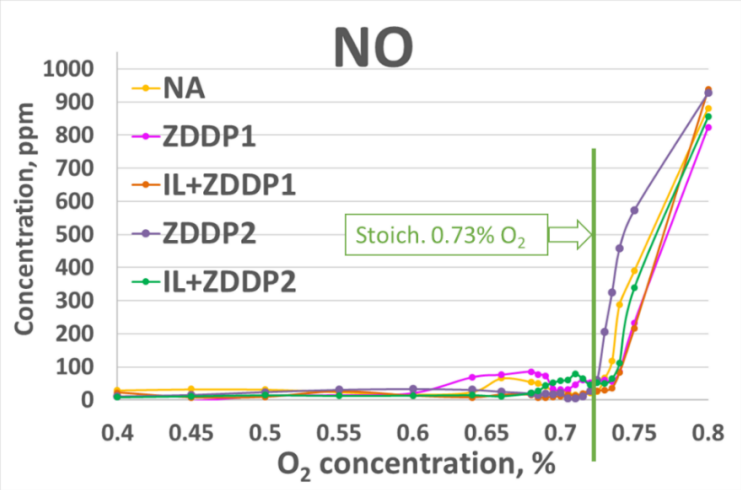

Figure 4.24 Effect of O_2 concentration on the concentration of NO for NA-, ZDDP1-, ZDDP2-, IL+ZDDP1-, and IL+ZDDP2-aged TWC samples with O_2 concentration varying between 0.4 and 0.8%.

The temperature sweep experiment is conducted to determine T50 and T90 of all engine-aged TWC samples at inlet gas temperatures between 100°C and 640°C using the O_2 concentration at the experimentally-determined stoichiometric condition of 0.73% O_2 obtained previously. The light-off curves of NO, CO, C_3H_6, and C_3H_8 for NA-, ZDDP1-, ZDDP2-, IL+ZDDP1-, and IL+ZDDP2-aged TWC samples are shown in Figures 4.25 (a) to (d), respectively. In addition, the formation of NH_3 and N_2O for all engine-aged TWC samples is plotted in Figures 4.25 (e) and (f), respectively. As shown in Figures 4.25 (b), (c), and (d), at a given conversion, the conversion of CO, C_3H_6, and C_3H_8 for all TWC samples exposed to lubricant additives (ZDDP1-, ZDDP2-, IL+ZDDP1-, and IL+ZDDP2) always occurs at a slightly higher temperature as compared to the NA-aged TWC sample, indicating a higher T50 and T90 (see Figures 4.26 (a)

and (b)). Such results unequivocally indicate the additional impact of lubricant additives (poisoning) on the performance of TWC in addition to thermal aging.

Figure 4.25 (e) shows that the ZDDP2- and IL+ZDDP2-aged TWC samples produce more NH_3 compared to NA-, ZDDP1-, and IL+ZDDP1-aged TWC samples at inlet gas temperatures between 150°C and 280°C, during which the conversion of NO for ZDDP2- and IL+ZDDP2-aged TWC samples is better than for NA-, ZDDP1-, and IL+ZDDP1-aged TWC samples (Figure 4.25 (a)). This results in a higher T50 for NO for NA-, ZDDP1-, and IL+ZDDP1-aged TWC samples, as will be seen later in Figure 4.26 (a). As mentioned previously in Sections 4.1.1 and 4.2.1.1, because there is a lack of NO reductants such as H_2, CO, and C_3H_6 in the temperature range between 270°C and 320°C, the conversion of NO decreases, resulting in an increase in T90 for NO for all engine-aged TWC samples. As mentioned previously in Sections 4.1.1 and 4.2.1, due to the complexity of the NO light-off curves, it is difficult to characterize the effects of lubricant additives on TWC performance using T50 and T90 of NO. Based on the light-off curves of CO and C_3H_6 (Figures 4.25 (b) and (c)), ZDDP2- and IL+ZDDP2-aged TWC samples appear to experience more performance degradation of TWC than ZDDP1- and IL+ZDDP1-aged TWC samples. As mentioned before, this can be attributed to higher P, Zn, and S contents in ZDDP2 than that ZDDP1.

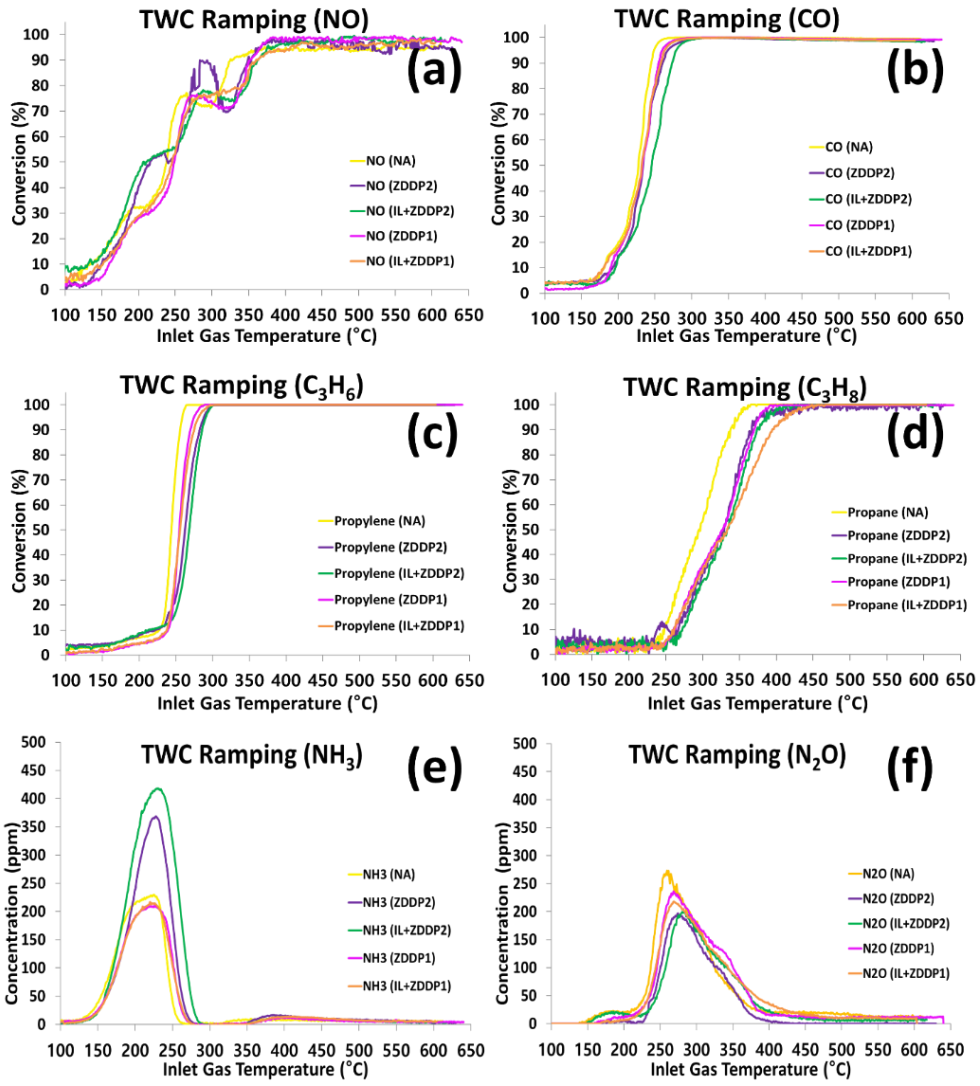

Figure 4.25 Effect of inlet gas temperature on the conversion (a) NO, (b) CO, (c) C_3H_6, (d) C_3H_8, and the formation of (e) NH_3 and (f) N_2O for NA-, ZDDP1-, ZDDP2-, IL+ZDDP1-, and IL+ZDDP2-aged TWC samples at the stoichiometric condition of 0.73% O_2 at inlet gas temperatures between 100°C and 640°C.

Figures 4.26 (a) and (b) show the temperature of 50% (T50) and 90% (T90) conversion of NO, CO, C_3H_6, and C_3H_8 for NA-, ZDDP1-, ZDDP2-, IL+ZDDP1-, and IL+ZDDP2- samples obtained from the light-off curves given in Figure 4.25. Also, Table 4.3 shows the difference in T50 and T90 between NA-aged TWC sample and lubricant additives-aged (poisoning) TWC samples. As mentioned before, the T50 of NO for ZDDP2- and IL+ZDDP2-aged TWC samples is lower than NA-, ZDDP1-, and IL+ZDDP1-aged TWC samples, which can be attributed to the higher formation of NH_3 at temperatures between 150°C and 280°C (see Figures 4.25 (a) and (e)). Except for the T50 of NO, all TWC samples exposed to lubricant additives have higher T50 and T90 for CO, C_3H_6, and C_3H_8 than the NA-aged TWC sample, indicating further degradation of the TWC performance due to lubricant additives poisoning in addition to thermal aging. Except for the T50 and T90 of C_3H_8, since ZDDP2 lubricant additive contains more P, S, and Zn by weight than ZDDP1, it is not surprising that T50 and T90 of CO and C_3H_6 for ZDDP2- and IL+ZDDP2-aged TWC samples are higher than for ZDDP1- and IL+ZDDP1-aged TWC samples. Thus, in general, the higher the amount of P, Zn, and S in the lubricant additive, the larger the impact on the TWC performance.

One of the major objectives of the present study is to compare the impact on the performance of the TWC by either a single ZDDP lubricant additive or a mixed lubricant additive containing both ZDDP and IL (IL+ZDDP). One way to determine the impact is to compare the T50 and T90 obtained from a single ZDDP lubricant additive and a mixed additive of IL and ZDDP (i.e., ZDDP1 vs. IL+ZDDP1 and ZDDP2 vs. IL+ZDDP2). As shown in Table 4.2, the T50 for the ZDDP1-aged TWC sample increases by 15, 10, 16, and 26°C for NO, CO, C_3H_6, and C_3H_8, respectively as compared with the NA-aged TWC sample. Moreover, the T50 for IL+ZDDP1-aged TWC sample increases by about a similar amount to

the ZDDP1-aged TWC sample. For the ZDDP2-aged TWC sample, the T50 for CO, C_3H_6, and C_3H_8 increases by 17, 28, and 31°C, respectively, but decreases by 20°C for NO compared with the NA-aged TWC sample. As in the case of ZDDP1 and IL+ZDDP1, the T50 for NO, CO, C_3H_6, and C_3H_8 for the IL+ZDDP2-aged TWC sample is similar to that for the ZDDP2-aged TWC sample. A similar trend is observed for the T90 for these samples. Based on these results, it is apparent that the impact of the mixed lubricant additives, either IL+ZDDP1 or IL+ZDDP2, on the TWC performance is similar to that of the ZDDP constituent rather than the IL. As will be shown later in Section 4.2.2.2, the results obtained from surface characterization studies such as ICP-OES, BET, XRD, and EPMA can be used to explain the effects of the lubricant additives on the T50 and T90 of NO, CO, C_3H_6, and C_3H_8 of accelerated engine-aged TWCs.

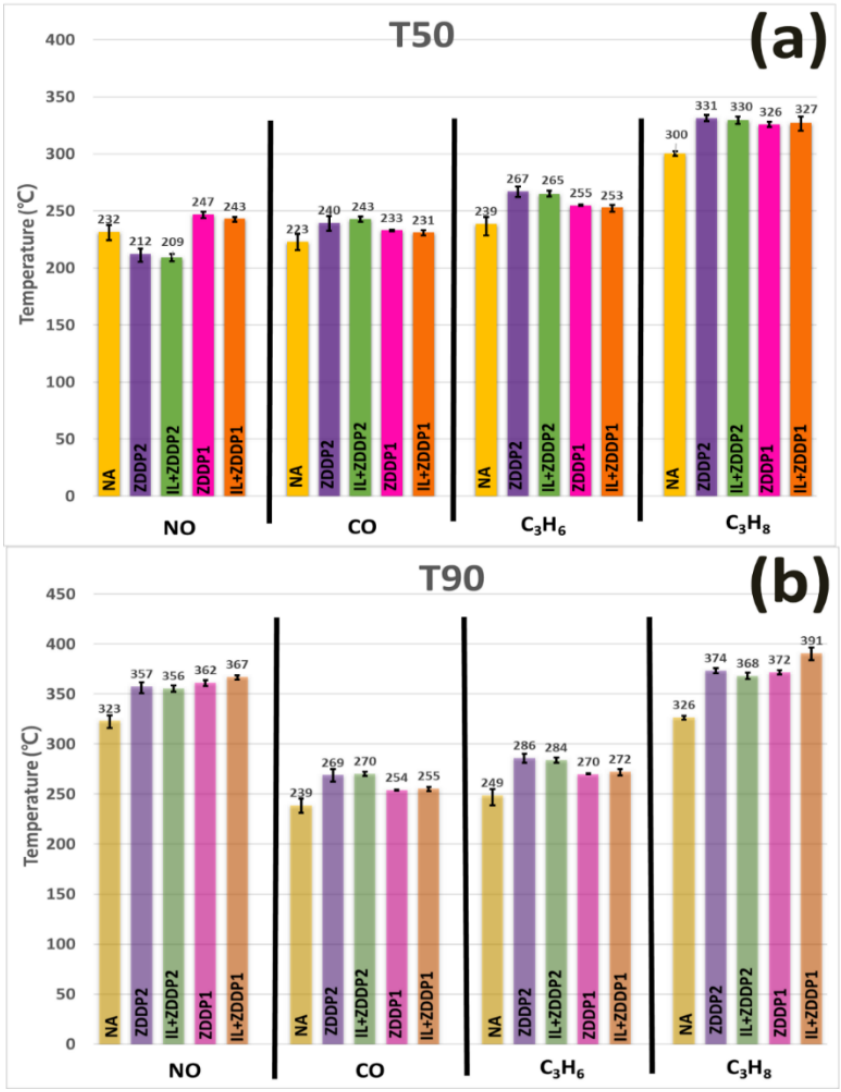

Figure 4.26 (a) T50 and (b) T90 of NO, CO, C_3H_6, and C_3H_8 for NA-, ZDDP1-, ZDDP2-, IL+ZDDP1-, and IL+ZDDP2-aged TWC samples.

Table 4.3 Temperature difference in T50 and T90 between NA- and ZDDP1-, ZDDP2-, IL+ZDDP1-, and IL+ZDDP2-aged TWC samples for NO, CO, C_3H_6, and C_3H_8.

Gas species	Sample	Temperature difference compared to NA	
		T50 (°C)	T90 (°C)
NO	ZDDP1	+15	+39
	IL+ZDDP1	+11	+44
	ZDDP2	-20	+34
	IL+ZDDP2	-23	+33
CO	ZDDP1	10	+15
	IL+ZDDP1	+8	+16
	ZDDP2	+17	+30
	IL+ZDDP2	+20	+31
C_3H_6	ZDDP1	+16	+21
	IL+ZDDP1	+14	+23
	ZDDP2	+28	+37
	IL+ZDDP2	+26	+35
C_3H_8	ZDDP1	+26	+46
	IL+ZDDP1	+27	+65
	ZDDP2	+31	+48
	IL+ZDDP2	+30	+42

The OSC experiment is performed to investigate the effect of lubricant additives on CeO_2, the oxygen storage material, in a temperature range between 300°C to 550°C at a 50°C increment. Figure 4.27 shows the OSC for NA-, ZDDP1-, ZDDP2-, IL+ZDDP1-, and IL+ZDDP2-aged TWC samples. The OSC performance of the ZDDP2- and IL+ZDDP2-aged TWC samples is more degraded than that of the ZDDP1- and IL+ZDDP1-aged TWC samples due to ZDDP2 lubricant additive contains more P, Zn, and S content than ZDDP1 lubricant additive. On the other hand, the OSC performance of the ZDDP1-aged TWC sample is comparable to the NA-aged TWC sample at all temperatures investigated in the present study. This result is the most surprising despite the fact that the ZDDP1-aged TWC sample was exposed to more P, Zn, and S poisoning than the NA-aged TWC sample during the accelerated engine aging. The reasons for such similarity in the OSC performance of ZDDP1 and NA-aged TWC samples can be explained from the results of surface characterization studies such as XRD, EPMA, BET, and ICP-OES given in Section 4.2.2.2. As in the case of T50 and T90, the OSC performance of the mixed lubricant additives (IL+ZDDP1 and IL+ZDDP2) is similar to that of the single ZDDP lubricant additives (ZDDP1 and ZDDP2).

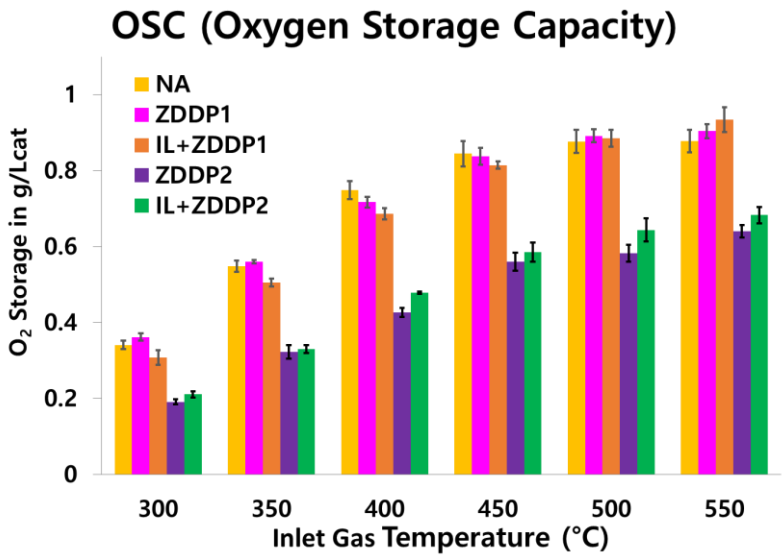

Figure 4.27 Oxygen storage capacity (OSC) for NA-, ZDDP1-, ZDDP2-, IL+ZDDP1-, and IL+ZDDP2-aged TWC samples at inlet gas temperatures between 300°C and 550°C in a 50°C increment.

The WGS reaction is performed to investigate the impact of lubricant additives on the performance of TWC at inlet gas temperatures between 200°C and 550°C at a 50°C increment. The concentration of CO_2 produced from the WGS reaction as a function of temperature for NA-, ZDDP1-, ZDDP2-, IL+ZDDP1-, and IL+ZDDP2-aged TWC samples is shown in Figure 4.28. The WGS reaction results indicate that the reduction in WGS reaction for all TWC samples exposed to lubricant additives (ZDDP1, ZDDP2, IL+ZDDP1, and IL+ZDDP2) is greater than the NA-aged TWC sample, indicating that in addition to thermal aging, P, S, and Zn poisoning from lubricant additives is also significant. As expected, the WGS reaction for the ZDDP2- and IL+ZDDP2-aged

TWC samples is significantly degraded than that for ZDDP1- and IL+ZDDP1-aged TWC samples at all temperatures investigated in the present study. Again, the main difference between ZDDP1 and ZDDP2 lubricant additives is that the ZDDP2 additive contains more P, S, and Zn. As in the case of OSC performance, the impact on the WGS reaction of the TWC of the mixed lubricant additives is similar to that of single ZDDP lubricant additives.

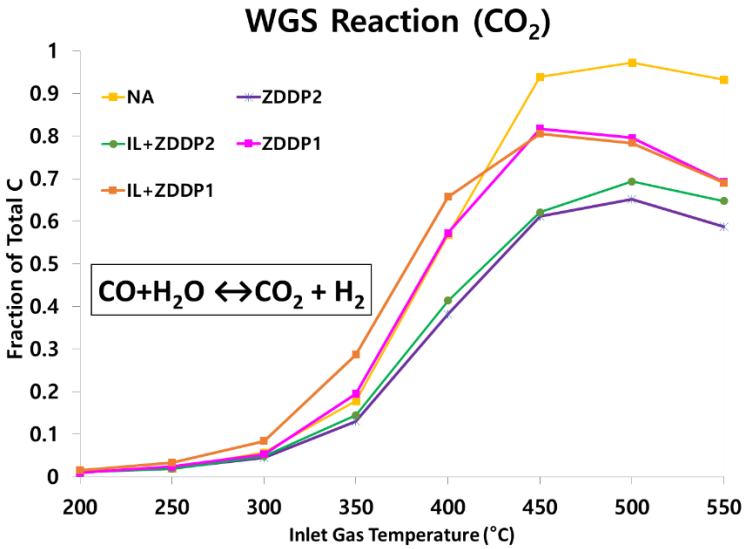

Figure 4.28 Formation of CO_2 in water gas shift (WGS) reaction for NA-, ZDDP1-, ZDDP2-, IL+ZDDP1-, and IL+ZDDP2-aged TWC samples at inlet gas temperatures between 200°C and 550°C.

4.2.2.2 Surface Characterization Analysis Results

The weight percentage of P and Zn in the washcoat of the TWC samples is determined using ICP-OES analysis and given in Figures 4.29 (a) and (b) for NA-, ZDDP1-, ZDDP2-, IL+ZDDP1-, and IL+ZDDP2-aged TWC samples. As mentioned previously in Section 4.1.2, the presence of P of 0.3% by weight detected in the NA-aged TWC sample is solely due to the P originally from the ZDDP additive in the Genset engine lubricant since no lubricant additives are added to the fuel for the accelerated thermal aging. Although the amount of lubricant additives added to the fuel is calculated based on the same amount of P exposed to the catalyst during accelerated engine aging, the amount of P detected in ZDDP2- and IL+ZDDP2-aged TWC samples is at least double the amount of P found in the ZDDP1- and IL+ZDDP1-aged TWC samples (see Figure 4.29 (a)). Interestingly the amount of P detected either in ZDDP- and IL+ZDDP-aged TWC samples, i.e., ZDDP1 vs. IL+ZDDP1 and ZDDP2 vs. IL+ZDDP2, are similar. It is apparent that the amount of P accumulated on the TWC is more affected by the type of ZDDP than IL due to the difference in the phosphorus volatility of ZDDP1 and ZDDP2 [168]. On the other hand, as seen in Figure 4.29 (b), more Zn is detected in the ZDDP1- and IL+ZDDP1-aged TWC samples than the ZDDP2- and IL+ZDDP2-aged TWC samples. As mentioned previously in Section 4.2.1.2, the variation in the amount of Zn detected in the TWC samples exposed to the lubricant additives is mainly due to the detection limit of the ICP instrument and should not be interpreted as an indication of strong differences across the samples, but instead, they clearly indicate a low level of Zn is captured in these samples.

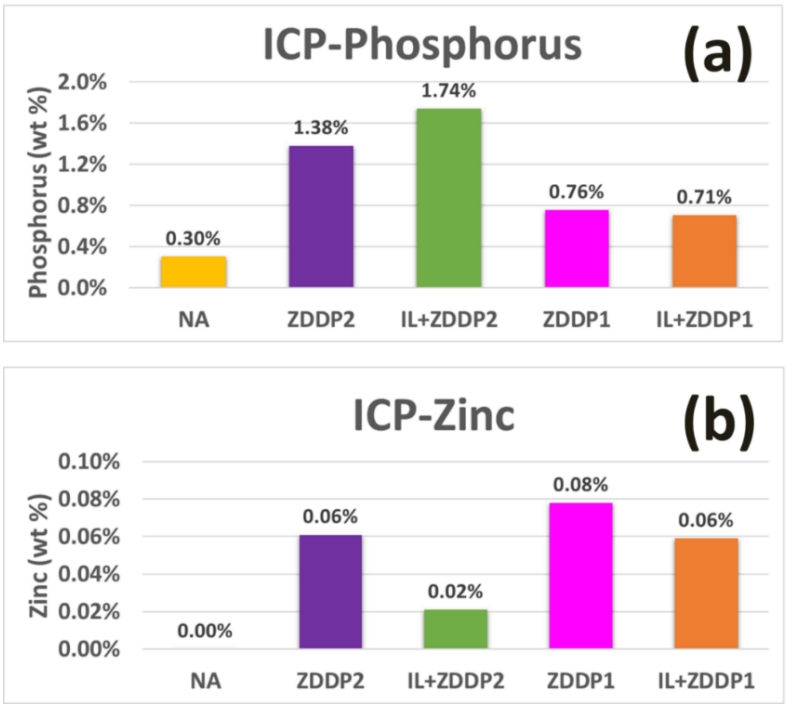

Figure 4.29 ICP-OES results of (a) P and (b) Zn in weight percent for NA-, ZDDP1-, ZDDP2-, IL+ZDDP1-, and IL+ZDDP2-aged TWC samples.

To investigate the effect of lubricant additives on TWC, the N_2 physisorption is performed on washcoat powder of all engine-aged TWC samples, from which the BET surface area, pore-volume, and pore size distribution are obtained. Figure 4.30 shows the BET surface area in m^2/g of NA-, ZDDP1-, ZDDP2-, IL+ZDDP1-, and IL+ZDDP2-aged TWC samples. As shown previously in Section 4.1.2, the BET surface area of the NA-aged TWC sample is reduced by about 16% compared with the fresh TWC sample mainly due to thermal aging. All TWC samples exposed to lubricant additives (ZDDP1, ZDDP2, IL+ZDDP1, and IL+ZDDP2) have a lower BET surface area than the NA-aged

TWC sample with the IL+ZDDP2-aged TWC sample having the smallest surface area of 71.6 m^2/g. The BET surface area of IL+ZDDP2-aged TWC sample is approximately 11.4% lower than that of the ZDDP2-aged TWC sample. This is possibly due to the presence of more cordierite in that sample, which has a much lower BET surface area than that of γ-Al_2O_3 washcoat (100~200 m^2/g). On the other hand, The BET surface area of the ZDDP1- and IL+ZDDP1-aged TWC samples is similar to (77.54 vs. 77.74 m^2/g), but still 7% lower than the NA-aged sample. Even though the loss of BET surface due to the poisoning of the lubricant additives alone is not significant varying between 3 and 11.4%, but that loss would result in a lower dispersion of the Pd particles, which in turn affects the reactivity of the reactions occurring on the Pd active sites. Thus, the performance of TWC exposed to lubricant additives would be adversely impacted.

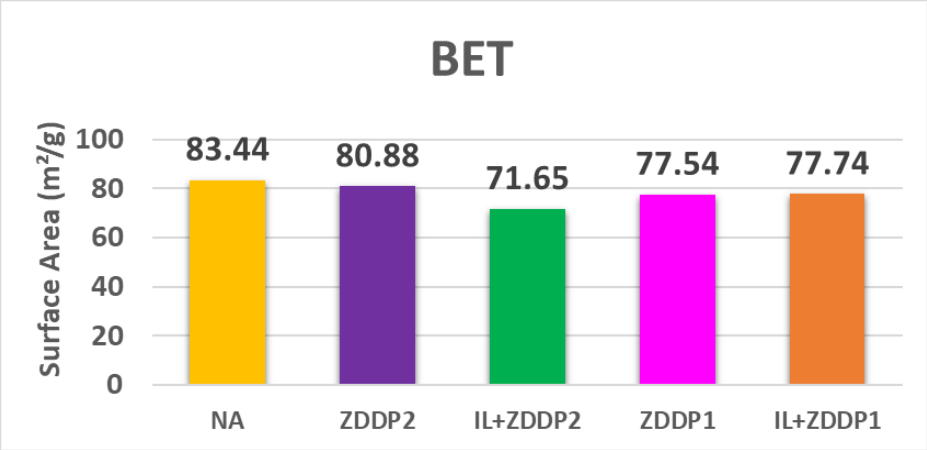

Figure 4.30 BET surface area measurements of NA-, ZDDP1-, ZDDP2-, IL+ZDDP1-, and IL+ZDDP2-aged TWC samples.

The BJH pore volumes and pore sizes of NA-, ZDDP1-, ZDDP2-, IL+ZDDP1-, and IL+ZDDP2-aged TWC samples are shown in Figures 4.31 (a) and (b), respectively. With regard to the pore volume shown in Figure 4.31 (a), the pore volume of all the TWC samples exposed to the lubricant additives is reduced compared with the NA-aged TWC sample. The ZDDP2- and IL+ZDDP2-aged TWC samples have the highest pore volume reduction of 20%, while ZDDP1- and IL+ZDDP1-aged TWC samples experience a lower reduction of pore volume 6.5%. In contrast to the pore volume, the pore size of all engine aged TWC samples is relatively similar, as shown in Figure 4.31 (b). Such results indicate that P compounds accumulate in the pores without blocking the pores, thereby decreasing the pore volume but not a decrease in pore size. This is in agreement with the results obtained by Marja-Liisa [170], which is investigated the effects of P on Pt/Pd-based diesel oxidation catalysts (DOCs) consisted of γ-Al_2O_3 support with Ce-Zr mixed oxides.

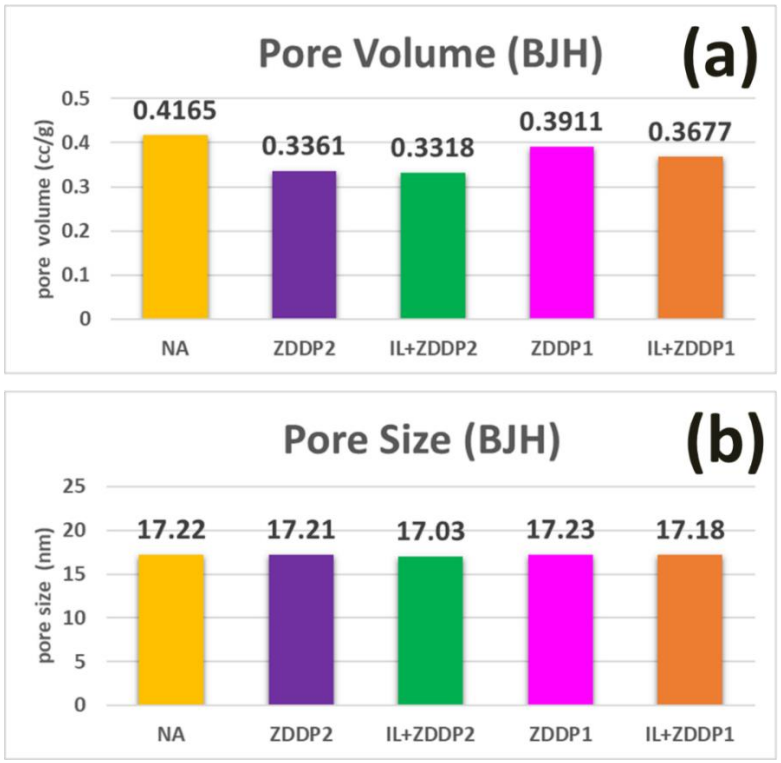

Figure 4.31 (a) Pore volume and (b) pore size (BJH method) measurements of NA-, ZDDP1-, ZDDP2-, IL+ZDDP1-, and IL+ZDDP2-aged TWC samples.

The XRD patterns of the NA-, ZDDP1, ZDDP2-, IL+ZDDP1- and IL+ZDDP2-aged TWC samples are presented in Figure 4.32. As presented in Section 4.1.2, the peaks denoted by (▼), (■), (◆), and (●) are assigned to $Ce_{1-x}Zr_xO_2$, $BaSO_4$, Pd, and PdO, respectively. For the NA-aged TWC sample, the much smaller peaks at 2θ = 21.7, 26.4, and 28.5° are due to interferences from the cordierite. Despite efforts to remove only the washcoat from the cordierite substrate, all washcoat powder samples are invariably contaminated with the cordierite substrate to a certain extent. The peaks for cordierite are denoted by

(○). The intensity of $CePO_4$ peaks (♠) at 2θ = 21.7 and 28.5° for the ZDDP2-aged TWC sample is stronger than that for the ZDDP1-, IL+ZDDP1-, and IL+ZDDP2-aged TWC samples. The results of EPMA show that the ZDDP2-aged TWC sample has the highest P on the washcoat, which is similar to the result of the XRD patterns. As mentioned before, although Zn is a major component of ZDDP1 and ZDDP2 lubricant additives, Zn-related peaks such as $Zn_2P_2O_4$ and etc. are not observed in the XRD patterns of all TWC samples exposed to lubricant additives in the present study, which is in contrast to previous studies in which $Zn_2P_2O_4$ is observed [127,134]. The intensity of the Pd peak at 2θ = 39.6° for TWC samples exposed to lubricant additives appears to be stronger than that for the NA-aged TWC sample, indicating the additional impact of additives on the sintering of Pd particles, which is in agreement with the XRD results obtained by Xie et al. [134].

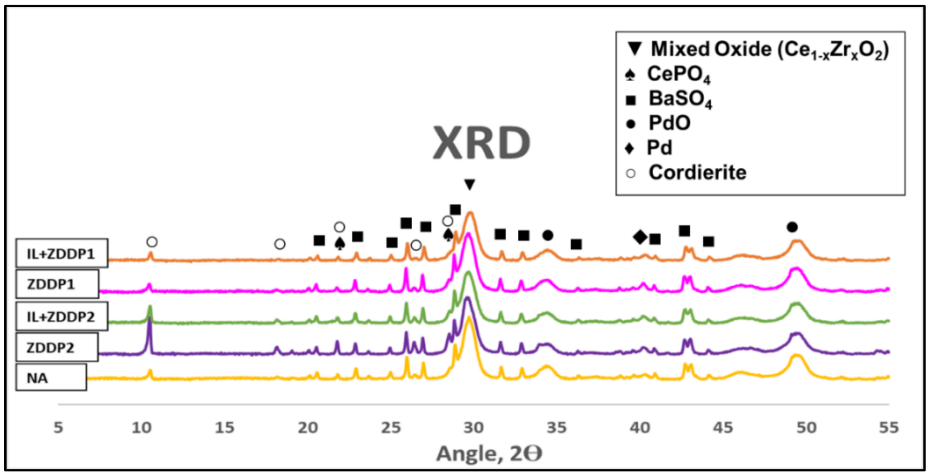

Figure 4.32 X-ray Diffraction (XRD) patterns for NA-, ZDDP1-, ZDDP2-, IL+ZDDP1-, and IL+ZDDP2-aged TWC samples.

Figure 4.33 (a) shows EPMA elemental maps of Zn for NA-, ZDDP1-, ZDDP2-, IL+ZDDP1-, and IL+ZDDP2-aged TWC samples. As seen in Figure 4.33 (a), a thin Zn layer is observed on the surface for ZDDP1- and ZDDP2-aged TWC samples, whereas only a trace amount of Zn is found on the washcoat surface of the IL+ZDDP1- and IL+ZDDP2-aged TWC samples. Since IL lubricant additive does not contain Zn, the concentration of Zn in the mixed additives of IL and ZDDP (IL+ZDDP1 and IL+ZDD2) is lower than that in the ZDDP only lubricant additive (ZDDP1 and ZDDP2), thus reducing the amount of Zn exposed. Also, as mentioned in Section 4.2.1.2, the Zn concentration in the ZDDP2 is higher than the ZDDP2, the ZDDP2-aged TWC sample shows a more contiguous Zn layer on the washcoat surface than the ZDDP1-aged TWC sample, where the layer is more incongruous. Furthermore, no evidence of penetration of Zn deep inside the washcoat is observed for all accelerated engine-aged TWC samples. On the other hand, the presence of Zn in the mixed IL and additives is much lower, and especially for IL+ZDDP1, it is barely visible. The results obtained from EPMA micrographs for Zn are in contrast to those obtained from ICP-OES analysis, in which the amount of Zn found in ZDDP1- and IL+ZDDP1-aged TWC samples is higher than in ZDDP2- and IL+ZDDP2-aged TWC samples. The discrepancy between the two results, as explained previously, is due to the limit of Zn detection of less than 0.08 wt% of the ICP-OES instrument.

Figure 4.33 (b) shows EPMA micrographs of P in the washcoat of NA-, ZDDP1-, ZDDP2-, IL+ZDDP1- and IL+ZDDP2-aged TWC samples. With the exception of the IL+ZDDP1-aged TWC sample, the TWCs exposed to the lubricant additives (ZDDP1, ZDDP2, and IL+ZDDP2) show a much higher level of P than the NA-aged TWC. As discussed in detail in Section 4.2.1.2, the EPMA micrographs of P for TWCs exposed to ZDDP1 and ZDDP2 lubricant additives show an overlayer of P on the washcoat surface and the penetration of P deep

inside the washcoat is much more significant than Zn. The P overlayer for the ZDDP2-aged TWC sample is more contiguous and contains more P, as reflected by the red color code, than the P overlayer of the ZDDP1-aged TWC sample. On the other hand, as in the case of Zn EPMA micrographs, the presence of P in the overlayer for the mixed IL and ZDDP additives is much lower, and especially IL+ZDDP1-aged TWC sample is indiscernible and similar to that of NA-aged TWC sample. The results obtained from EPMA are in contrast to the ICP-OES results, in which the concentration of P is highest (1.74 wt%) in IL+ZDDP2-aged TWC sample and similar in ZDDP1 and IL+ZDDP1-aged TWC samples (≈0.74 wt%). Regardless, the EMPA results clearly show that the presence of P on the catalyst surface and the penetration of P into the washcoat is the most dominant deactivation mechanism that likely causes the reduction in TWC performance.

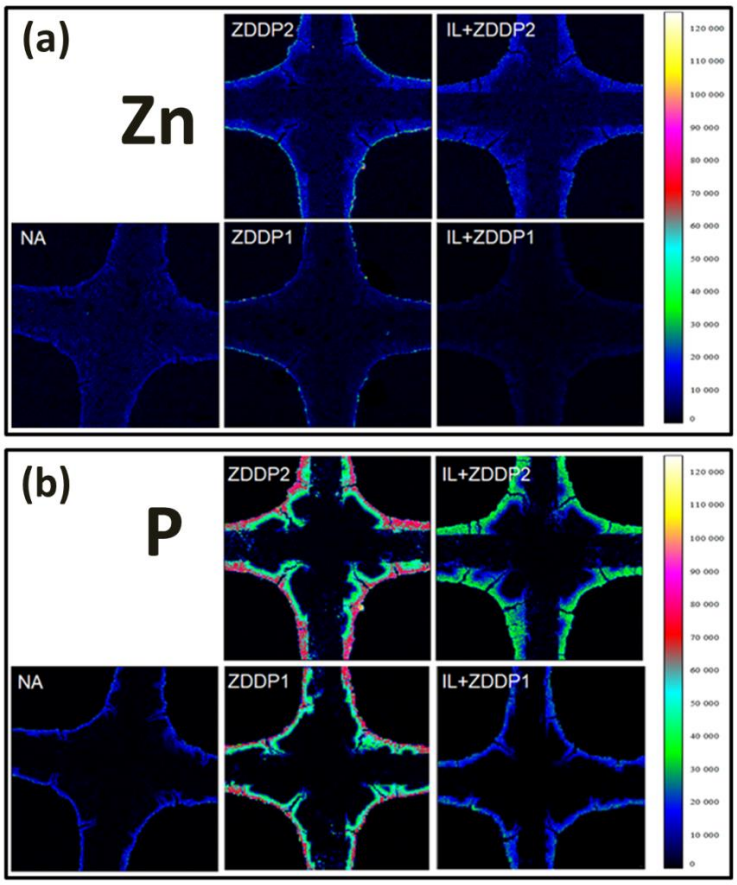

Figure 4.33 EPMA elemental maps of (a) Zn and (b) P at inlet of NA-, ZDDP1-, ZDDP2-, IL+ZDDP1- and IL+ZDDP2-aged TWC samples.

CHAPTER 5
MATHEMATICAL MODELING

This chapter presents a steady-state, one-dimensional continuous-stirred tank reactors (CSTRs) mathematical model implemented in MATLAB for predicting the performance of fresh and three-way catalyst (TWC). Section 5.1 describes the governing equations, the chemical reactions, and the global chemical reactions with kinetics parameters used in modeling the performance of Pd-based TWC. A comparison between the results predicted by the mathematical model and the results obtained from the bench flow reactor (BFR) for fresh and lubricant additive-poisoned TWC samples is presented in Section 5.2.

5.1 Mathematical Modeling of Pd-based TWC

5.1.1 Overview of TWC Model

The TWC reactor is modeled as a series of N equal-sized continuous-stirred tank reactors (CSTRs). The TWC model implemented in MATLAB was originally developed by Stuart Daw [171] of ORNL and is modified for predicting the performance of fresh and accelerated engine-aged Pd-based TWC samples under the BFR conditions. The accelerated engine-aged TWC samples include the thermally-aged TWC sample (NA), and the TWC samples that have been exposed to lubricant additives (IL, ZDDP1, and ZDDP2). In deriving the mathematical model, the following key assumptions are made:

1. The performance of all TWC monolith channels can be represented by a single channel, which implies that the performance of a multichannel TWC sample can be modeled as a single channel instead of the average of all channels.
2. The channel is assumed to be a series of N equal-sized continuous-stirred tank reactors (CSTRs) or stages arranged in the axial or flow direction, in which the gas-phase mass and energy balance equations can be expressed in terms of residence time or the reciprocal of the GHSV.
3. Each CSTR is assumed to be a one-dimensional steady-state, and well-mixed.
4. The operating pressure of all N continuous-CSTRs or stages is assumed to be 1 atm.
5. All reactions are assumed to occur only on the catalytic surface or the washcoat of the channel wall, whereas the reactions in the gas phase are neglected.
6. The inlet concentrations of all species at the first stage or the first CSTR are specified by using the composition of the simulated exhaust gases; and similarly, the inlet temperature at the first stage is given by the experimentally measured temperature of the inlet gas.
7. The temperature of each stage of the channel is interpolated from the temperatures measured from the type-K thermocouples embedded inside the TWC sample in the quartz tube reactor.
8. Mass transfer between gaseous species in the exhaust gases and the solid channel wall (the washcoat) is estimated using mass transfer correlations for fully-developed laminar flow.

9. The minimum number of stages or CSTRs is determined by increasing the number of stages until the change in the axial concentration profiles is negligible.
10. Since the CSTRs are connected in series, the exit conditions of the previous CSTR (or stage) become the inlet conditions of the next CSTR.
11. The gas composition, velocity, temperature, and pressure in the gas phase are uniform in each stage.
12. The species concentration and temperature are assumed to be uniform at the channel walls of each stage, which means that there are no spatial variations within the catalyst wall.
13. Using the series CSTR approximation, the mass balance system for each stage of the channel is reduced from partial differential equations (PDE) to a series of ordinary differential equations (ODEs).

5.1.2 Gas Phase Mass Balance

A gas phase mass balance on species i in a mixture containing n components (i = 1, 2, 3 … n) for each stage of the TWC channel can be expressed as follows:

$$\begin{bmatrix} Molar\ flow \\ rate\ of \\ species\ i\ IN\ at\ V \end{bmatrix} - \begin{bmatrix} Molar\ flow \\ rate\ of \\ species\ i\ OUT\ at\ V \end{bmatrix} - \begin{bmatrix} Moles\ transproted \\ to\ catalys\ surface \\ of\ species\ j\ within\ V \end{bmatrix} = \begin{bmatrix} Time\ rate\ of \\ change \\ of\ species\ i\ within\ V \end{bmatrix} \quad (5.1)$$

$$[F\ C_{i,f}] - [F\ C_i] - \left[k_{i,m}\left(C_i - C_{i,s}\right) V\right] = \left[\frac{dN_i}{dt}\right] \quad (5.2)$$

where

F is the volumetric flow rate through the CSTR in m^3/s,

$C_{i,f}$ is the concentration of species i at the reactor inlet in moles/m^3,

C_i is the concentration of species i at the bulk gas and stage outlet in moles/m^3,

$C_{i,s}$ is the concentration of species i at the solid phase (washcoat) in moles/m^3,

$k_{i,m}$ is the volumetric mass-transfer coefficient of species i in s^{-1},

V is the reactor volume in m^3,

N_i is number of moles of species i in the reactor in moles,

t is time in s.

Since the model of CSTRs in series assumes a constant reactor volume for each stage, the residence time, $\tau\ [s]\ =\ V\ /\ F$ is introduced into the gas-phase mass balance by dividing both sides of Equation 5.2 by the reactor volume.

$$\frac{1}{\tau}\left[C_{if} - C_i\right] - [k_{im}(C_i - C_{is})] = \left[\frac{dC_i}{dt}\right] \quad (5.3)$$

where τ is gas residence time in each stage (V / F) in s.

For steady-state the term on the right-hand side of Equation 5.3 vanishes, and the gas phase mass balance is given as:

$$\frac{1}{\tau}\left[C_{if} - C_i\right] - [k_{im}(C_i - C_{is})] = 0 \quad (5.4)$$

The initial condition of concentration of the i^{th} species at t = 0, $C_i = C_{i,0}$, is given by the composition of the simulated exhaust gases at the inlet condition. The

coefficient for the volumetric mass-transfer coefficient of the i^{th} species, $k_{i,m}$, is expressed by Equation 5.5, and it is related to the Sherwood number (Sh).

$$k_{i,m} = \frac{Sh_i \cdot D_{g,i} \cdot a_s}{D_h} \tag{5.5}$$

where

Sh_i is the Sherwood number of species i,

$D_{g,i}$ is the diffusivity of species i in m^2/s,

D_h is the characteristic hydraulic diameter of the channel in m,

a_s is the surface area per unit volume of washcoat in m^2/m^3.

The correlation given by Equation 5.6 is used to obtain the Sherwood number of the i^{th} species, Sh_i, for fully-developed laminar flow in a monolith reactor channel of a hydraulic diameter D_h [167,168].

$$Sh_i = 3.66 \left\{1 + 0.095\, Re\, Sc_i \frac{D_h}{L}\right\}^{0.45} \tag{5.6}$$

where

Re is the Reynolds number,

Sc_i is the Schmidt number of species i,

L is the channel length in m.

The expressions for the Reynolds number (Re) and the Schmidt number (Sc) of the i^{th} species are given by Equations 5.7 and 5.8, respectively.

$$Re = \frac{\rho_g v_m D_h}{\mu} \tag{5.7}$$

$$Sc_i = \frac{\mu}{\rho_g D_{g,i}} \tag{5.8}$$

where

ρ_g is the mass density of the exhaust gas in kg/m^3,

v_m is the mean mass average velocity of the gas in m/s,

μ is the dynamic viscosity of the fluid in kg/(m-s),

$D_{g,i}$ is the diffusivity of species i in m^2/s.

5.1.3 Solid Phase Mass Balance

The steady-state mass balance in the solid phase of species i in a mixture of n components (i = 1, 2, 3 … n) can be written as:

$$\begin{bmatrix} Moles\ transported \\ to\ catalyst\ surface \end{bmatrix} = \begin{bmatrix} Moles\ reacted \\ in\ catalytic\ reaction \end{bmatrix} \tag{5.9}$$

$$\left[k_{i,m}(C_i - C_{is})\right]V = V\sum_k R_{i,s}^k \tag{5.10}$$

where

$k_{i,m}$ is the volumetric mass-transfer coefficient of species i in s^{-1},

C_i is the concentration of species i in the bulk gas and at the stage exit in moles/m^3,

$C_{i,s}$ is the concentration of species i at the channel surface or the washcoat surface in moles/m^3,

V is the reactor volume in m^3,

$R_{i,s}^k$ is the surface reaction rate of species i in a k-step chemical reaction in moles/m^{3}s.

Dividing Equation 5.10 by the reactor volume,

$$\left[k_{i,m}(C_i - C_{is})\right] = \sum_k R_{i,s}^k \tag{5.11}$$

The specific surface reaction rate ($R_{i,s}$) given by Equation. 5.11 is typically expressed in terms of Arrhenius rate law,

$$\left[R_{i,s}^k\right] = \left[A_i^k \exp\left(-\frac{Ea_i^k}{R_g T_s}\right) C_{j,s}^m C_{i,s}^n\right] \tag{5.12}$$

where

m is the reaction order for species j,

n is the reaction order for species i,

A_i^k is the Arrhenius kinetic pre-exponential factor involving species i in a k-step chemical reaction in moles$^{(1\text{-}m\text{-}n)}$/m$^{3(1\text{-}m\text{-}n)}$-s,

Ea_i^k is Arrhenius activation energy involving species i in a k-step chemical reaction in kJ/mole,

$C_{j,s}$ is the concentration of j species at the solid-wall surface or the washcoat surface in moles/m^3,

$C_{i,s}$ is the concentration of i species at the solid-wall surface or the washcoat surface in moles/m^3,

R_g is the universal gas constant in kJ/mole-K,

T_s is the solid-wall or the washcoat temperature in K.

Therefore, the solid phase mass balance after combining Equations 5.11 and 5.12 is

$$\left[k_{i,m}(C_i - C_{is})\right] = \sum_k \left[A_i^k \exp\left(-\frac{E a_i^k}{R_g T_s}\right) C_{j,s}^m C_{i,s}^n\right] \tag{5.13}$$

The kinetic parameters of the TWC model, such as activation energy (E_a) and Arrhenius kinetic pre-exponential factor (A) for the surface reaction rate of species i in a k-step chemical reaction, are given in Table 5.2.

5.1.4 Gas Phase Energy Balance

The energy balance for the gas phase can be expressed as:

$$\begin{bmatrix} Time\ rate\ change \\ in\ gas\ phase \\ energy \end{bmatrix} = \begin{bmatrix} Heat\ added\ to\ gas \\ from\ surface \\ convection \end{bmatrix} + \begin{bmatrix} Heat\ generated \\ in\ gas\ phase \\ reaction \end{bmatrix} - \begin{bmatrix} Enthalpy\ increase \\ due\ to \\ temperature\ rise \\ in\ gas\ phase \end{bmatrix} \tag{5.14}$$

Since the gas phase reactions are neglected (see assumption 5), the heat generated term in the gas phase reaction is not included, which is written as:

$$V\rho_g c_{pg} \frac{dT_g}{dt} = h_g A_s\left(T_s - T_g\right) - F\rho_g c_{pg}\left(T_g - T_{g,i}\right) \tag{5.15}$$

where

V is the reactor volume in m^3,

ρ_g is the mass density of the exhaust gas in kg/m^3,

c_{pg} is the specific heat of the exhaust gas in J/kg-K,

T_g is the exhaust gas temperature in K,

$T_{g,i}$ is the exhaust gas temperature at the inlet of the stage inlet in K,

T_s is the solid-wall or the washcoat temperature in K,

h_g is the convective heat transfer coefficient between the bulk gas and washcoat in W/m^2-K,

A_s is the surface area in m^2,

F is the volumetric flow rate through the CSTR in m^3/s.

A_s in the gas phase mass balance equation, the residence time, τ, is introduced by dividing both sides of Equation 5.15 by the reactor volume,

$$\rho_g c_{pg} \frac{dT_g}{dt} = h_g a_s (T_s - T_g) - \frac{\rho_g c_{pg} (T_g - T_{g,i})}{\tau} \quad (5.16)$$

For steady-state, the term in the left-hand side of Equation 5.16 varnishes, and the energy balance of the gas phase in each stage is simplified to

$$h_g a_s (T_s - T_g) + \frac{\rho_g c_{pg} (T_{g,i} - T_g)}{\tau} = 0 \quad (5.17)$$

5.1.5 Solid Phase Energy Balance

The energy balance for solid phase can be written as:

$$\begin{bmatrix} Time\ rate\ change \\ in\ solid\ phase \\ energy \end{bmatrix} = \begin{bmatrix} Heat\ transfferred \\ from\ solid \\ conduction, \\ loss\ by\ covection \\ and\ radiation \end{bmatrix} - \begin{bmatrix} Heat\ released \\ by\ reaction \end{bmatrix} \qquad (5.18)$$

The model assumes that the temperature at each point in time at the channel wall at each stage is uniform, so there is no conduction within the washcoat. In addition, radiation losses are neglected in this model. With these assumptions, the solid phase energy balance can be expressed as:

$$V\rho_s c_{ps}\frac{dT_s}{dt} = h_g A_s\left(T_g - T_s\right) + h_a A_w(T_o - T_s) - V\sum_k R_k \Delta H_k \qquad (5.19)$$

where

V is the reactor volume in m^3,

ρ_s is the density of the solid-wall or the washcoat in kg/m^3,

c_{ps} is the specific heat of the washcoat and solid wall in J/kg-K,

T_g is the exhaust gas temperature in K,

T_s is the washcoat and solid-wall temperature in K,

T_0 is the ambient temperature in K,

h_g is the convective heat transfer coefficient between the bulk gas and washcoat in W/m^2-K,

h_a is the convective heat-transfer coefficient between the ambient atmosphere and the catalyst wall/washcoat in W/m^2-K,

A_s is the surface area in m^2,

A_w is the external heat transfer surface in m^2,

F is the volumetric flow rate through the CSTR in m^3/s,

R_k is the specific rate of the k reaction,
ΔH_k is the heat generated of the k-step reaction in J/mol.

Dividing both sides of the Equation 5.19 by the reactor volume, the solid phase energy balance can be given as:

$$\rho_s c_{ps} \frac{dT_s}{dt} = h_g a_s (T_g - T_s) - h_a a_w (T_s - T_o) - \sum_k R_k \Delta H_k \qquad (5.20)$$

where a_s and a_w are the surface area per volume of washcoat and the external heat transfer surface per volume, respectively, in m^2/m^3.

Finally, steady-state energy balance for solid phase (washcoat) at each stage can be written as:

$$h_g a_s (T_g - T_s) - h_a a_w (T_s - T_o) - \sum_k R_k \Delta H_k = 0 \qquad (5.21)$$

As seen in Equation 5.21, to solve the steady-state energy balance for the solid phase requires a knowledge of the heat transfer between the wall of the TWC and the ambient, from which the convective heat-transfer coefficient between the ambient atmosphere and the catalyst wall, h_g, can be determined. Furthermore, the heat generated from the surface reactions, i.e., the last term on the left-hand side of Equation 5.21, varies with the reaction rates, none of which is known precisely. Thus, in order to reduce the additional computational complexity in the computational model, the catalyst surface temperature in each stage is obtained by interpolating from the temperatures measured from the type-K thermocouples embedded inside the TWC sample in the quartz tube reactor (see assumption 7).

In summary, the governing equations for the one-dimensional, steady-state of N equal-sized CSTRs in series are shown in Equations 5.22-5.25, and the symbols and units of the parameters used in the model are given in Table 5.1.

Gas phase mass balance:

$$\frac{1}{\tau}\left[C_{if} - C_i\right] - \left[k_{im}(C_i - C_{is})\right] = 0 \tag{5.22}$$

Gas phase energy balance:

$$h_g a_s\left(T_s - T_g\right) + \frac{\rho_g c_{pg}\left(T_{g,i} - T_g\right)}{\tau} = 0 \tag{5.23}$$

Solid phase mass balance:

$$\left[k_{i,m}(C_i - C_{is})\right] = \sum_k R_{i,s}^k \tag{5.24}$$

Solid phase energy balance:

$$h_g a_s\left(T_g - T_s\right) - h_a a_w(T_s - T_o) - \sum_k R_k \Delta H_k = 0 \tag{5.25}$$

Table 5.1 Notation for mass and energy balance equations.

F	Volumetric flow rate through the reactor (m^3/s)
V	Reactor volume (m^3)
A_s	Surface area (m^2)
A_w	External heat transfer surface (m^2)
$\mathrm{D_h}$	Characteristic hydraulic diameter of the channel (m)
$D_{g,i}$	Diffusivity of species i (m^2/s)
L	Monolith channel length (m)
τ	Gas residence time in each stage (s)
$\mathrm{R_g}$	Ideal gas constant [kJ/mole-K]
c_{pg}	Specific heat of the exhaust gases (J/kg-K)
c_{ps}	Specific heat of the washcoat and solid wall (J/kg-K)
$\mathrm{C_i}$	Concentration of species i at the bulk gas and stage outlet ($moles/m^3$)
$\mathrm{C_{i,f}}$	Concentration of species i at the reactor inlet ($moles/m^3$)
$\mathrm{C_{i,s}}$	Concentration of i species at the solid phase ($moles/m^3$)
$\mathrm{C_{j,s}}$	Concentration of j species at the solid phase ($moles/m^3$)
$\mathrm{N_i}$	Number of moles of species i in the reactor (moles)
h_g	Heat transfer coefficient between the bulk gas and washcoat (W/m^2-K)
h_a	Convective heat transfer coefficient between the ambient atmosphere and the catalyst wall/washcoat (W/m^2-K)
$k_{\mathrm{i,m}}$	Mass transfer coefficient (s^{-1})
R_{k}	k-step chemical reaction rate (mol/m^3-s)
t	Time (s)
$\mathrm{T_g}$	Exhaust gas temperature (K)

Table 5.1 continued

$T_{g,i}$	Exhaust gas temperature at the inlet of the stage inlet (K)
T_s	Washcoat and solid-wall temperature (K)
T_o	Ambient temperature (K)
A_i^k	Arrhenius kinetic pre-exponential factor involving species i in a k-step chemical reaction (moles$^{(1-m-n)}$/m$^{3(1-m-n)}$-s), where, m and n are the reaction order for species j and i, respectively
Ea_i^k	Arrhenius activation energy involving species i in a k-step chemical reaction (kJ/mole)
$R_{i,s}^k$	Surface reaction rate of species i in a k-step chemical reaction (moles/m^{3}s)
R_k	Specific rate of the k reaction
ΔH_k	Heat generated of the k-step reaction (J/mol)
ρ_g	Mass density of the exhaust gas (kg/m^3)
ρ_s	Density of the washcoat and solid wall in the catalyst (kg/m^3)
v_m	Mean mass average velocity of the gas (m/s)
μ	Dynamic viscosity of the fluid (kg/(m-s))
a_s	Surface area per volume of washcoat (m^2/m^3)
a_w	External heat transfer surface per volume (m^2/m^3)

The model considers 20 different global reactions and 11 species, such as N_2, H_2, CO, NO, C_3H_6, C_3H_8, NH_3, N_2O, O_2, H_2O, and CO_2. The kinetic parameters of Gong's TWC model [169,170] are used as base kinetics in this modified MATLAB-implemented mathematical model. However, since kinetics from Gong have been obtained from data based on different TWCs, it is necessary to adjust parameters such as activation energy and pre-exponential factor in the global reactions, until the results obtained from the mathematical

model agree with those obtained from a temperature sweep experiment carried out in the BFR for a fresh TWC sample. The reaction rate and kinetic parameters of CO and UHCs oxidation, NO reduction, water gas shift (WGS), steam reforming (SR) reaction, oxygen storage, formation of NH_3, and formation of N_2O for the Pd-based TWC model are given in Table 5.2. In the MATLAB code, active PGM loading and dispersion are included in Equation 5.26 via the active site density, α, which can be varied, from which the loss of the Pd active sites in the washcoat of the TWC is modeled.

$$R_i = r_i \cdot \alpha \tag{5.26}$$

where

R_i is total reaction rate of species i in mole/m^3s,

r_i is specific reaction rate of species i in mole/mole-site/s,

α is active site density of catalyst in mole-site/m^3.

The specific reaction rate (r_i) and the rate coefficient (k_i) are given in Equations 5.27 and 5.28, respectively.

$$r_i = k_i \cdot [C_{i,s}] \cdot [C_{j,s}] \cdot f(G_i) \cdot C(\theta_i) \tag{5.27}$$

where

$C_{i,s}$ is the concentration of species i at the channel surface or the washcoat surface in moles/m^3,

$C_{j,s}$ are the concentration of species j at the channel surface or the washcoat surface in moles/m^3,

$f(G_i)$ is the inhibition function,

$C(\theta_i)$ is the surface coverage.

$$k_i = A_i \cdot T^b \cdot exp\left(-\frac{E_i}{R_u T}\right) \tag{5.28}$$

Table 5.2 Kinetic parameters of TWC model [175].

No.	Reaction	A	b	E(J/mole)	Conc*f(Gk)	C(θ)
1	$CO + 0.5O_2 \rightarrow CO_2$	3.642E+13	0	138450	$[CO]*[O_2]/G(1)$	1
2	$C_3H_6 + 4.5O_2 \rightarrow 3CO_2 + 3H_2O$	3.170E+13	0	130530	$[C_3H_6]*[O_2]/G(1)$	1
3	$C3H_8 + 5O_2 \rightarrow 3CO_2 + 4H_2O$	9.404E+14	0	165160	$[C_3H_8]*[O_2]/G(1)$	1
4	$H_2 + 0.5O_2 \rightarrow H_2O$	1.67E+13	0	111450	$[H_2]*[O_2]/G(1)$	1
5	$CO + NO \rightarrow CO_2 + 0.5N_2$	3.154E+09	0	52374	$[CO]*[NO]/G(1)$	1
6	$C_3H_6 + 9NO \rightarrow 3CO_2 + 3H_2O + 4.5N_2$	6.242E+09	0	80063	$[C_3H_6]*[NO]/G(1)$	1
7	$H_2 + NO \rightarrow H_2O + 0.5N_2$	4.642E+08	0	69237	$[H_2]*[NO]/G(1)$	1
8	$CO + H_2O \leftrightarrow CO_2 + H_2$	1.800E+00	0	56720	$([CO]*[H_2O]-[H_2]*[CO_2]/G(2))/G(1)$	1
9	$C_3H_6 + 3H_2O \rightarrow 3CO + 6H_2$	1.230E+05	0	81920	$[C_3H_6]*[H_2O]/G(1)$	1
10	$NH_3+1.25O_2 \rightarrow NO+1.5H_2O$	3.000E+13	0	139300	$[NH_3]*[O_2]/G(1)$	1
11	$NO+2.5H_2 \rightarrow NH_3+H_2O$	7.390E+09	0	44720	$[NO]*[H_2]/G(1)$	1
12	$NH_3+1.5NO \rightarrow 1.25N_2+1.5H_2O$	1.500E+10	0	121400	$[NH_3]*[NO]/G(1)$	1
13	$NO+1/18C_3H_6 \rightarrow 0.5N_2O+1/6CO_2+1/6H_2O$	6.720E+12	0	83700	$[NO]*[C_3H_6]*G(3)/G(1)$	1
14	$N_2O+1/9C_3H_6 \rightarrow N_2+1/3CO_2+1/3H_2O$	1.200E+15	0	135000	$[N_2O]*[C_3H_6]/G(1)$	1
15	$2Ce_2O_3 + O_2 \rightarrow 4CeO_2$	2.943E+00	0	5296	$[O_2]$	1-θ
16	$Ce_2O_3 + NO \rightarrow 2CeO_2 + 0.5N_2$	7.920E+02	0	25101	$[NO]$	1-θ
17	$CO + 2CeO_2 \rightarrow Ce_2O_3 + CO_2$	1.824E-01	0	31768	$[CO]$	θ
18	$C_3H_6 + 12CeO_2 \rightarrow 6Ce2O_3 + 3CO + 3H_2O$	1.357E+01	0	39070	$[C_3H_6]$	θ
19	$C_3H_8 + 14CeO_2 \rightarrow 7Ce_2O_3 + 3CO + 4H_2O$	1.770E+01	0	39680	$[C_3H_8]$	θ
20	$H_2 + 2CeO_2 \rightarrow Ce2O_3 + H_2O$	2.845E+00	0	31768	$[H_2]$	θ

Remark:

$$G(1) = \left(1 + 4.314 \cdot exp\left(\frac{485}{T_s}\right) \cdot [CO] + 1.289 \cdot exp\left(\frac{166}{T_s}\right) \cdot [C_3H_6]^2\right) \cdot \left(1 + 2.147 \cdot 10^{-4} \cdot exp\left(\frac{10163}{T_s}\right) \cdot [CO]^2 \cdot [C_3H_6]^2\right) \cdot \left(1 + 8.699 \cdot 10^5 \cdot exp\left(\frac{3685}{T_s}\right) \cdot [NO]\right)$$

$$G(2) = exp\left(-\frac{-41034 + 44.19 \cdot T_s - 5.553 \cdot 10^{-3} \cdot T_s}{8.314 \cdot T_s}\right)$$

$$G(3) = f_0 + exp\left(-\frac{(T_s - T_{m1})^2}{\sigma_1}\right) \cdot exp\left(-\frac{(T_s - T_{m2})^2}{\sigma_2}\right)$$

where T_{m1}, T_{m2}, σ_1, σ_2, and f_0 are 400°C, 550°C, 280, 90, and 0.05, respectively.

5.2. Results of Mathematical Model

As mentioned in Section 5.1, the TWC is modeled as a steady-state, one-dimensional of N-continuous-stirred tank reactors (CSTRs) in series implemented in MATLAB. The mathematical model takes into account gas-phase energy balance, gas-phase species balance, solid-phase energy balance, and catalytic surface species balance. The TWC model considers 14 different global reactions and 11 species, such as N_2, H_2, CO, NO, C_3H_6, C_3H_8, NH_3, N_2O, O_2, H_2O, and CO_2. Table 5.3 shows the specifications of the Pd-based TWC sample used in the model simulation, and the gas composition of the simulated gas is given in Table 5.4.

Table 5.3 Specifications of monolith Pd-based TWC.

Ratio of PGM (Pd: Rh)	8:1
Total PGM loading (g/ft^3)	200
Length (cm)	2.54
Diameter (cm)	2.2
Wall thickness (mm)	0.12
Cell density (cpsi)	600

Table 5.4 Simulated gas composition for stoichiometric gasoline engines.

Components	Stoichiometric
O_2 (%)	0.73
H_2O (%)	13
CO_2 (%)	13
CO (ppm)	5000
NO (ppm)	1000
C_3H_6 (ppm)	1000
C_3H_8 (ppm)	100
N_2 (%)	Balanced
SV (hr^{-1})	60K

5.2.1 Kinetics Validation

Before simulating the performance of the engine-aged TWC samples, the kinetic parameters provided by Gong [175] have to be adjusted until the results obtained from the mathematical model are similar to those obtained from the temperature sweep experiment of a fresh TWC sample. As a reminder in the temperature sweep experiment, the conversion of NO, CO, C_3H_6, and C_3H_8 of a fresh TWC sample is obtained in the BFR stoichiometric condition of 0.73% O_2 with inlet gas temperature varying between 100°C and 630°C. Table 5.5 lists the adjusted kinetic parameters along with those given by Gong [175]. As seen in the table, in order to match the results of the mathematical model and those obtained

from the BFR for a fresh TWC sample, pre-exponential factor, A, and the activation energy, E, in almost all global reactions considered have to be adjusted.

Table 5.5 Adjusted kinetic parameters compared to Gong's kinetic parameters of the Pd-based TWC model.

No.	Reaction	Jian Gong [175]		Adjusted	
		A	E(J/mole)	A	E(J/mole)
1	$CO + 0.5O_2 \rightarrow CO_2$	3.642E+13	138450	2.540E+13	93450
2	$C_3H_6 + 4.5O_2 \rightarrow 3CO_2 + 3H_2O$	3.170E+13	130530	9.910E+13	105500
3	$C_3H_8 + 5O_2 \rightarrow 3CO_2 + 4H_2O$	9.404E+14	165160	4.004+16	157160
4	$H_2 + 0.5O_2 \rightarrow H_2O$	1.67E+13	111450	1.670E+13	110450
5	$CO + NO \rightarrow CO_2 + 0.5N_2$	3.154E+09	52374	2.154E+12	85374
6	$C_3H_6 + 9NO \rightarrow 3CO_2 + 3H_2O + 4.5N_2$	6.242E+09	80063	7.242E+13	105063
7	$H_2 + NO \rightarrow H_2O + 0.5N_2$	4.642E+08	69237	2.642E+09	69237
8	$CO + H_2O \leftrightarrow CO_2 + H_2$	1.800E+00	56720	1.800E+00	56720
9	$C_3H_6 + 3H_2O \rightarrow 3CO + 6H_2$	1.230E+05	81920	6.430E+08	78620
10	$NH_3+1.25O_2 \rightarrow NO+1.5H_2O$	3.000E+13	139300	7.000E+12	92300
11	$NO+2.5H_2 \rightarrow NH_3+H_2O$	7.390E+09	44720	2.501E+10	61020
12	$NH_3+1.5NO \rightarrow 1.25N_2+1.5H_2O$	1.500E+10	121400	8.500E+12	150400
13	$NO+1/18C_3H_6 \rightarrow 0.5N_2O+1/6CO_2+1/6H_2O$	6.720E+12	83700	1.920E+13	65000
14	$N_2O+1/9C_3H_6 \rightarrow N_2+1/3CO_2+1/3H_2O$	1.200E+15	135000	3.900E+15	120000

Using the adjusted kinetics in Table 5.5, Figures 5.1 (a) to (d) show the comparison between the conversion of NO, CO, C_3H_6, and C_3H_8 from the BFR to those from the mathematical models obtained using Gong's kinetic parameters and the adjusted kinetics for a fresh TWC sample at the stoichiometric condition of 0.73% O_2 with inlet gas temperature varying between 100°C and 630°C. In addition, the formation of NH_3 and N_2O for the three cases under consideration is shown in Figures 5.1 (e) and (f), respectively. The conversion of NO, CO, C_3H_6, and C_3H_8 and formation of NH_3 and N_2O using Gong's kinetics are significantly different from those obtained from the BFR. Gong's kinetics results in significant reductions in CO, C_3H_6, and C_3H_8 conversions (Figures 5.1 (b), (c), and (d)), whereas the formation of N_2O is overpredicted with the formation of N_2O occurring at the temperature as low as 100°C (Figure 5.1 (f)). As seen in Figures 5.1 (a) and (e), significant formation of the N-containing species such as NH_3 and especially N_2O from NO using Gong's kinetics occurs at the temperature as low as 100°C compared to that obtained from the BFR. Furthermore, the trend of N_2O formation using Gong's kinetics deviates significantly from the experimental result. Consequently, the maximum NO conversion using Gong's kinetics occurs at a much lower temperature than that from the BFR. Therefore, to obtain a better match for the results obtained from the mathematical model and the BFR, it is imperative that the kinetic parameters suggested by Gong need to be adjusted.

As seen in Figure 5.1, the results obtained from the model using adjusted kinetic parameters agree quite well with those obtained from the experiment, except for NO conversion at temperatures between 250°C and 400°C (Figure 5.1 (a)). As explained in detail in Section 4.1.1, NO conversion is much more complex due to a large number of NO reductants such as CO, H_2, C_3H_6, C_3H_8, etc., and hence more global reactions, which in turn increases the complexity of

the conversion of NO. On the other hand, using the adjusted kinetic parameters, the conversion of CO, C_3H_6, and C_3H_8 and formation of NH_3 and N_2O obtained from the mathematical model agree quite well with the experimental results obtained from the BFR. Therefore, it is expected that the mathematical model with the adjusted kinetic parameters could be used to identify the most dominant deactivation mechanism in the NA-aged TWC sample as well as TWC samples exposed to lubricant additives.

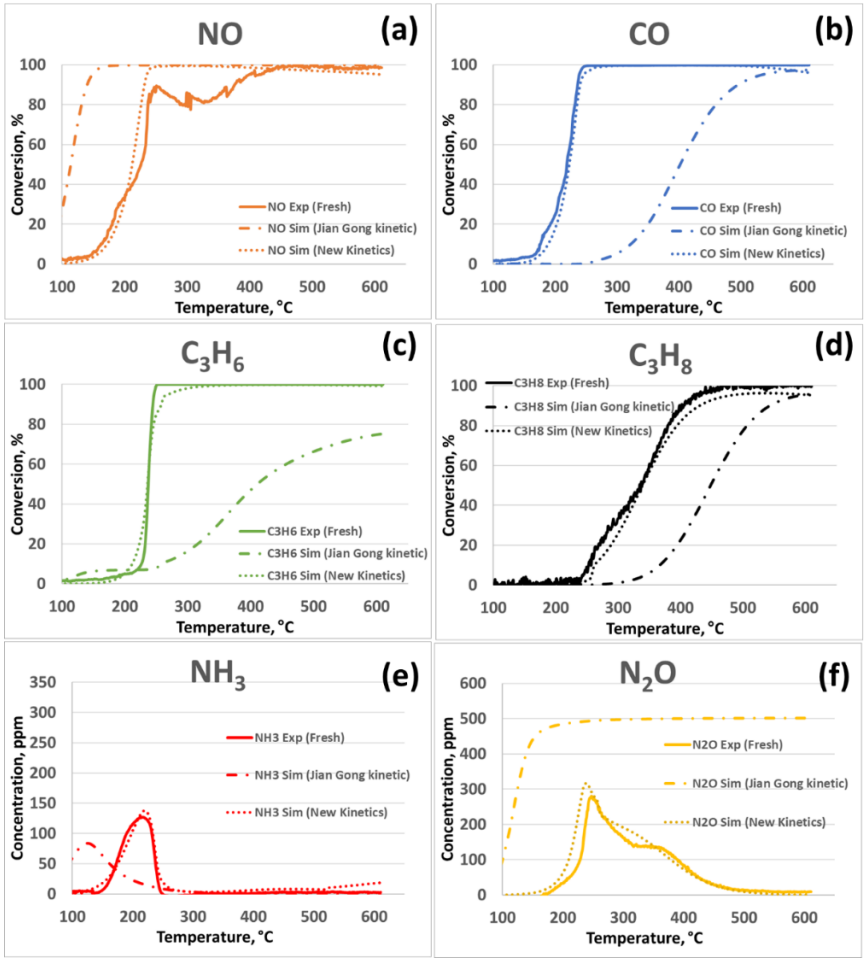

Figure 5.1 Comparing results for the conversion of (a) NO, (b) CO, (c) C_3H_6, (d) C_3H_8, and formation of (e) NH_3 and (f) N_2O obtained from BFR for fresh TWC sample (solid lines) and computational models (dashed lines) at the stoichiometric condition (0.73% O_2) at inlet gas temperatures between 100°C and 630°C.

5.2.2 Simulation Study of TWC Deactivation Mechanisms

After adjusting the kinetic parameters to fit the light-off curves of the fresh TWC sample, the mathematical model is then used to predict the performance of the NA-aged TWC samples as well as those exposed to lubricant additives. One of the dominant deactivation mechanisms of the TWC identified in Chapter 4 is the reduction in the BET surface area as a result of thermal aging as well as poisoning from lubricant additives. The reduction in the BET surface area can lead to a reduction of PGM dispersion, which in turn results in a loss of Pd active sites. It is possible to model the loss of Pd active sites on the washcoat of the TWC by reducing the PGM loading in the simulation.

Figure 5.2 shows the concentration of NO, CO, C_3H_6, C_3H_8, NH_3, and N_2O as a function of PGM loading of 50, 100, and 200 g/ft^3 at an O_2 concentration of 0.73% and with inlet gas temperature varying between 100°C and 600°C. For comparison purposes, the PGM loading for the fresh TWC sample used in the present study is 200 g/ft^3. As seen in the figure, as expected at a given temperature, the higher the PGM loading, the lower the concentration of NO, CO, C_3H_6, and C_3H_8, and consequently, the higher conversion of these species. On the other hand, for the inlet gas temperatures between 100 and 230°C the higher the PGM loading, the higher the formation of NH_3, and the lower the formation of N_2O at inlet gas temperatures above 230°C, which is opposite to the results obtained from the experiment. In addition, no double peak is observed for the NO conversion curves predicted by the model at temperatures between 250°C and 400°C, which is different from the results obtained from the experiment. Based on the results of major species such as CO, NO, C_3H_6 and C_3H_8, it is possible to model the deactivation of Pd-based TWCs either from thermal aging or poisoning from lubricant additives by the loss of PGM active sites, which can be simulated by the reduction in the PGM loading.

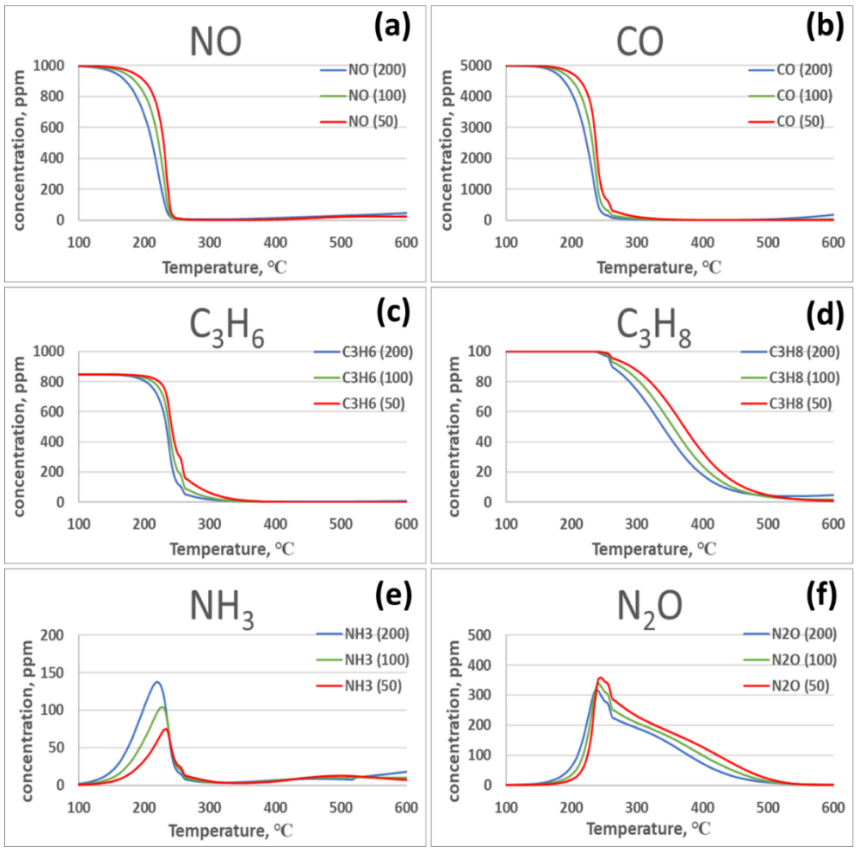

Figure 5.2 Effect of PGM loading (50, 100, and 200 g/ft^3) on the concentration of NO, CO, C_3H_6, C_3H_8, NH_3, and N_2O at the stoichiometric condition (0.73% O_2) at inlet gas temperatures between 100°C and 600°C.

To simulate the degradation in the performance of the NA-aged TWC sample, the PGM loading of the catalyst is reduced by 20% from 200 to 160 g/ft^3. Figures 5.3 (a) to (d) show the comparison between the mathematical model and BFR results for the conversion of NO, CO, C_3H_6, and C_3H_8 of the NA-aged TWC sample at the stoichiometric condition as a function of the inlet gas temperature.

The formation of NH_3 and N_2O is also shown in Figures 5.3 (e) and (f), respectively. The dashed and solid lines represent the results obtained from the computational model and the experimental results, respectively. As seen in Figures 5.3 (b) and (c), the CO and C_3H_6 conversion results obtained from the model with a PGM loading of 160 g/ft^3 are quite similar with those obtained from the BFR for the NA-aged TWC sample. For the conversion of NO, the mathematical model underpredicts at inlet gas temperatures below 200°C, but overpredict at inlet gas temperatures above 200°C, as seen in Figure 5.3 (a). On the other hand, as seen in Figure 5.3 (d), the mathematical model underpredicts the conversion C_3H_8 at all inlet gas temperatures. As shown in Figure 4.5 (d) of Section 4.1.1, the conversion of C_3H_8 for the NA-aged TWC sample is better than that for the fresh TWC sample, which is in contrast with the results predicted by the mathematical model as PGM loading decreases (see Figure 5.2 (d)). The discrepancy in the conversion of C_3H_8 between the model and the experiment the NA-aged TWC sample is about 20% at inlet gas temperatures above 250°C. In addition, even though the formation of NH_3 predicted by the mathematical model exhibits the same trend in the inlet gas temperatures between 150°C and 250°C, it is much less than the experimental result, as seen in Figure 5.3 (e). On the other hand, the formation of N_2O is the opposite, in which the model overpredicts the formation of N_2O.

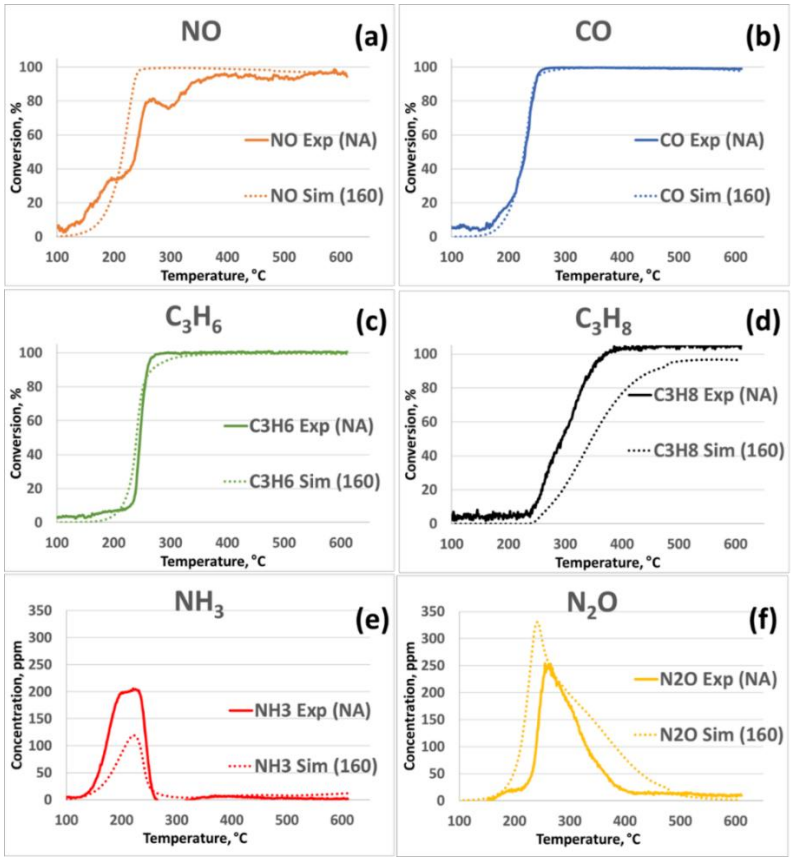

Figure 5.3 Comparison between the conversion of (a) NO, (b) CO, (c) C_3H_6, (d) C_3H_8, and formation of (e) NH_3 and (f) N_2O obtained from BFR for NA-aged TWC sample (solid lines) and mathematical model with a PGM loading of 160 g/ft^3 or 10% reduction (dashed lines) at the stoichiometric condition of 0.73% O_2 with inlet gas temperature varying between 100°C and 630°C.

Since the ZDDP2-aged TWC sample experiences more severe degradation in performance degradation than other TWC samples, it is selected to be used to compare the modeling results to confirm the clear catalyst deactivation, especially poisoning. As in the case of the NA-age TWC sample,

the performance degradation of the ZDDP2-aged TWC sample is simulated by a loss of PGM dispersion or active sites with a PGM loading of 120 g/ft^3, a 40% reduction in PGM loading from the fresh TWC sample of 200 g/ft^3. Figures 5.4 (a) to (d) show the comparison between the mathematical model and BFR results for the conversion of NO, CO, C_3H_6, and C_3H_8 of the ZDDP2-aged TWC sample at the stoichiometric condition of 0.73% O_2 as a function of the inlet gas temperature. As seen in Figures 5.4 (b), (c), and (d), the conversion of CO, C_3H_6, and C_3H_8 for the ZDDP2-aged TWC sample obtained from the model is similar with that obtained from the experiment. On the other hand, the discrepancy in NO conversion (Figure 5.4 (a)) and NH_3 generation (Figure 5.4 (e)) between the model and the experiment is similar, as in the case of the NA-aged TWC sample for the same reasons explained earlier.

In summary, by adjusting the kinetic parameters in the global reactions proposed by Gong, then the mathematical model is suitable for simulating the performance of the fresh TWC sample. Furthermore, for major species such as NO, CO, C_3H_6, and C_3H_8, it is possible to model the performance degradation of the TWCs due to thermal sintering and lubricant additive poisoning solely as the loss of PGM dispersion or the reduction of PGM active sites. The reduction of PGM active sites is modeled as the decrease in the original PGM loading of the fresh TWC. On the other hand, for the formation of minor species such as NH_3 and N_2O, the model can predict only qualitatively but not quantitatively.

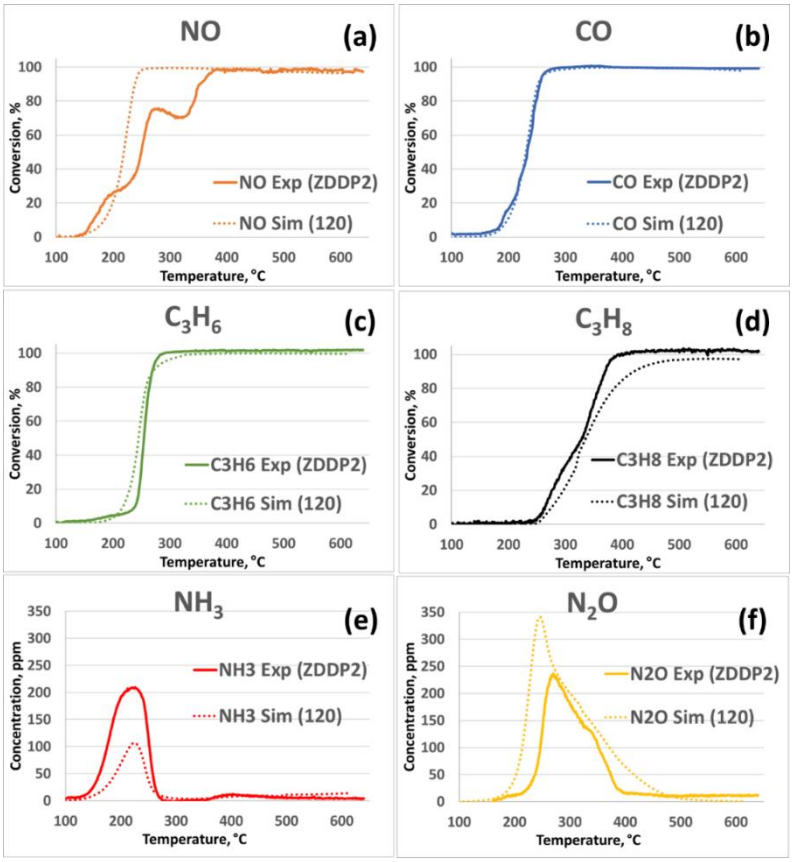

Figure 5.4 Comparison between the conversion of (a) NO, (b) CO, (c) C_3H_6, (d) C_3H_8, and formation of (e) NH_3 and (f) N_2O obtained from experimental for ZDDP2-aged TWC sample (solid lines) and mathematical model with a PGM loading of 120 g/ft^3 or 40% reduction (dashed lines) at the stoichiometric condition of 0.73% O_2 at inlet gas temperature varying between 100°C and 630°C.

CHAPTER 6
CONCLUSIONS AND RECOMMENDATIONS

In the present investigation, the effects of lubricant additives (IL, ZDDP1, ZDDP2, IL+ZDDP1, and IL+ZDDP2) on the performance of Pd-based TWC are investigated and compared with the thermally-aged TWC sample (no additive or NA). The accelerated thermal aging and poisoning of the TWC samples is carried out in an engine bench consisting of a 3.5 kW Westerbeke SBCG gasoline generator or Genset engine for 24 hours at a catalyst mid-bed temperature of 700°C. After accelerated thermal aging and poisoning, the performance of the TWC is carried out in a BFR using simulated engine exhaust gases. The performance evaluations consist of T50, T90, WGS reaction, and OSC. In addition to BFR experiments, the deactivation mechanisms of thermally-aged and poisoned TWCs are identified and elucidated using surface characterization techniques, such as Brunauer-Emmett-Teller (BET), electron probe microanalysis (EPMA), X-ray diffraction (XRD), and inductively coupled plasma (ICP) analysis.

For the NA-aged TWC sample the T50 and T90 of CO and C_3H_6 increase compared to the fresh TWC sample, indicating the performance degradation mainly due to thermal aging. On the other hand, the T50 and T90 of NO exhibit no definite trend, possibly as a result of the complexity of the reduction process of NO. The degradation in the performance of the NA-aged TWC sample is mainly due to the reduction of the OSC and WGS reaction as a result of a loss in BET surface area and sintering of Pd particles. Only a trace amount of Zn and P, mainly from the consumption of the engine lubricant additive during the accelerated engine aging, is detected by ICP-OES and EPMA analyses. Such

results indicate that the NA-aged TWC can be used as a baseline to which the impact of lubricant additives such as ZDDP, IL, and mixed IL and ZDDP lubricant additives on the performance of Pd-based TWCs can be investigated.

The present study has revealed the following points regarding the degradation in the performance of Pd-based TWCs due to lubricant additives.

- The performance of the TWC is degraded further by IL, ZDDP1, ZDDP2, IL+ZDDP2, and IL+ZDDP2 lubricant additives as compared to that of NA-aged TWC sample, indicating additional impact of poisoning from lubricant additives.
- T50 for CO, C_3H_6, and C_3H_8 of IL-, ZDDP1-, ZDDP2-, IL+ZDDP1-, and IL+ZDDP2-aged TWC samples is higher than that of the NA-aged TWC sample. Similarly, all lubricant additive-aged TWC samples have higher T90 than NA-aged TWC sample for NO, CO, C_3H_6, and C_3H_8.
- T50 for NO of the ZDDP2- and IL+ZDDP2-aged TWC sample is 20°C and 23°C lower than that of NA-aged TWC sample, respectively. Since the NO conversion is very sensitive to the reactivity of the reductants such as H_2, CO, and C_3H_6, especially in the temperature range between 150°C and 300°C, it is difficult to assess the effects of lubricant additives on the performance of TWC based on the light-off behavior of NO conversion.
- The degradation in the OSC performance is more severe for IL-, ZDDP2-, and IL+ZDDP2-aged TWC samples, indicating that P, S, and Zn poisoning from lubricant additives is also significant in addition to thermal aging. On the other hand, the ZDDP1- and IL+ZDDP1-aged TWC sample is the least affected when compared to the NA-aged TWC sample.
- Significant WGS reactivity losses for the IL-, ZDDP2-, and IL+ZDDP2-aged samples above 300°C are mainly due to poisoning from lubricant additives. The WGS reaction for the ZDDP1- and IL+ZDDP1-aged TWC

samples is less degraded than that for ZDDP2- and IL+ZDDP2-aged TWC samples at all temperatures. As in the case of OSC performance, the impact on the WGS reaction of the TWC of the mixed lubricant additives is similar to that of single ZDDP lubricant additives.

- The impact of a mixed additive of IL and ZDDP (IL+ZDDP1 and IL+ZDDP2) on TWC performance is comparable to that of a single ZDDP (ZDDP1 and ZDDP2).
- Since the amount of S, Zn, and P in ZDDP1 is lower than in ZDDP2, the degradation in the TWC performance due to ZDDP1 is less severe than that ZDDP2, as reflected from the BFR evaluation results.
- Similarly, the degradation in the TWC performance by IL+ZDDP1 is less than IL+ZDDP2.
- TWC sample exposed to lubricant additives has lower BET surface area than NA-aged TWC sample as a result of thermal aging and poisoning.
- NA-aged TWC sample and all TWC samples exposed to lubricant additives have similar pore sizes, which suggests that no blocking or occluding of the pores by the compounds formed from the components of the lubricant additives such as P, Zn, S, etc.
- EPMA micrographs of Zn indicate the presence of a thin Zn layer on the washcoat surface and slightly Zn penetration deep inside the washcoat for ZDDP1- and ZDDP2-aged TWC samples. On the other hand, since IL lubricant additive does not contain Zn only a trace amount of Zn is observed on the washcoat surface of IL, IL+ZDDP1- and IL+ZDDP2-aged TWC samples. ICP-OES results show that no significant difference in the amount of Zn across all TWC samples exposed to lubricant additives since the amount of Zn detected is near the detection limit of the instrument. However, ICP-OES and EPMA results clearly indicate that all

TWC samples exposed to lubricant additives captured low levels of Zn during accelerated engine aging.

- EPMA micrographs of P show that for all TWC samples exposed to lubricant additives, the presence of P is mainly observed on the washcoat surface with some penetration into the washcoat. The P overlayer for the ZDDP2-aged TWC sample is more contiguous and contains more P, whereas, for the IL+ZDDP1-aged TWC sample, the P overlayer is less discernible and similar to that of NA-aged TWC sample. EPMA results are further confirmed by those from ICP-OES analysis, which shows the concentration of P is highest (1.74 wt%) in IL+ZDDP2-aged TWC sample and lowest (0.71 wt%) in IL+ZDDP1-aged TWC sample. Even though the dose of P is kept constant throughout the accelerated poisoning experiment, the difference in the amount of P obtained from EPMA and ICP-OES is possibly due to the difference in the phosphorus volatility of ZDDP1 and ZDDP2. The presence of P on the washcoat surface acts as a barrier preventing the diffusion of gaseous species to the Pd active sites, and this is one of the main deactivation mechanisms.
- Powder XRD results indicate that P, primary in the form of $CePO_4$, is found to be present on the washcoat of IL-, ZDDP2-, and IL+ZDDP2-aged TWC samples, but not on the NA-aged TWC sample. The presence of $CePO_4$ is believed to be the major contributor to the decrease in OSC and WGS reaction in IL, ZDDP2, and IL+ZDDP2 TWC samples as compared to the NA-aged TWC sample. On the other hand, the presence of $CePO_4$ is less in ZDDP1- and IL+ZDDP1-aged TWC samples, resulting in less degradation of OSC performance. No other peaks associated with $Zn_2P_2O_7$ and $AlPO_4$, are observed in all TWC samples exposed to lubricant additives.

The mathematical model is suitable for simulating the performance of the fresh TWC sample by adjusting the kinetic parameters in the global reactions. In addition, the performance degradation of the TWCs due to thermal aging (sintering) and lubricant additives (poisoning) can be represented as the reduction of PGM active sites, which in turn can be modeled as a decrease in the PGM loading. The NO, CO, C_3H_6, and C_3H_8 conversion results obtained from the model are quite similar to those obtained from the BFR results for fresh and engine-aged TWC samples, whereas the formation of NH_3 and N_2O can be predicted only qualitatively, but not quantitatively. The model can be further improved by including additional global reactions such as an oxygen storage mechanism, C_3H_8 steam reforming reaction, etc.

In conclusion, the impact of mixed lubricant additives containing both ZDDP and IL such as IL+ZDDP1 and IL+ZDDP2 on the performance of Pd-based TWCs have been found to be not significantly different from that of single ZDDP lubricant additives such as ZDDP1 and ZDDP2. Consequently, the mixed lubricant additives with [P8888][DEHP] as the IL component with the low friction coefficient and wear volume are certainly viable candidates for lubricant additives for vehicle applications.

LIST OF REFERENCES

[1] O. US EPA, OAR, “Fuel economy,” *Nature*, vol. 103, no. 2585. p. 213, 1919.
[2] “Spare The Air: Health Effects of Air Pollution.” [Online]. Available: http://www.sparetheair.com/health.cfm. [Accessed: 14-Apr-2020].
[3] N. E. Health, “Health Effects Carbon Monoxide Poisoning Exposure and Risk - CDC Tracking Network,” *CDC*, 2016. [Online]. Available: https://ephtracking.cdc.gov/showCoRisk.action. [Accessed: 14-Apr-2020].
[4] Phys Org, “NO_x gases in diesel car fumes: Why are they so dangerous?,” 2015. [Online]. Available: https://phys.org/news/2015-09-nox-gases-diesel-car-fumes.html. [Accessed: 14-Apr-2020].
[5] “Emission Standards: USA: Cars and Light-Duty Trucks—Tier 1.” [Online]. Available: https://www.dieselnet.com/standards/us/ld_t1.php. [Accessed: 01-Nov-2018].
[6] “Emission Standards: USA: Cars and Light-Duty Trucks—Tier 2.” [Online]. Available: https://www.dieselnet.com/standards/us/ld_t2.php. [Accessed: 01-Nov-2018].
[7] “Emission Standards: USA: Cars and Light-Duty Trucks—Tier 3.” [Online]. Available: https://www.dieselnet.com/standards/us/ld_t3.php. [Accessed: 01-Nov-2018].
[8] NHTSA, “Final Regulatory Impact Analysis for Corporate Average Fuel Economy for MY 2017-MY 2025 Passenger Cars and Light Trucks,” no. August, pp. 1–1178, 2012.
[9] “Inventory of U.S. Greenhouse Gas Emissions and Sinks | Greenhouse Gas (GHG) Emissions | US EPA,” 2019. [Online]. Available: https://www.epa.gov/ghgemissions/inventory-us-greenhouse-gas-emissions-and-sinks. [Accessed: 14-Apr-2020].
[10] Amber Broch and S. Kent Hoekman, “Effects of Organometallic Additives on Gasoline Vehicles: Analysis of Existing Literature,” 2015.
[11] “Umicore - Three-way catalyst (TWC).” [Online]. Available: https://ac.umicore.com/en/technologies/three-way-catalyst/. [Accessed: 14-Apr-2020].
[12] J. Kašpar, P. Fornasiero, and N. Hickey, “Automotive catalytic converters: current status and some perspectives,” *Catal. today*, vol. 77, no. 4, pp. 419–449, 2003.
[13] J. Kašpar, P. Fornasiero, and M. Graziani, “Use of CeO_2-based oxides in the three-way catalysis,” *Catal. Today*, vol. 50, no. 2, pp. 285–298, 1999.
[14] J. Wang, H. Chen, Z. Hu, M. Yao, and Y. Li, “A review on the Pd-based three-way catalyst,” *Catal. Rev. - Sci. Eng.*, vol. 57, no. 1, pp. 79–144, 2015.

[15] M. SHELEF, G. W. GRAHAM, and R. W. McCABE, “Ceria and other oxygen storage components in automotive catalysts,” in *Catalysis by Ceria and related Materials*, World Scientific, 2002, pp. 343–375.
[16] M. Ozawa and M. Kimura, “Effect of cerium addition on the thermal stability of gamma alumina support,” *J. Mater. Sci. Lett.*, vol. 9, no. 3, pp. 291–293, 1990.
[17] P. Burtin, J.-P. Brunelle, M. Pijolat, and M. Soustelle, “Influence of surface area and additives on the thermal stability of transition alumina catalyst supports. I: Kinetic data,” *Appl. Catal.*, vol. 34, pp. 225–238, 1987.
[18] T. Yamamoto, T. Hatsui, T. Matsuyama, T. Tanaka, and T. Funabiki, “Structures and acid− base properties of La/Al_2O_3 role of La addition to enhance thermal stability of γ-Al_2O_3,” *Chem. Mater.*, vol. 15, no. 25, pp. 4830–4840, 2003.
[19] J. H. Kwak, J. Hu, A. Lukaski, D. H. Kim, J. Szanyi, and C. H. F. Peden, “Role of pentacoordinated Al^{3+} ions in the high temperature phase transformation of γ-Al_2O_3,” *J. Phys. Chem. C*, vol. 112, no. 25, pp. 9486–9492, 2008.
[20] H. S. Gandhi, Gw. Graham, and R. McCabe, “Automotive exhaust catalysis,” *J. Catal.*, vol. 216, no. 1–2, pp. 433–442, 2003.
[21] C.-Z. Wan and J. C. Dettling, “High temperature catalyst compositions for internal combustion engine.” U.S. Patent 4,624,940, 25-Nov-1986.
[22] C. Z. Wan and J. C. Dettling, “Effective Rhodium Utilization in Automotive Exhaust Catalysts,” SAE Technical Paper, 1986.
[23] G. B. Fisher, J. R. Theis, M. V Casarella, and S. T. Mahan, “The role of ceria in automotive exhaust catalysis and OBD-II catalyst monitoring,” SAE Technical Paper, 1993.
[24] A. Kato, H. Yamashita, H. Kawagoshi, and S. Matsuda, “Preparation of Larnthanum β-Alumina with High Surface Area by Coprecipitation,” *J. Am. Ceram. Soc.*, vol. 70, no. 7, pp. C–157, 1987.
[25] I. I. M. Tijburg, J. W. Geus, and H. W. Zandbergen, “Application of lanthanum to pseudo-boehmite and γ-Al_2O_3,” *J. Mater. Sci.*, vol. 26, no. 23, pp. 6479–6486, 1991.
[26] M. Machida, K. Eguchi, and H. Arai, “Preparation and characterization of large surface area BaO· $6Al_2O_3$,” *Bull. Chem. Soc. Jpn.*, vol. 61, no. 10, pp. 3659–3665, 1988.
[27] B. Beguin, E. Garbowski, and M. Primet, “Stabilization of alumina toward thermal sintering by silicon addition,” *J. Catal.*, vol. 127, no. 2, pp. 595–604, 1991.

[28] P. Granger, J. F. Lamonier, N. Sergent, A. Aboukais, L. Leclercq, and G. Leclercq, “Investigation of the intrinsic activity of $Zr_xCe_{1-x}O_2$ mixed oxides in the CO+ NO reactions: influence of Pd incorporation,” *Top. Catal.*, vol. 16, no. 1–4, pp. 89–94, 2001.
[29] R. M. Heck, R. K. Farrauto, and S. Gulati, “‘Catalytic Air Pollution Control: Commercial Technology,’” *Platin. Met. Rev*, vol. 54, no. 3, pp. 180–183, 2010.
[30] Y.-F. Y. Yao, “Oxidation of alkanes over noble metal catalysts,” *Ind. Eng. Chem. Prod. Res. Dev.*, vol. 19, no. 3, pp. 293–298, 1980.
[31] A. M. Gololobov *et al.*, “Platinum nanoparticle size effect on specific catalytic activity in n-alkane deep oxidation: Dependence on the chain length of the paraffin,” *Kinet. Catal.*, vol. 50, no. 6, p. 830, 2009.
[32] H. S. Gandhi and M. Shelef, “Effects of sulphur on noble metal automotive catalysts,” *Appl. Catal.*, vol. 77, no. 2, pp. 175–186, 1991.
[33] H. S. H. Gandhi *et al.*, “Affinity of lead for noble metals on different supports,” *Surf.*, vol. 6, no. 4, pp. 149–161, 1984.
[34] Y. Yu Yao, “The Oxidation of CO and Hydrocarbons over Noble Metal Catalysts,” *J. Catal.*, vol. 87, pp. 152–162, 1984.
[35] C. F. Cullis and B. M. Willatt, “Oxidation of methane over supported precious metal catalysts,” *J. Catal.*, vol. 83, no. 2, pp. 267–285, 1983.
[36] J. T. Kummer, “Oxidation of CO and C_2H_4 by base metal catalysts prepared on honeycomb supports,” ACS Publications, 1975.
[37] A. Russell and W. S. Epling, “Diesel oxidation catalysts,” *Catal. Rev.*, vol. 53, no. 4, pp. 337–423, 2011.
[38] T. Yamada, K. Kayano, and M. Funabiki, “The effectiveness of Pd for converting hydrocarbons in TWC catalysts,” SAE Technical Paper, 1993.
[39] J. E. Kummer and J. McEvoy, “Catalysts for the Control of Automotive Pollutants,” *ACS Adv. Chem. Ser. No. 143*, 1975.
[40] J. G. E. Cohn, “Method of removing nitrogen oxides from gases.” U.S. Patent, 21-Jan-1964.
[41] A. Somayaji, “A study of the antiwear behavior and oxidation stability of fluorinated zinc dialkyl dithio phosphate in the presence of antioxidants,” The University of Texas at Arlington, 2008.
[42] K. Eriksson, “Fatty Amines as Friction Modifiers in Engine Oils Correlating Adsorbed Amount to Friction and Wear Performance,” CHALMERS UNIVERSITY OF TECHNOLOGY, 2014.
[43] K. K. Swami *et al.*, “Additive-additive interactions: The search for synergistic antioxidant—antiwear phosphorodithioate compositions,” *Lubr. Sci.*, vol. 14, no. 4, pp. 385–392, 2002.
[44] H. Spikes, “The history and mechanisms of ZDDP,” *Tribol. Lett.*, 2004.

[45] K. K. Swami *et al.*, “Additive-additive interactions: The search for synergistic antioxidant-antiwear phosphorodithioate compositions,” *Lubr. Sci.*, vol. 14, no. 4, pp. 385–392, 2002.
[46] T. Welton, “Room-temperature ionic liquids. Solvents for synthesis and catalysis,” *Chem. Rev.*, vol. 99, pp. 2071–2083, 1999.
[47] M. Earle and K. Seddon, “Ionic liquids. Green solvents for the future,” *Pure Appl. Chem.*, vol. 72, pp. 1391–1398, 2000.
[48] H. Olivier, “Recent developments in the use of non-aqueous ionic liquids for two-phase catalysis,” *J. Mol. Catal. A Chem.*, vol. 146, no. 1–2, pp. 285–289, 1999.
[49] A. E. Jiménez, M. D. Bermúdez, and A. Jim, “Imidazolium ionic liquids as additives of the synthetic ester propylene glycol dioleate in aluminium-steel lubrication,” *Wear*, vol. 265, no. 5–6, pp. 787–798, 2008.
[50] M. Yao, Y. Liang, Y. Xia, and F. Zhou, “Bisimidazolium ionic liquids as the high-performance antiwear additives in poly(ethylene glycol) for steel-steel contacts,” *ACS Appl. Mater. Interfaces*, vol. 1, no. 2, pp. 467–471, 2009.
[51] M. Cai, Y. Liang, M. Yao, Y. Xia, F. Zhou, and W. Liu, “Imidazolium ionic liquids as antiwear and antioxidant additive in poly(ethylene glycol) for steel/steel contacts,” *ACS Appl. Mater. Interfaces*, vol. 2, no. 3, pp. 870–876, 2010.
[52] A. Libardi, S. R. Schmid, M. Sen, and W. Schneider, “Evaluation of ionic fluids as lubricants in manufacturing,” *J. Manuf. Process.*, vol. 15, no. 4, pp. 414–418, 2013.
[53] F. U. Shah, S. Glavatskih, D. R. MacFarlane, A. Somers, M. Forsyth, and O. N. Antzutkin, “Novel halogen-free chelated orthoborate–phosphonium ionic liquids: synthesis and tribophysical properties,” *Phys. Chem. Chem. Phys.*, vol. 13, no. 28, pp. 12865–12873, 2011.
[54] A. Hernández Battez, M. Bartolomé, D. Blanco, J. L. Viesca, A. Fernández-González, and R. González, “Phosphonium cation-based ionic liquids as neat lubricants: Physicochemical and tribological performance,” *Tribol. Int.*, vol. 95, pp. 118–131, 2016.
[55] W. C. Barnhill *et al.*, “Phosphonium-Organophosphate Ionic Liquids as Lubricant Additives: Effects of Cation Structure on Physicochemical and Tribological Characteristics,” *ACS Appl. Mater. Interfaces*, vol. 6, p. 22585−22593, 2014.
[56] J. Qu *et al.*, “Antiwear performance and mechanism of an oil-miscible ionic liquid as a lubricant additive,” *ACS Appl. Mater. Interfaces*, vol. 4, no. 2, pp. 997–1002, 2012.
[57] J. Qu *et al.*, “Comparison of an oil-miscible ionic liquid and ZDDP as a lubricant anti-wear additive,” *Tribol. Int.*, vol. 71, pp. 88–97, 2014.

[58] B. Yu *et al.*, “Oil-miscible and non-corrosive phosphonium-based ionic liquids as candidate lubricant additives,” *Wear*, vol. 289, pp. 58–64, 2012.
[59] Y. Zhou, J. Dyck, T. W. Graham, H. Luo, D. N. Leonard, and J. Qu, “Ionic liquids composed of phosphonium cations and organophosphate, carboxylate, and sulfonate anions as lubricant antiwear additives,” *Langmuir*, vol. 30, no. 44, pp. 13301–13311, 2014.
[60] I. Otero, E. López, and M. Reichelt, “Ionic liquids based on phosphonium cations as neat lubricants or lubricant additives for a steel/steel contact,” *ACS Appl. Mater. Interfaces*, vol. 6, no. 15, pp. 13115–13128, 2014.
[61] A. E. Somers, B. Khemchandani, P. C. Howlett, J. Sun, D. R. Macfarlane, and M. Forsyth, “Ionic liquids as antiwear additives in base oils: Influence of structure on miscibility and antiwear performance for steel on aluminum,” *ACS Appl. Mater. Interfaces*, vol. 5, no. 22, pp. 11544–11553, 2013.
[62] J. Qu, H. Luo, T. Toops, B. West, P. Blau, and S. Dai, “Ionic Liquids as Multi-Functional Lubricant Additives to Enhance Engine Efficiency (final report NFE-12-03876),” 2016.
[63] J. Qu *et al.*, “Synergistic effects between phosphonium-alkylphosphate ionic liquids and zinc dialkyldithiophosphate (ZDDP) as lubricant additives,” *Adv. Mater.*, vol. 27, no. 32, pp. 4767–4774, 2015.
[64] J. Qu, “Ionic Liquids as Next Generation Anti-wear Additives – From Molecular Design to Engine Dynamometer Testing,” in *Research sponsored by the Fuels and Lubricants Program, Vehicle Technologies Office, Office of Energy Efficiency and Renewable Energy, U.S. Department of Energy.*
[65] W. C. Barnhill, “Tribological Testing and Analysis of Ionic Liquids as Candidate Anti-Wear Additives for Next- Generation Engine Lubricants,” 2016.
[66] H. Muraki, H. Shinjoh, H. Sobukawa, K. Yokota, and Y. Fujitani, “Palladium-lanthanum catalysts for automotive emission control,” *Ind. Eng. Chem. Prod. Res. Dev.*, vol. 25, no. 2, pp. 202–208, 1986.
[67] H. Muraki, K. Yokota, and Y. Fujitani, “Nitric oxide reduction performance of automotive palladium catalysts,” *Appl. Catal.*, vol. 48, no. 1, pp. 93–105, 1989.
[68] H. Muraki, H. Shinjoh, and Y. Fujitani, “Effect of lanthanum on the no reduction over palladium catalysts,” *Appl. Catal.*, vol. 22, no. 2, pp. 325–335, 1986.
[69] H. Shinjoh, “Rare earth metals for automotive exhaust catalysts,” *J. Alloys Compd.*, vol. 408, pp. 1061–1064, 2006.

[70] A. D. Logan and G. W. Graham, “NO chemisorption on Pd (100) with ultra-thin overlayers of oxidized La and Al,” *Surf. Sci. Lett.*, vol. 277, no. 1–2, pp. L47–L51, 1992.
[71] M. Skoglundh, H. Johansson, L. Löwendahl, K. Jansson, L. Dahl, and B. Hirschauer, “Cobalt-promoted palladium as a three-way catalyst,” *Appl. Catal. B Environ.*, vol. 7, no. 3–4, pp. 299–319, 1996.
[72] J. Noh, O.-B. Yang, D. H. Kim, and S. I. Woo, “Characteristics of the Pd-only three-way catalysts prepared by sol–gel method,” *Catal. today*, vol. 53, no. 4, pp. 575–582, 1999.
[73] K. M. Adams and H. S. Gandhi, “Palladium-tungsten catalysts for automotive exhaust treatment,” *Ind. Eng. Chem. Prod. Res. Dev.*, vol. 22, no. 2, pp. 207–212, 1983.
[74] C. Neyertz and M. Volpe, “Preparation of binary palladium-vanadium supported catalysts from metal acetylacetonates,” *Colloids Surfaces A Physicochem. Eng. Asp.*, vol. 136, no. 1–2, pp. 63–69, 1998.
[75] D. H. Kim, S. I. Woo, J. Noh, and O.-B. Yang, “Synergistic effect of vanadium and zirconium oxides in the Pd-only three-way catalysts synthesized by sol–gel method,” *Appl. Catal. A Gen.*, vol. 207, no. 1–2, pp. 69–77, 2001.
[76] I. V Yentekakis, R. M. Lambert, M. S. Tikhov, M. Konsolakis, and V. Kiousis, “Promotion by sodium in emission control catalysis: a kinetic and spectroscopic study of the Pd-catalyzed reduction of NO by propene,” *J. Catal.*, vol. 176, no. 1, pp. 82–92, 1998.
[77] N. Macleod, J. Isaac, and R. M. Lambert, “Sodium promotion of Pd/γ-Al_2O_3 catalysts operated under simulated ‘three-way’ conditions,” *J. Catal.*, vol. 198, no. 1, pp. 128–135, 2001.
[78] T. Sekiba, S. Kimura, H. Yamamoto, and A. Okada, “Development of automotive palladium three-way catalysts,” *Catal. today*, vol. 22, no. 1, pp. 113–126, 1994.
[79] M. Fernández-Garcıa *et al.*, “New Pd/$Ce_xZr_{1-x}O_2$/Al_2O_3 three-way catalysts prepared by microemulsion: Part 1. Characterization and catalytic behavior for CO oxidation,” *Appl. Catal. B Environ.*, vol. 31, no. 1, pp. 39–50, 2001.
[80] A. Martınez-Arias *et al.*, “New Pd/$CexZr_{1-x}O_2$/Al_2O_3 three-way catalysts prepared by microemulsion: Part 2. In situ analysis of CO oxidation and NO reduction under stoichiometric CO+ NO+ O_2,” *Appl. Catal. B Environ.*, vol. 31, no. 1, pp. 51–60, 2001.
[81] J. Guo, D. Wu, L. Zhang, M. Gong, M. Zhao, and Y. Chen, “Influence of support,” *J. Alloys Compd.*, vol. 460, no. 1–2, pp. 485–490, 2008.

[82] X. Wu *et al.*, “Structure and oxygen storage capacity of Pr/Nd doped CeO_2–ZrO_2 mixed oxides,” *Solid state Sci.*, vol. 9, no. 7, pp. 636–643, 2007.
[83] J. Mikulova, S. Rossignol, F. Gérard, D. Mesnard, C. Kappenstein, and D. Duprez, “Properties of cerium–zirconium mixed oxides partially substituted by neodymium: comparison with Zr–Ce–Pr–O ternary oxides,” *J. Solid State Chem.*, vol. 179, no. 8, pp. 2511–2520, 2006.
[84] Q. Wang, G. Li, B. Zhao, and R. Zhou, “Investigation on properties of a novel ceria–zirconia–praseodymia solid solution and its application in Pd-only three-way catalyst for gasoline engine emission control,” *Fuel*, vol. 90, no. 10, pp. 3047–3055, 2011.
[85] Q. Wang, G. Li, B. Zhao, and R. Zhou, “The effect of Nd on the properties of ceria–zirconia solid solution and the catalytic performance of its supported Pd-only three-way catalyst for gasoline engine exhaust reduction,” *J. Hazard. Mater.*, vol. 189, no. 1–2, pp. 150–157, 2011.
[86] Q. Wang, G. Li, B. Zhao, and R. Zhou, “The effect of rare earth modification on ceria–zirconia solid solution and its application in Pd-only three-way catalyst,” *J. Mol. Catal. A Chem.*, vol. 339, no. 1–2, pp. 52–60, 2011.
[87] M. Yamamoto and H. Tanaka, “Influence of support materials on durability of palladium in three-way catalyst,” *SAE Trans.*, pp. 237–244, 1998.
[88] P. Vidmar, P. Fornasiero, J. Kašpar, G. Gubitosa, and M. Graziani, “Effects of trivalent dopants on the redox properties of $Ce_{0.6}Zr_{0.4}O_2$ mixed oxide,” *J. Catal.*, vol. 171, no. 1, pp. 160–168, Oct. 1997.
[89] G. L. Markaryan *et al.*, “Red–ox properties and phase composition of CeO_2–ZrO_2 and Y_2O_3–CeO_2–ZrO_2 solid solutions,” *Colloids Surfaces A Physicochem. Eng. Asp.*, vol. 151, no. 3, pp. 435–447, 1999.
[90] H. Yucai, “Hydrothermal Synthesis of Nano Ce–Zr–Y Oxide Solid Solution for Automotive Three-Way Catalyst,” *J. Am. Ceram. Soc.*, vol. 89, no. 9, pp. 2949–2951, 2006.
[91] G. Wang, M. Meng, Y. Zha, and T. Ding, “High-temperature close coupled catalysts Pd/Ce–Zr–M/Al_2O_3 (M = Y, Ca or Ba) used for the total oxidation of propane,” *Fuel*, vol. 89, no. 9, pp. 2244–2251, 2010.
[92] G. Wang, R. You, and M. Meng, “An optimized highly active and thermo-stable oxidation catalyst Pd/Ce–Zr–Y/Al_2O_3 calcined at superhigh temperature and used for C_3H_8 total oxidation,” *Fuel*, vol. 103, no. C, pp. 799–804, 2013.

[93] G. Li, Q. Wang, B. Zhao, M. Shen, and R. Zhou, “Effect of iron doping into CeO_2–ZrO_2 on the properties and catalytic behaviour of Pd-only three-way catalyst for automotive emission control,” *J. Hazard. Mater.*, vol. 186, no. 1, pp. 911–920, 2011.
[94] G. Li, B. Zhao, Q. Wang, and R. Zhou, “The effect of Ni on the structure and catalytic behavior of model Pd/$Ce_{0.67}Zr_{0.33}O_2$ three-way catalyst before and after aging,” *Appl. Catal. B, Environ.*, vol. 97, no. 1–2, pp. 41–48, 2010.
[95] G. Li, Q. Wang, B. Zhao, and R. Zhou, “A new insight into the role of transition metals doping with CeO_2–ZrO_2 and its application in Pd-only three-way catalysts for automotive emission control,” *Fuel*, vol. 92, no. 1, pp. 360–368, 2012.
[96] Y. Guo, G. Lu, Z. Zhang, S. Zhang, Y. Qi, and Y. Liu, “Preparation of $Ce_xZr_{1-x}O_2$ (x=0.75, 0.62) solid solution and its application in Pd-only three-way catalysts,” *Catal. Today*, vol. 126, no. 3–4, pp. 296–302, 2007.
[97] Y. Yao, R. Fang, Z. Shi, M. Gong, and Y. Chen, “The Effect of La_2O_3 on Pd Close-Coupled Catalysts,” *Chinese J. Catal.*, vol. 32, no. 3, pp. 589–594, 2011.
[98] A. B. Hungría *et al.*, “The effect of Ni in Pd–Ni/(Ce,Zr)O_x/Al_2O_3 catalysts used for stoichiometric CO and NO elimination. Part 1: Nanoscopic characterization of the catalysts,” *J. Catal.*, vol. 235, no. 2, pp. 251–261, 2005.
[99] A. B. Hungría, M. Fernández-García, J. A. Anderson, and A. Martínez-Arias, “The effect of Ni in Pd–Ni/(Ce,Zr)O_x/Al_2O_3 catalysts used for stoichiometric CO and NO elimination. Part 2: Catalytic activity and in situ spectroscopic studies,” *J. Catal.*, vol. 235, no. 2, pp. 262–271, 2005.
[100] A. B. Hungría *et al.*, “Effects of Copper on the Catalytic Properties of Bimetallic Pd–Cu/(Ce,Zr)O_x/Al_2O_3 and Pd–Cu/(Ce,Zr)O_x Catalysts for CO and NO Elimination,” *J. Catal.*, vol. 206, no. 2, pp. 281–294, 2002.
[101] A. Iglesias-Juez, A. B. Hungría, A. Martínez-Arias, J. A. Anderson, and M. Fernández-García, “Pd-based (Ce,Zr)O_x-supported catalysts: Promoting effect of base metals (Cr, Cu, Ni) in CO and NO elimination,” *Catal. Today*, vol. 143, no. 3–4, pp. 195–202, 2009.
[102] J. A. Moulijn, A. E. van Diepen, and F. Kapteijn, “Catalyst deactivation: is it predictable?: What to do?,” *Appl. Catal. A, Gen.*, vol. 212, no. 1, pp. 3–16, 2001.
[103] J. J. Chen and E. Ruckenstein, “Sintering of palladium on alumina model catalyst in a hydrogen atmosphere,” *J. Catal.*, vol. 69, no. 2, pp. 254–273, 1981.

[104] Q. Xu, K. C. Kharas, B. J. Croley, and A. K. Datye, “The Sintering of Supported Pd Automotive Catalysts,” *ChemCatChem*, vol. 3, no. 6, pp. 1004–1014, 2011.
[105] X. Chen, Y. Cheng, C. Y. Seo, J. W. Schwank, and R. W. McCabe, “Aging, re-dispersion, and catalytic oxidation characteristics of model Pd/Al_2O_3 automotive three-way catalysts,” *Appl. Catal. B Environ.*, vol. 163, pp. 499–509, 2015.
[106] H. Birgersson, M. Boutonnet, S. Järås, and L. Eriksson, “Deactivation and regeneration of spent three-way automotive exhaust gas catalysts (TWC),” *Top. Catal.*, vol. 30–31, no. July, pp. 433–438, 2004.
[107] S. B. Kang, H. J. Kwon, I.-S. S. Nam, Y. Il Song, and S. H. Oh, “Activity Function for Describing Alteration of Three-Way Catalyst Performance over Palladium-Only Three-Way Catalysts by Catalyst Mileage,” *Ind. Eng. Chem. Res.*, vol. 50, no. 9, pp. 5499–5509, 2011.
[108] G. W. Graham, H. W. Jen, W. Chun, and R. W. McCabe, “High-temperature-aging-induced encapsulation of metal particles by support materials: Comparative results for Pt, Pd, and Rh on cerium-zirconium mixed oxides,” *J. Catal.*, vol. 182, no. 1, pp. 228–233, 1999.
[109] G. W. Graham, A. E. O’Neill, D. Uy, W. H. Weber, H. Sun, and X. Q. Pan, “Observation of strained PdO in an aged Pd/ceria-zirconia catalyst,” *Catal. Letters*, vol. 79, no. 1–4, pp. 99–105, 2002.
[110] G. W. Graham, A. E. O’Neill, and A. E. Chen, “Pd encapsulation in automotive exhaust-gas catalysts,” *Appl. Catal. A Gen.*, vol. 252, no. 2, pp. 437–445, 2003.
[111] I. Heo *et al.*, “The alteration of the performance of field-aged Pd-based TWCs towards CO and C_3H_6 oxidation,” *Appl. Catal. B Environ.*, vol. 92, no. 1–2, pp. 114–125, 2009.
[112] U. Lassi *et al.*, “Effect of ageing atmosphere on the deactivation of Pd/Rh automotive exhaust gas catalysts: catalytic activity and XPS studies,” *Appl. Catal. A, Gen.*, vol. 263, no. 2, pp. 241–248, 2004.
[113] W. J. Koehl *et al.*, “Effects of gasoline sulfur level on exhaust mass and speciated emissions: The question of linearity - Auto/Oil air quality Improvement Program,” *SAE Tech. Pap.*, 1993.
[114] D. D. Beck, J. W. Sommers, and C. L. DiMaggio, “Impact of sulfur on model palladium-only catalysts under simulated three-way operation,” *Appl. Catal. B, Environ.*, vol. 3, no. 2–3, pp. 205–227, 1994.
[115] D. R. Monroe, M. H. Krueger, D. D. Beck, and M. J. D. Aniello, “THE EFFECT OF SULFUR ON THREE-WAY CATALYSTS,” *Catal. Automot. Pollut. Control II*, pp. 593–616, 1991.

[116] T.-C. C. Yu and H. Shaw, “The effect of sulfur poisoning on methane oxidation over palladium supported on γ-alumina catalysts,” *Appl. Catal. B Environ.*, vol. 18, no. 1–2, pp. 105–114, 1998.
[117] D. D. Beck and J. W. Sommers, “Impact of sulfur on three-way catalysts: Comparison of commercially produced Pd and Pt-Rh monoliths,” in *Studies in Surface Science and Catalysis*, vol. 96, Elsevier Science & Technology, 1995, pp. 721–748.
[118] “The Impact of Gasoline Fuel Sulfur on Catalytic,” *Manuf. Emiss. Control. Assoc.*, no. June, pp. 1–35, 2013.
[119] D. D. Beck, “Impact of sulfur on three-way automotive catalyst performance and catalyst diagnostics,” *Catal. Deactiv.*, pp. 21–38, 1997.
[120] W. J. Koehl, J. D. Benson, V. Burns, R. A. Gorse, A. M. Hochhauser, and R. M. Reuter, “Effects of Gasoline Composition and Properties on Vehicle Emissions: A Review of Prior Studies - Auto/Oil Air Quality Improvement Research Program.” SAE International , 1991.
[121] P. Bazin, O. Saur, J. C. Lavalley, G. Blanchard, V. Visciglio, and O. Touret, “Influence of platinum on ceria sulfation,” *Appl. Catal. B Environ.*, vol. 13, no. 3–4, pp. 265–274, 1997.
[122] J. A. Rodriguez *et al.*, “Physical and chemical properties of $Ce_{1-x}Zr_xO_2$ nanoparticles and $Ce_{1-x}ZrxO_2$ (1 1 1) surfaces: Synchrotron-based studies,” *Journal of Molecular Catalysis A: Chemical*, vol. 228, no. 1-2 SPEC. ISS. pp. 11–19, 2005.
[123] J. Twu, C. J. Chuang, K. I. Chang, C. H. Yang, and K. H. Chen, “Raman spectroscopic studies on the sulfation of cerium oxide,” *Appl. Catal. B Environ.*, vol. 12, no. 4, pp. 309–324, 1997.
[124] M. Waqif, P. Bazin, O. Saur, J. C. Lavalley, G. Blanchard, and O. Touret, “Study of ceria sulfation,” *Appl. Catal. B Environ.*, vol. 11, no. 2, pp. 193–205, 1997.
[125] J. Rodriguez, T. Jirsak, A. Freitag, J. Hanson, J. Larese, and S. Chaturvedi, “Interaction of SO_2 with CeO_2 and Cu/CeO_2 catalysts: photoemission, XANES and TPD studies,” *Catal. Letters*, vol. 62, no. 2–4, pp. 113–119, 1999.
[126] M. Boaro, C. De Leitenburg, G. Dolcetti, A. Trovarelli, and M. Graziani, “Oxygen storage behavior of ceria-zirconia-based catalysts in the presence of SO_2,” *Top. Catal.*, vol. 16–17, no. 1–4, pp. 299–306, 2001.
[127] W. B. Williamson, J. Perry, R. L. Goss, H. S. Gandhi, and R. E. Beason, “Catalyst deactivation due to glaze formation from oil-derived phosphorus and zinc,” SAE Technical Paper, 1984.

[128] H. S. Gandhi, W. B. Wlliamson, and J. L. Bomback, “Deactivation of three-way and oxidation catalyst dual bed emission control systems: catalyst post mortem analyses from methanol-fueled vehicles,” *Appl. Catal.*, vol. 3, no. 1, pp. 79–88, 1982.
[129] M. J. Rokosz *et al.*, “Characterization of phosphorus-poisoned automotive exhaust catalysts,” *Appl. Catal. B Environ.*, vol. 33, no. 3, pp. 205–215, 2001.
[130] L. Xu *et al.*, “Cerium phosphate in automotive exhaust catalyst poisoning,” *Appl. Catal. B Environ.*, vol. 50, no. 2, pp. 113–125, 2004.
[131] C. Larese *et al.*, “Deactivation of real three way catalysts by $CePO_4$ formation,” *Appl. Catal. B Environ.*, vol. 40, no. 4, pp. 305–317, 2003.
[132] D. Uy, A. E. O’Neill, L. Xu, W. H. Weber, and R. W. McCabe, “Observation of cerium phosphate in aged automotive catalysts using Raman spectroscopy,” *Appl. Catal. B Environ.*, vol. 41, no. 3, pp. 269–278, 2003.
[133] T. N. Angelidis and S. A. Sklavounos, “A SEM-EDS study of new and used automotive catalysts,” *Appl. Catal. A, Gen.*, vol. 133, no. 1, pp. 121–132, 1995.
[134] C. Xie *et al.*, “Impact of Lubricant Additives on the Physicochemical Properties and Activity of Three-Way Catalysts,” *Catalysts*, vol. 6, no. 4, p. 54, 2016.
[135] S. A. Culley, T. F. McDonnell, D. J. Ball, C. W. Kirby, and S. W. Hawes, “The impact of passenger car motor oil phosphorus levels on automotive emissions control systems,” *SAE Tech. Pap.*, 1996.
[136] W. Chamberlin and F. Zalar, “Balancing crankcase lubricant performance with catalyst life,” *SAE Tech. Pap.*, no. No.841407, 1984.
[137] M. L. Granados *et al.*, “Effect of mileage on the deactivation of vehicle-aged three-way catalysts,” *Catal. Today*, vol. 107–108, pp. 77–85, 2005.
[138] N. Instruments, “The application of PIXE to the mapping of contaminants deposited on a monolithic automotive catalytic converter,” vol. 110, pp. 563–568, 1996.
[139] B. West and C. S. Sluder, “Lubricating oil consumption on the standard road cycle,” *SAE Tech. Pap.*, vol. 2, 2013.
[140] “HORIBA| Fluid Measurement & Control| Mass Flow Controller.” [Online]. Available: https://www.horiba.com/en_en/fluid-measurement-and-control/. [Accessed: 15-Apr-2020].
[141] K. G. Rappé *et al.*, “Aftertreatment Protocols for Catalyst Characterization and Performance Evaluation: Low-Temperature Oxidation, Storage, Three-Way, and NH_3-SCR Catalyst Test Protocols,” *Emiss. Control Sci. Technol.*, 2019.

[142] “Electron Probe Micro Analyzer Introduction to JEOL Products JEOL Ltd.” [Online]. Available: https://www.jeol.co.jp/en/science/epma.html. [Accessed: 15-Apr-2020].
[143] J. Goodge, “Electron probe micro-analyzer (EPMA),” *Univ. Minnesota-Duluth*, p. 2888, 2012.
[144] “X-ray diffraction.” [Online]. Available: https://www.stresstech.com/en-fi/products/x-ray-diffraction-equipment/x-ray-diffraction/. [Accessed: 15-Apr-2020].
[145] K. S. W. Sing, “Reporting physisorption data for gas/solid systems with special reference to the determination of surface area and porosity (Recommendations 1984),” *Pure Appl. Chem.*, vol. 57, no. 4, pp. 603–619, 1985.
[146] M. Thommes *et al.*, “Physisorption of gases, with special reference to the evaluation of surface area and pore size distribution (IUPAC Technical Report),” *Pure Appl. Chem.*, vol. 87, no. 9–10, pp. 1051–1069, 2015.
[147] S. Brunauer, P. H. Emmett, and E. Teller, “Adsorption of Gases in Multimolecular Layers,” *J. Am. Chem. Soc.*, vol. 60, no. 2, pp. 309–319, 1938.
[148] E. P. Barrett, L. G. Joyner, and P. P. Halenda, “The Determination of Pore Volume and Area Distributions in Porous Substances. I. Computations from Nitrogen Isotherms,” *J. Am. Chem. Soc.*, vol. 73, no. 1, pp. 373–380, 1951.
[149] “ICP-MS Systems and Technologies | Thermo Fisher Scientific - NL.” [Online]. Available: https://www.thermofisher.com/us/en/home/industrial/spectroscopy-elemental-isotope-analysis/spectroscopy-elemental-isotope-analysis-learning-center/trace-elemental-analysis-tea-information/icp-oes-information/icp-oes-system-technologies.html. [Accessed: 15-Apr-2020].
[150] E. Adams, M. Skoglundh, P. Gabrielsson, and P.-A. Carlsson, “Passive SCR: The Effect of H_2 to NO Ratio on the Formation of NH_3 Over Alumina Supported Platinum and Palladium Catalysts,” *Top. Catal.*, vol. 59, no. 10, pp. 970–975, 2016.
[151] S. H. Oh and T. Triplett, “Reaction pathways and mechanism for ammonia formation and removal over palladium-based three-way catalysts: Multiple roles of CO,” *Catal. Today*, vol. 231, pp. 22–32, 2014.
[152] K. Ramanathan, C. S. Sharma, and C. H. Kim, “Global Kinetics for Ammonia Formation and Oxidation Reactions in a Commercial Three-Way Catalyst,” *Ind. Eng. Chem. Res.*, vol. 51, no. 3, pp. 1198–1208, 2012.

[153] R. Dümpelmann, N. W. Cant, and D. L. Trimm, “Enahncement of the reaction of nitric oxide and carbon monoxide by hydrogen and water over platinum and rhodium-containing catalysts,” *Stud. Surf. Sci. Catal.*, 1995.
[154] R. Dümpelmann, N. W. Cant, and A. D. Cowan, “The role of gaseous and surface isocyanates in the reaction of mixtures of H_2, NO, and CO over supported platinum catalysts,” in *Studies in Surface Science and Catalysis*, vol. 101, Elsevier, 1996, pp. 1175–1184.
[155] R. Dümpelmann, N. W. Cant, and D. L. Trimm, “The Formation of Isocyanic Acid (HNCO) by Reaction of NO, CO, and H_2 over Pt/SiO_2 and Its Hydrolysis on Alumina,” *J. Catal.*, vol. 162, no. 1, pp. 96–103, 1996.
[156] D. C. Chambers, D. E. Angove, and N. W. Cant, “The formation and hydrolysis of isocyanic acid during the reaction of NO, CO, and H_2 mixtures on supported platinum, palladium, and rhodium,” *J. Catal.*, vol. 204, no. 1, pp. 11–22, 2001.
[157] N. W. Cant, D. C. Chambers, and I. O. Y. Liu, “The formation of isocyanic acid and ammonia during the reduction of NO over supported platinum group metals,” *Catal. today*, vol. 93, pp. 761–768, 2004.
[158] C. Descorme, R. Taha, N. Mouaddib-Moral, and D. Duprez, “Oxygen storage capacity measurements of three-way catalysts under transient conditions,” *Appl. Catal. A, Gen.*, vol. 223, no. 1, pp. 287–299, 2002.
[159] R. J. Gorte, “Ceria in catalysis: From automotive applications to the water–gas shift reaction,” *AIChE J.*, vol. 56, no. 5, pp. 1126–1135, 2010.
[160] Z. Han *et al.*, “Performance of dynamic oxygen storage capacity, water–gas shift and steam reforming reactions over Pd-only three-way catalysts,” *Catal. Today*, vol. 158, no. 3–4, pp. 481–489, 2010.
[161] W. Jianqiang, S. Meiqing, W. Jun, and W. Wang, “Steam effects over $Pd/Ce_{0.67}Zr_{0.0.33}O_2$ three-way catalyst,” *J. Rare Earths*, vol. 29, no. 3, pp. 217–224, 2011.
[162] R. Jain and R. Maric, “Synthesis of nano-Pt onto ceria support as catalyst for water–gas shift reaction by Reactive Spray Deposition Technology,” *Appl. Catal. A Gen.*, vol. 475, pp. 461–468, 2014.
[163] E. V Rebrov, “Advances in water-gas shift technology: Modern catalysts and improved reactor concepts,” in *Advances in Clean Hydrocarbon Fuel Processing*, Elsevier, 2011, pp. 387–412.
[164] T. N. Angelidis *et al.*, “Causes of deactivation and an effort to regenerate a commercial spent three-way catalyst,” *Catal. Automot. Pollut. Control IV*, vol. 116, pp. 155–164, 1998.
[165] D. E. Angove and N. W. Cant, “Position dependent phenomena during deactivation of three-way catalytic converters on vehicles,” *Catal. today*, vol. 63, pp. 371–378, 2000.

[166] K. Voss, B. Yavuz, C. Hirt, and R. Farrauto, “Performance characteristics of a novel diesel oxidation catalyst,” SAE Technical Paper, 1994.
[167] R. J. Farrauto and K. E. Voss, “Monolithic diesel oxidation catalysts,” *Appl. Catal. B Environ.*, vol. 10, no. 1–3, pp. 29–51, 1996.
[168] L. Wang, L. Wang, G. Li, and X. Xu, “The Effect of ZDDP Type on Phosphorus Volatility: Engine Oil Performance on Sequence IIIG and Field Tests,” SAE Technical Paper, 2013.
[169] N. Hussain, “Phosphorus Poisoning and Characterization of Al_2O_3 Based Support Material,” 2014.
[170] M. Kärkkäinen, “Deactivation of oxidation catalysts by sulphur and phosphorus in diesel and gas driven vehicles,” 2017.
[171] “C. Stuart Daw | ORNL.” [Online]. Available: https://www.ornl.gov/our-people/c-stuart-daw. [Accessed: 16-Apr-2020].
[172] R. Hayes and S. Kolaczkowski, “Introduction to Catalytic Combustion,” in *CRC press*, Gordon and Breach Science Publishers, 1998.
[173] Z. Gao, V. K. Chakravarthy, and C. S. Daw, “Comparisons of the simulated emissions and fuel efficiencies of diesel and gasoline hybrid electric vehicles,” in *Proceedings of the Institution of Mechanical Engineers, Part D: Journal of Automobile Engineering*, 2011.
[174] J. Gong and C. Rutland, “Three way catalyst modeling with ammonia and nitrous oxide kinetics for a lean burn spark ignition direct injection (SIDI) gasoline engine,” SAE Technical Paper, 2013.
[175] J. Gong, “Passive ammonia SCR and filtration modeling for fuel-neutral engine aftertreatment systems,” The University of Wisconsin-Madison, 2014.

VITA

Daekun Kim was born in Mokpo, Republic of Korea on 4 February 1987. He graduated from Mokpo National Maritime University (MMU) in Mokpo, South Korea in February 2009. After completing his B.S., he worked as an engineer with Korea Marine Transport Co., Ltd (KMTC) serving on a number of container ships for 4 years and 8 months. In the spring of 2015, he attended the University of Tennessee in Knoxville, TN. He earned his M.S. in Mechanical Engineering in December 2017 and completed his Ph.D. studies in August 2020.